Department of Precision and Microsystems Engineering

Design and Experimental Validation of a Permanent Magnet Long-Stroke Gravity Compensator

R. S. Argiro

Report no : 2021.004
Coaches : Ir. J.W. Spronck & Ir. M. Dansberg (DEMCON)
Professor : Prof. dr. Ir. J.L. Herder
Specialisation : Mechatronic System Design
Type of report : Master Thesis
Date : January 27, 2021

PERMANENT MAGNET LONG-STROKE GRAVITY COMPENSATOR

DESIGN AND EXPERIMENTAL VALIDATION OF A PERMANENT MAGNET LONG-STROKE MAGNETIC GRAVITY COMPENSATOR FOR A NANOMETER PRECISION POSITIONING MACHINE

by

R.S. Argiro

to obtain the degree of Master of Science

at the Delft University of Technology,

to be defended publicly on Wednesday January 27th, 2021 at 13:30 PM.

Supervisors:	Ir. J.W. Spronck (TUDelft)	Ir. M. Dansberg (DEMCON)
Thesis committee:	Ir. J.W. Spronck,	TU Delft
	Dr. S.H. Hossein Nia Kani,	TU Delft
	Dr. A. Hunt	TU Delft

This thesis is confidential and cannot be made public until January 27, 2023.

TU Delft Delft University of Technology

PREFACE

I would like to thank Jo and Michel for their advice and guidance throughout this project. They have provided my with valuable feedback to help this project to become a great success.

Furthermore, I would like to thank all the students and staff in the Monday morning meetings: Bas, Marcin, Madan, Andres, Timothy, Tim, Romano, Marcos, Hassan, and all the other names I am forgetting. I have always enjoyed the fruitful discussions and conversations.

Also, I would like to thank my housemates, for their help and understanding in the times I was not able to join the huisavonden, game nights, movie watching, etc.

Finally and foremost I would like to thank my girlfriend who was always there for me through the ups and downs. She has been the constant support helping me to stay motivated, hear me out when I was doubtful, and my go-to person when I didn't see the light at the end of tunnel.

R.S. Argiro
Delft, January 15, 2021

SUMMARY

In the High-Tech industry, positioning accuracy and precision are crucial factors, for example in the chip manufacturing process where positioning machines are used. To achieve this performance, these machines use a layout that is comprised of a series of cascaded stages, stacked on top of one another (see figure 1a). The long-stroke stages are required to achieve the needed movement ranges in the $x-$ and $y-$ directions, while the fine stage is responsible for the final, high accuracy, positioning of the substrate. Even though this concept has proven its worth, a better alternative could be envisioned where the same performance could be obtained but at a significantly lower machine cost. This can be achieved by using only a single long-stroke stage, combined with a fine stage that also has a long-stroke capability in the remaining horizontal direction (see figure 1b). This would result in a substantial reduction of the machine complexity and therefore the accompanying costs.

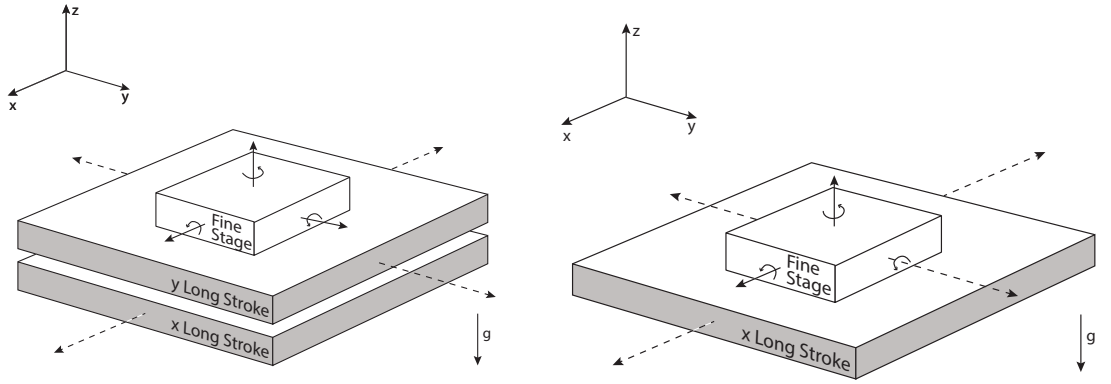

(a) The current, more complex, design composed of three cascaded stages.

(b) The proposed, simpler, design consiting of only two stages (the long arrows on the fine stage indicate the long-stroke movement direction).

Figure 1: The envisioned design improvement in the layout of high precision positioning machines.

One of the components inhibiting the proposed innovation is the gravity compensator, which is a crucial part for the functioning of the entire machine. The gravity compensator is a passive element, compensating for the static force of gravity on the fine stage. This reduces the force required from the $z-$direction actuators, which in turn reduces their heat production. Without the gravity compensator, the heat generation of these actuators would be too large for the machine to obtain the required performance. Besides the ability to support the specified weight of the fine stage, gravity compensators are also required to have a low stiffness to limit disturbing forces on the fine stage. These disturbing forces are the result of the parasitic stiffness of the gravity compensator combined with the relative motion between the fine stage and the long-stroke stage underneath, caused by the vibrations present in the machine.

However, to enable the proposed innovation in the layout of high precision positioning machines, a long-stroke gravity compensator is required. Therefore, the goal of this thesis is: "***To design and experimentally validate a permanent magnet based long-stroke gravity compensator for a nanometer precision positioning machine***". To achieve this goal, four specific research objectives have been identified:

1. Perform a state of the art study to find suitable magnet configurations that could provide the needed combination of a high load capacity and a low stiffness.

2. Find modeling techniques that can be used to calculate interaction forces between permanent magnets to determine performance parameters of different magnetic designs.

3. Combining the modeling techniques with the found magnet configurations and design a long stroke magnetic gravity compensator that is suitable for the intended application. For this purpose, a set of design requirements has been defined, of which the most important aspects are listed in table 1. Both the model and the design will be validated using an experimental setup.
4. Finally, the achievable performance of a long-stroke gravity compensator will be determined to provide the information to assess the suitability of the long-stroke gravity compensator for high precision positioning machines.

The results of these four objectives are discussed below.

In the literature study into the state of the art of magnetic gravity compensation, many design variations were observed. These designs were categorized and reduced to four fundamental configurations that all show the desired combination of a high load capacity with a low stiffness. From the information presented in literature, a trade-off was made between the four configurations where the two most suitable were selected for further research.

Furthermore, four modeling techniques were found that can be used to calculate interaction forces between permanent magnets, namely; the dipole model, finite element methods, the coil model, and the surface charge model. From a comparison between these four, it was concluded that the dipole model cannot be used in the design of a magnetic gravity compensator, as its accuracy is severely limited. On the contrary, a 2D implementation of the combination between finite element methods and the coil model proved to be a very strong and capable design tool. The main advantage of this approach is that it provides a lot of understanding of the working principles of the specific magnet configurations, therefore allowing for a quick design process. However, from a comparison between 2D and 3D models, it was concluded that it is best practice to check the results of a 2D analysis with a 3D model. It is therefore advised to always use a 3D model for determining the final design dimensions.

The two selected magnet configurations from the state of the art study, and the 2D modeling technique described above, were combined to develop three different designs. During this process, the magnet dimensions were optimized to meet the stiffness and load capacity requirements from table 1. For this analysis ideal magnets were used (i.e. neglecting manufacturing tolerances) resulting in stiffnesses as low as 24 $\left[\frac{N}{m}\right]$. Subsequently, the sensitivity of each design to magnet tolerances was determined and compared. All designs were subjected to equal variations in magnet dimensions, magnetization strength, and magnetization angle. This resulted in significant increases in stiffness (up to a factor of 20 w.r.t. the ideal case), leading to the important conclusion that these tolerances cannot be neglected in the design of magnetic gravity compensators. From the three magnetic designs, the configuration with the lowest stiffness increase due to the magnetic tolerances was chosen, resulting into the final design as showed in figure 2.

This final design was built into an experimental setup using standard magnets. The goal of the setup was to validate both the used model and the design of the gravity compensator. The chosen approach to achieve these goals, was to measure the magnetic field in the air gap between the stator magnets, as the magnetic field created by the stator directly determines the forces (and hence also the stiffnesses) onto the mover magnet of the gravity compensator. From the measurements it was observed that the variations of the magnetic field were within the expected 3σ uncertainty interval, thereby validating the model. From the measurement data the maximum absolute stiffness was estimated at 720 $\left[\frac{N}{m}\right]$ (see table 1), which is within specification. However the maximal peak-to-peak change in the stiffness over the entire stroke was approximately 1320 $\left[\frac{N}{m}\right]$, therefore indicating that the performance specifications cannot be met using standard magnets.

To determine the achievable performance, the 3D surface charge model was implemented into a Monte Carlo simulation. In this approach, magnetic tolerances were randomly generated for 2000 gravity compensators, and the resulting performance parameters were calculated. The results were statistically evaluated. The mean obtained performance for Grade A, and highly specified magnets are listed in table 1.

From the resulting performance presented in table 1 it is concluded that a long-stroke gravity compensator can be applied in nanometer positioning equipment if high-grade magnets are used. Even though when using Grade A magnets the peak-to-peak change of the stiffness is slightly outside of the requirement, the

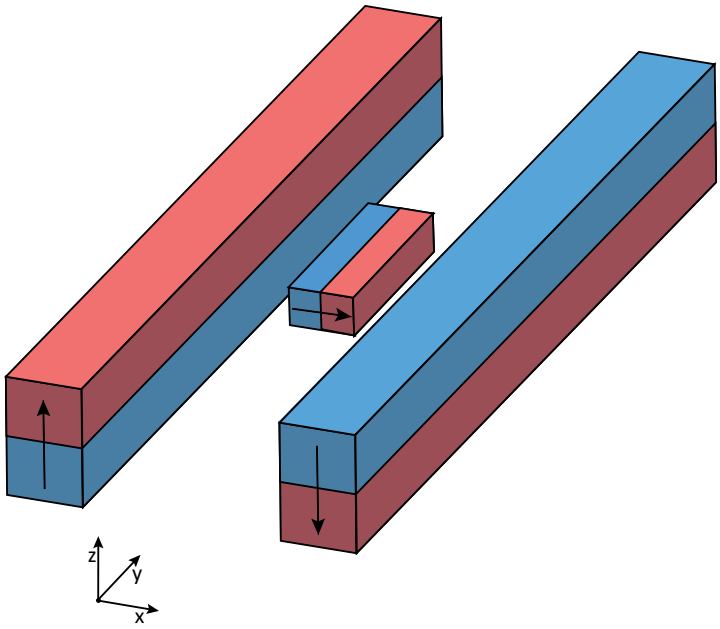

Figure 2: Schematic of the design of the magnetic gravity compensator of the mover magnet in between the two stator magnets.

Table 1: Overview of obtained performance with different magnet classes.

Design Requirements	**Values**	**Experimental setup**	**Grade A magnets**	**Highly specified magnets**
Strokes: x, y, z	$1,200,1\,[mm]$	$1,200,1\,[mm]$	$1,200,1\,[mm]$	$1,200,1\,[mm]$
Nominal load Capacity:	$196.2\,[N]$	$197.9\,[N]$	$196.0\,[kg]$	$196.0\,[kg]$
Parasitic Stiffness:	$\leq 1000\,[\frac{N}{m}]$	$720\,[\frac{N}{m}]$	$150\,[\frac{N}{m}]$	$90\,[\frac{N}{m}]$
Change of Stiffness:	$\leq 200\,[\frac{N}{m}]$	$1320\,[\frac{N}{m}]$	$250\,[\frac{N}{m}]$	$150\,[\frac{N}{m}]$
Force Error:	$\leq 1\,[N]$	$12\,[N]$	$1\ [N]$	$0.5\ [N]$
Magnet costs:		$\approx$ € 500	$\approx$ € 800	$\approx$ € 1000

long-stroke magnetic gravity compensator can still be implemented successfully by utilizing simple control algorithms in the feedforward controller of the machine, to compensate for the changes in the stiffness. On the other hand, if the budget allows, more expensive highly specified magnets can be used to ensure that all requirements are met.

In conclusion, this research has proven that a long-stroke magnetic gravity compensator can successfully be designed to meet the required design specifications. Thereby, the first step has been made towards the next generation of nanometer precision positioning machines.

CONTENTS

1

INTRODUCTION

1.1. MOTIVATION

The societal demand for smaller and more powerful electronic components and devices fuels the innovation in the High-Tech and Semiconductor industry where the boundaries of achievable position accuracy and precision are continuously being pushed further and further. To reach this incredible performance, positioning machines are traditionally designed with a set of three cascaded stages (see figure 1.1). The bottom two stages are referred to as long-stroke stages. They have a single degree-of-freedom and are needed to cover the required working area in the horizontal plane (the $x-$ and $y-$ direction). The fine stage is placed on top, which is positioned in six degrees-of-freedom. High precision Lorentz Force Actuators are used to position the fine stage and the substrate with nanometer-level accuracy and precision.

Even though conceptually this is a simple design, a lot of moving parts are required, therefore the cost-effectiveness of the design can be questioned. An alternative design could be envisioned where the performance is maintained, but the complexity is reduced significantly. This design would consist of only two stages. The first being a single DOF long-stroke stage similar to the one in the original design, moving in the $x-$direction. On top of this, a 6 DOF fine stage is placed, which is also capable of making a long-stroke in the $y-$direction. This design is substantially simpler, making it a huge improvement in the overall cost-effectiveness of nanometer precision positioning machines.

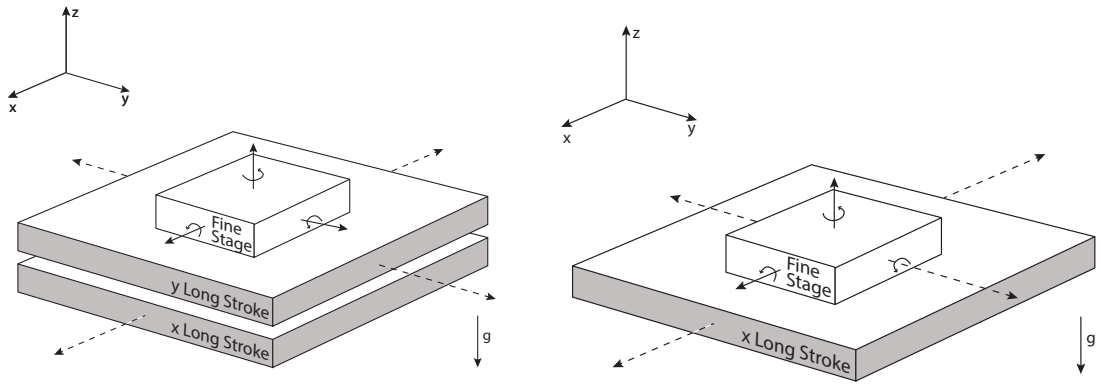

(a) The current, more complex, design composed of three cascaded stages.

(b) The proposed, simpler, design consiting of only two stages (the long arrows on the fine stage indicate the long-stroke movement direction).

Figure 1.1: The envisioned design improvement in the layout of high precision positioning machines.

Unfortunately, this proposed innovation in the layout of these high-precision positioning machines is currently inhibited by a crucial component of these machines namely; the gravity compensator. A gravity compensator is a passive element used to support the fine stage in the gravitational direction. This reduces the

load on the actuators working in the $z-$direction, therefore improving the thermal stability of the machine. To put it differently, the function of the gravity compensator is to counteract the static force on the fine stage due to gravity. Besides their load capacity, gravity compensators also require a low stiffness to limit the effect of the present vibrations in the machine. These vibrations cause relative motion, between the fine stage and the long-stroke stages below, in all directions. Due to the parasitic stiffness of the gravity compensator, this generates disturbing force onto the fine stage. It is, therefore, crucial to limit the stiffness, as insufficient attenuation of these disturbing forces will compromise the positioning accuracy and precision of the entire machine.

Gravity compensators can be constructed in three ways: firstly, they can be made using low stiffness mechanical springs. Secondly, pneumatic systems can be designed with multiple chambers and complex valve systems, resulting in a low effective stiffness. Finally, permanent magnets can be used to create the needed combination of load capacity and low stiffness. The latter is the preferred option as there is no physical connection between the long-stroke stage and the fine stage. This has the advantage that there are no internal dynamics that could cause disturbance forces at higher frequencies due to internal resonance modes of a connecting structure. Also, pneumatic devices are not preferred in high vacuum applications, whereas magnets can easily be made vacuum compatible.

However, to enable the proposed innovation in the high precision positioning concept, a long-stroke gravity compensator is required. Unfortunately, these are not commercially available, nor has a study been published investigating their performance. Therefore, in this thesis, the feasibility of a permanent magnet-based long-stroke gravity compensator for a high precision positioning machine will be investigated.

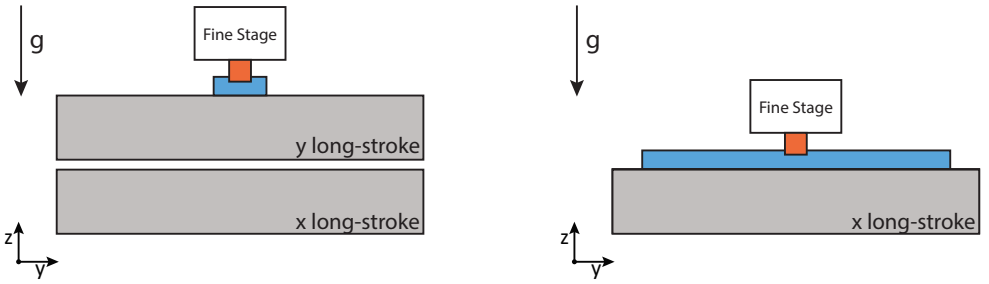

(a) The current, more complex, design in side view with a traditional gravity compensator.

(b) The proposed, simpler, design in side view with the long-stroke gravity compensator.

Figure 1.2: The envisioned design improvement made possible by the long-stroke magnetic gravity compensator (gravity compensator is indicated in color in both figures).

1.2. RESEARCH GOALS AND OBJECTIVES

To take the first step towards the innovative positioning machine layout from figures 1.1b and 1.2b, the suitability of permanent magnet long-stroke gravity compensators must be studied. Therefore the goal of this research is: "***To design and experimentally validate a permanent magnet based long-stroke gravity compensator for a nanometer precision positioning machine***". To aid this process, the following research goals have been defined:

1. A suitable modeling technique is required to determine interaction forces between permanent magnets. This will be a crucial tool in the design process as the resulting load capacity and stiffness of the magnetic design need to be evaluated.

2. Magnetic configurations need to be found that provide the combination of a load capacity with a low stiffness. For this, a literature study into the state of the art of magnetic gravity compensation will be conducted. The results from this research will be used as a starting point for the magnetic design of the gravity compensator.

3. Using the model and the found magnetic configurations, a design will be made for a long-stroke magnetic gravity compensator. This design and the model will be validated using measurements performed on an experimental setup.

4. Finally, using the validated model, the achievable performance of a long stroke magnetic gravity compensator will be determined. This will provide the answer to the question if a long stroke gravity compensator can successfully be implemented into a nanometer precision positioning machine.

1.3. DESIGN SPECIFICATIONS

A set of design requirements has been constructed to provide measurable criteria for the design of the long-stroke gravity compensator in a high precision positioning application. These design requirements can be found in table 1.1, and are discussed briefly in more detail in the following subsections.

Table 1.1: Overview of design specifications for a long-stroke permanent magnet gravity compensator.

Spec. nr.	Design Specification	Symbol	Value	Unit
1	**Strokes and Velocity**			
1.1	Translational strokes	$x,\ y,\ z$	$1,200,1$	$[mm]$
1.2	Rotational strokes	$R_x,\ R_y,\ R_z$	$1,1,1$	$[mrad]$
1.2	Maximum velocity in long stroke direction	$v_{y,max}$	250	$\left[\frac{mm}{s}\right]$
2	**Load Capacity and Force Error**			
2.1	Fine stage mass	m_{fs}	20	$[kg]$
2.2	Maximum force error in nominal position	$F_{e,max}$	<1	$[N]$
3	**Parasitic Stiffness and Damping**			
3.1	Maximum parasitic stiffness	$\lvert k_x\rvert,\ \lvert k_y\rvert,\ \lvert k_z\rvert$	<1000	$\left[\frac{N}{m}\right]$
3.2	Maximum peak to peak change of stiffness	$\Delta k_x,\ \Delta k_y,\ \Delta k_z$	<200	$\left[\frac{N}{m}\right]$
3.3	Maximum parasitic damping constant	c_y	<1	$\left[\frac{Ns}{m}\right]$
4	**Number and Size Constraints**			
4.1	Maximum number of gravity compensators	n_{max}	3	$[-]$
4.2	Maximum height of the gravity compensator(s)	h_{max}	50	$[mm]$
4.3	Maximum width of the gravity compensator(s)	w_{max}	50	$[mm]$

1.3.1. STROKES AND VELOCITY

The strokes of the gravity compensator are defined as the possible motion range of the mover of the gravity compensator, with respect to the stator. The stator of the gravity compensator is attached to the long-stroke stage, and the mover is the part of the gravity compensator that is attached to the fine stage. As the fine stage is positioned in 6 degrees-of-freedom, it moves relative to the long-stroke stage below it. From figure 1.3 it can be seen that the $x-$ and $z-$ directions correspond to the short-stroke directions and that the long-stroke direction is chosen as the $y-$direction. The negative $z-$direction corresponds to the gravitational direction. This results in the required strokes of $1,200,1$ $[mm]$ for the $x-$, $y-$, $z-$directions respectively. The required rotational strokes are 1 $[mrad]$ for all axis. The maximal velocity is only defined in the long-stroke direction, as the velocities in the $x-$ and $z-$directions are negligible. This maximum velocity will be relevant for determining the maximum damping constant.

1.3.2. LOAD CAPACITY AND FORCE ERROR

The mass of the fine stage is specified at 20 $[kg]$, therefore resulting in a required load capacity of

$$20\ [kg] \cdot 9.81 \left[\frac{m}{s^2}\right] = 196.2\ [N].$$

The force error is defined as the error between the force provided by the gravity compensator and the required load capacity of 196.2 $[N]$. This error is a measure for the heat that will be generated by the actuators in the machine during operation, as the deviation from the required capacity needs to be compensated for by the actuators. The force error needs to be determined in the nominal "position", which is defined as the following set of coordinates: $x = 0\ [mm]$, $y \in [-100,\ 100]\ [mm]$, $z = 0\ [mm]$. It is, therefore, in contrary to normal

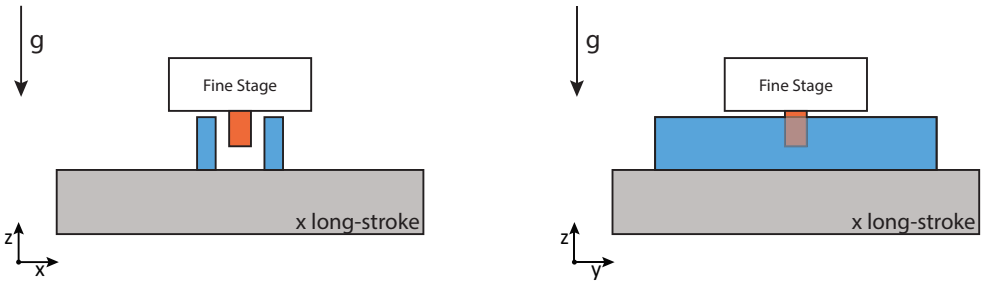

(a) Side view showing the short stroke directions.

(b) Side view showing the long-stroke direction.

Figure 1.3: Schematic of the strokes of the long-stroke gravity compensator (stator of the gravity compensator indicated in blue, the mover is indicated in red).

gravity compensators, not a single point, but an entire line over which this force error needs to be evaluated.

1.3.3. PARASITIC STIFFNESS AND DAMPING

As explained, a low stiffness is very important for the application of a gravity compensator into a high precision positioning application as the effect of disturbance forces due to vibrations needs to be limited. Therefore, the absolute value of the parasitic (unwanted) stiffness in all translational directions cannot exceed 1000 $\left[\frac{N}{m}\right]$.

Additionally, the maximum peak to peak change of the stiffness should also be limited. The peak to peak change of the stiffness refers to the difference between the minimum and maximum value of the stiffness, which is set at a maximum of 200 $\left[\frac{N}{m}\right]$ in all directions.

The maximum absolute stiffness and the maximum peak to peak stiffness requirement have been schematically visualized in figures 1.4a and 1.4b for clarity purposes. Important to mention is that these requirements should be met over the entire movement domain of the gravity compensator. In other words, for all possible combinations of $x-$, $y-$, and $z-$coordinates of the mover gravity compensator with respect to the stator, the stiffness cannot exceed the specified 1000 $\left[\frac{N}{m}\right]$. Similarly, the maximum peak to peak change of the stiffness should remain below 200 $\left[\frac{N}{m}\right]$. This can be mathematically represented as

$$
\begin{aligned}
|k_x|,\ |k_y|,\ |k_z| \leq 1000\ \left[\frac{N}{m}\right] \quad & \text{for} \quad (x,y,z) \in ([-1,1],[-100,100],[-1,1])\ [mm] \\
& \text{and} \quad (\theta_x,\theta_y,\theta_z) \in ([-1,1],[-1,1],[-1,1])\ [mrad] \\
\Delta k_x, \Delta k_y, \Delta k_z \leq 200\ \left[\frac{N}{m}\right] \quad & \text{for} \quad (x,y,z) \in ([-1,1],[-100,100],[-1,1])\ [mm] \\
& \text{and} \quad (\theta_x,\theta_y,\theta_z) \in ([-1,1],[-1,1],[-1,1])\ [mrad].
\end{aligned}
$$

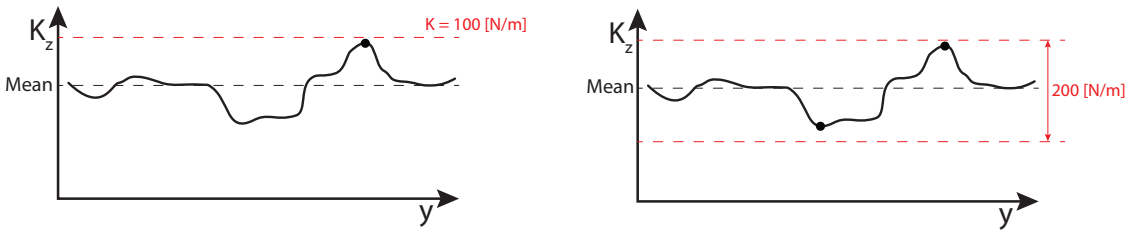

(a) Visualization of the maximum absolute stiffness requirement.

(b) Visualization of the maximum peak to peak change of the stiffness varaition.

Figure 1.4: Graphical visualizations of the maximum stiffness and maximum peak to peak change of the stiffness requirements.

1.3.4. NUMBER AND SIZE CONSTRAINTS

The maximum number of gravity compensators allowed in the design is 3, meaning that the required load capacity can be divided over 1, 2, or 3 gravity compensators. The needed number of gravity compensators will be determined during the design process where the load capacity of the different designs needs to be assessed. This cannot be decided in advance, as there are also two size restrictions for each individual gravity compensator. The maximal cross-sectional dimensions are 50 $[mm]$ in the $x-$direction (referred to as the width), and also 50 $[mm]$ in the $z-$direction (referred to as the height). In other words, irrespective of the number of gravity compensators used (1,2, or 3) the maximum width and height of each gravity compensator cannot exceed 50 by 50 $[mm]$. Note that there is no size restriction given in the long-stroke direction, as the required length needs to be determined during the design process. This is due to the fact that in this direction the stiffness and force error requirements are leading in the needed dimension.

1.4. THESIS OUTLINE

In chapter 2 the fundamentals of magnetic materials are discussed. This also includes modeling options for the interaction forces between permanent magnets. Chapter 3 discusses the results of the literature study into the state of the art of magnetic gravity compensation. Four suitable magnetic designs were found for a gravity compensator from which two were selected for further investigation. In chapter 4 the selected designs are evaluated in detail after which, the one with the best performance was chosen as a final design. Subsequently, in chapter 5 and 6 the design of the experimental setup and the taken measurements are presented. In chapter 7 the achievable performance of a long-stroke magnetic gravity compensator is discussed. The final conclusions and recommendations for further research are presented in 8.

2

Fundamentals of Magnetic Materials and Modeling of Interaction Forces

To successfully design a long-stroke magnetic gravity compensator, it is crucial that performance parameters such as load capacity and stiffness can be calculated. As explained in chapter 1, these parameters are key for the proposed application and are a direct result of the forces between the permanent magnets incorporated in the design. It is therefore essential that these forces can be calculated to assess the feasibility of the long-stroke magnetic gravity compensator for nanometer precision positioning machines. Ideally, the modeling technique would also provide insight into how the magnetic design could be changed to improve its performance, as this will be very valuable information during the design process.

The first step in this process is to understand the basics of magnetic materials. This mainly includes how to characterize them and identify the relevant parameters needed as input for the modeling. Secondly, different modeling options need to be found and understood, to understand their pros and cons. Finally, these techniques will be compared to assess their limitations. Together, these points will provide the needed information to select an appropriate modeling technique for the different calculations during this study. The following subsection will cover these aspects in more detail.

2.1. Magnetic Materials

The response of materials to an external magnetic field can be categorized in three ways: paramagnetic, diamagnetic, and ferromagnetic. Out of these three, ferromagnetic materials are the only materials that retain their magnetic properties once an applied magnetic field is removed. Therefore, making it the only one suitable type of materials for the production of permanent magnets, and thus the only category of interest in this study.

The mechanism behind the retention of the magnetization in ferromagnetic materials lies in the alignment of the magnetic domains. A material is said to be magnetized when the internal magnetic domains are aligned with each other. Under normal conditions, the orientations of the magnetic domains in ferromagnetic materials are distributed randomly, therefore resulting in a zero net magnetization. This can be seen in figure 2.1a. However, when an external field is applied (figure 2.1b), the magnetization of the domains aligns with the applied field. When the external field is removed, the domains remain aligned, therefore resulting in what we know as a permanent magnet (figure 2.1c).

2.1.1. Permanent Magnet Parameters and BH Curves

The relation between the externally applied field and the alignment of the material is often a complex, nonlinear function, that varies from material to material. It used in the classification of permanent magnets and provides insight into the behavior of the materials and the relevant parameters for their modeling. This relation between the externally applied field (represented by H in $[\frac{A}{m}]$) and the resulting alignment of the magnetic domains (quantified by the parameter B in $[T]$) is referred to as the $B-H$ or hysteresis curve of the magnetic material. A typical $B-H$ curve of a ferromagnetic material can be seen in figure 2.2a. On the

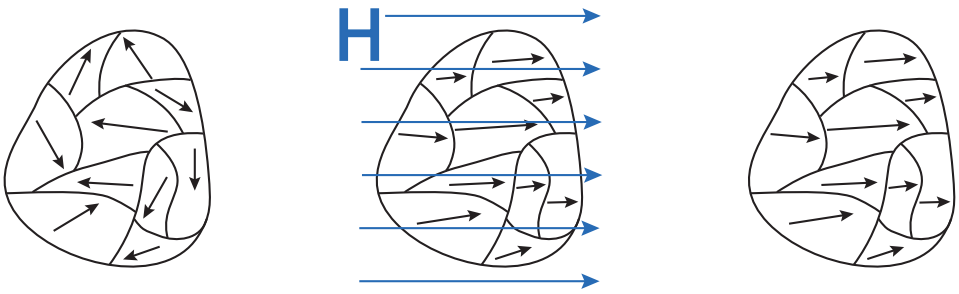

(a) Not magnetized material.

(b) Magnetization of the material due to the applied field.

(c) Remaining, permanent magnetization after the applied field is removed.

Figure 2.1: Alignment of the magnetization of the magnetic domains in ferromagnetic material.

right, in figure 2.2b, the state of the magnetic domains at the indicated points on the curve are schematically depicted.

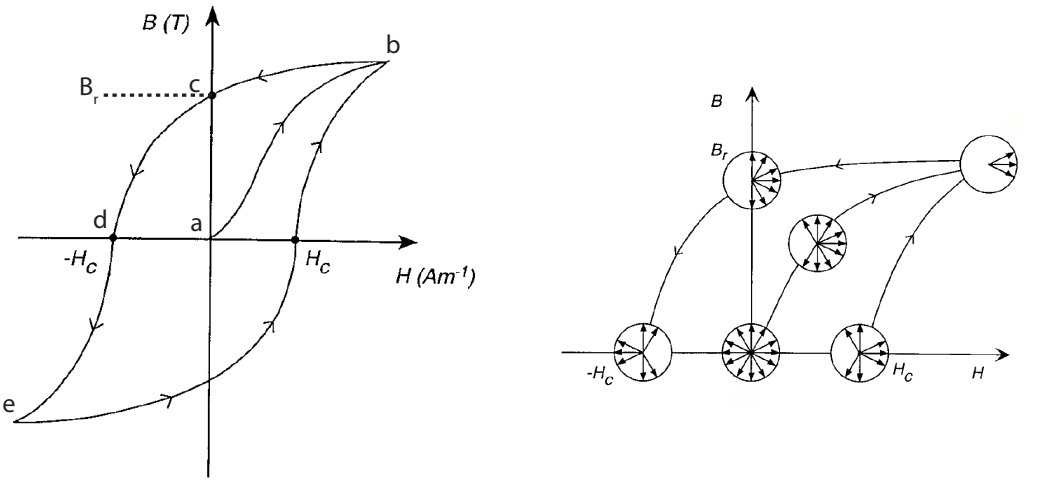

(a) Typical $B-H$ curve of ferromagnetic material.

(b) States of the magnetic domains at various points in the $B-H$ curve.

Figure 2.2: Magnetization $B-H$ curve and states of the magnetic domains (both are taken from [1]).

As previously explained, the material starts out as not magnetized (point a), where the magnetic domains are randomly oriented throughout the material. When a positive external field is applied, the magnetization of all the domains aligns with the applied field, where the degree of alignment depends on the strength of the external field. If the field is increased until all the domains are completely aligned the material is said to be saturated, indicated by point b. The curve from point a to point b thus represents the action of magnetizing the material and is referred to as the virgin curve. When the external field is again decreased, the alignment of the domains also slightly decreases, eventually ending up at point c, where the external field is zero. Here a permanent magnet is obtained like the one we know from refrigerator magnets for example. Subsequently, if a negative field is applied in the opposite direction, the alignment decreases further, until the net produced field by the magnet and the external field is zero (point d). If then the field is increased further, all the magnetic domains align in the opposite direction, resulting again in saturation (point e).

From the $B-H$ curve two important characteristics can be derived. The first one is the remanence or remnant flux density of the magnetic material, and is indicated by the symbol B_r and is measured in the unit of Tesla ($[T]$). The remanence of a magnetic material is a measure of the remaining alignment of the magnetic domains and is, therefore, a measure for the strength of the permanent magnet. The other parameter is referred

to as the coercivity or coercive force of the magnetic material and is indicated by H_c, measured in amperes per meter ($[\frac{A}{m}]$). This provides a measure of how easily the material is magnetized and demagnetized. Both these parameters are essential in the classification and modeling of permanent magnets as will be explained later in more detail.

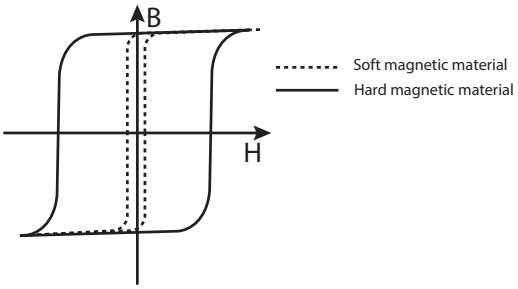

Figure 2.3: $B-H$ curve of hard and soft magnetic materials.

Within the category of ferromagnetic materials, two types of materials can be distinguished: soft magnetic materials and hard magnetic materials. The difference lies mainly in the difference in coercivity. Soft magnetic materials have a very low coercive force and are thus easily magnetized and demagnetized. This makes them suitable for applications such as AC transformers, where the applied field switches direction constantly. As the coecivity is low, the magnetization follows the external field easily. On the other side, hard magnetic materials exhibit a high coercive force, meaning they are hard to magnetize and demagnetize. This makes them suitable for permanent magnets. The differences between these two types of materials are clearly visible when comparing their $B-H$ curves (see figure 2.3).

2.1.2. RARE-EARTH MAGNETS

There is one type of hard magnetic material that is particularly interesting for a magnetic gravity compensator which is the rare-earth magnets. This is due to a couple of properties. First of all, they have very high energy densities (indicated by BH_{max} value in data sheets) and high remanence. This is advantageous as it increases the force density of the magnetic design. Secondly, they exhibit very high coercivity, meaning that they are very hard to demagnetize. In a practical application, this means that they can withstand strong opposing magnetic fields (explained in more detail in subsection 2.1.3), which allows for aspects such as more design freedom and also higher force densities as gap sizes can be reduced without demagnetization. Finally, rare-earth magnets have a linear relationship between the applied field H and the resulting magnetization B. This makes the modeling of rare-earth magnets much easier compared to the non-linear alternatives.

As stated in the previous section, the $B-H$ curve shows the relation between the applied field and the resulting magnetization of the material. This is true, however, it is a somewhat simplified statement. To correctly understand some important aspects of permanent magnetic materials, a slightly more detailed understanding is required. In fact, the magnetic field B is a combination of the applied field and the resulting magnetization of the material. The actual magnetization of the material is quantified by the symbol M with the unit $[\frac{A}{m}]$. As already explained, the magnetization of a material is a function of the applied field, so $M = M(H)$. The parameter χ_m is introduced as the relation between the applied field and the resulting magnetization,

$$\chi_m(H) = \frac{M(H)}{H} = \chi_m, \tag{2.1}$$

which is in fact a constant for rare-earth magnets. The relation between B and H for rare-earth magnets can now be described as

$$B = \mu_0 H + \mu_0 M(H) = \mu_0 H + \mu_0 \chi_m H = \mu_0 (1 + \chi_m) H = \mu_0 \mu_r H, \tag{2.2}$$

clearly showing the linear relation between B and H. The parameter μ_0 in equation 2.2 is the vacuum permeability which is a universal constant with the value of $4\pi \cdot 10^{-7}$ $\left[\frac{N}{A^2}\right]$, and μ_r is called the relative permeability and is a material property. From a typical $B-H$ curve of a rare-earth magnet (see figure 2.4a it can clearly be seen that indeed the relation is linear, of which the slope is defined by the product of mu_0 and mu_r.

One should note that equation 2.2 is only valid for materials that don't retain their magnetization, as it crosses the H axis at $H = 0$. However, from figure 2.4a it can be concluded that the line should cross at the value of

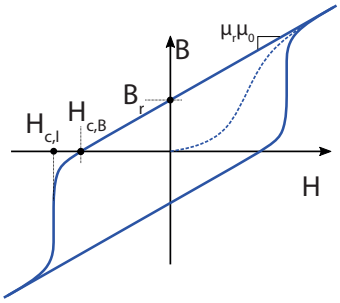

(a) Typical $B-H$ curve of rare-earth magnets, clearly showing the linear $B-H$ relationship.

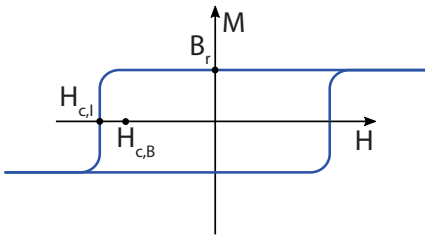

(b) $M-H$ curve of rare-earth magnets, clearly showing the constant magnetization over a large range.

Figure 2.4: Typical $B-H$ and $M-H$ (magnetization vs applied field) curves of rare-earth magnets.

$H_{c,B}$. This can easily accounted for by modifying equation 2.2 into

$$B = \mu_0 \mu_r (H + H_{c,B}). \tag{2.3}$$

If the applied field is set to zero, this reduces to $B = \mu_0 \mu_r H_{c,B} = B_r$, resulting in the equivalent relation

$$B = \mu_0 \mu_r H + B_r. \tag{2.4}$$

It is very important to realize that these equations only apply to linear magnetic materials (like rare-earth magnets) and are only valid in the linear regions of the $B-H$ curves. As soon as the magnetization starts to change due to the applied field these equations are no longer valid. This is clearly visible in figure 2.4b where the actual magnetization M is plotted against the applied field H. From this graph, two very important points need to be noted. The first one is that, in the linear region of the curve, the magnetization is very constant. It actually has a very small slope which is equal to the magnetic susceptibility χ_m as defined by equation 2.1). Rare-earth magnets have a relative permeability that is generally around 1.05. Using equation 2.2 the susceptibility then results in

$$\chi_m = \mu_r - 1 = 1.05 - 1 = 0.05\ [-]. \tag{2.5}$$

It might not seem like a significant result, but this low magnetic susceptibility is actually very useful for the modeling of rare-earth magnets. It means that, in the linear region of the magnetic, the magnetization of the material is nearly constant, irrespective of the applied field. This directly implies that, as long as demagnetization is avoided, changes in magnetization can be neglected when modeling rare-earth magnets. This makes the modeling of rare-earth magnets substantially easier as compared to other, non-linear, hard magnetic materials.

The second important point that should be taken from figures 2.4a and 2.4b, is that there is actually a difference between $H_{c,B}$ and $H_{c,i}$. In section 2.1.1 it was explained that the coercivity H_c of a magnetic material describes how easily a material is magnetized and demagnetized and that it is defined as the value of H for which B is zero. However, in practice, the value for which the net field is zero, and when the magnetization of the material starts to change are generally not the same. Therefore, two separate coercivities are defined. $H_{c,B}$ is referred to as the normal coercive force (or coercivity) and is defined as the intersection point of the $B-H$ curve with the $H-$axis. $H_{c,i}$ is called the intrinsic coercivity and is defined as the point where the $M-H$ curve crosses the $H-$axis. It, therefore, represents the actual value for which permanent demagnetization occurs. In other words, if a permanent magnet is exposed to an opposing field close to H,c,i it is permanently damaged, therefore, this should be avoided. This is discussed in more detail in the next subsection. Table 2.1 gives an overview of typical values for all the discussed parameters of various permanent magnetic materials. From this comparison, it can clearly be seen that rare-earth magnets ($NeFeB$ and $SmCo$) indeed have substantially higher energy densities (BH_{max} values) and coercivities.

2.1.3. DEMAGNETIZATION

As explained in the previous section, $H_{c,i}$ is the value at which a permanent magnet is being demagnetized. In other words, the magnet gets (partially) destroyed. It is clear that this must be avoided in applications such

Table 2.1: Overview of most common ferromagnetic materials (values are taken from [1] section 1.14 to 1.18 and [2] section 9.2.3.2).

Material	$H_{c,i}$ $[kA/m]$	$H_{c,B}$ $[kA/m]$	B_r $[T]$	$(BH)_{max}$ $[kJ/m^3]$	μ_r $[-]$
Alnico	45 – 148	43 – 131	0.7 – 1.5	11.9 – 43.8	2.0 – 6.4
Ferrite	200 – 320	140 – 260	0.23 – 0.41	8 – 32	1.1
SmCo	558 – 1440	480 – 700	0.89 – 1.0	128 – 192	1.05
NeFeB	1200 – 1280	424 – 840	0.61 – 1.18	64 – 256	1.05 – 1.15

as gravity compensators as this would result in large errors in load capacity and increased stiffness values, or in extreme cases a broken gravity compensator and machine.

Magnets can safely operate in the first quadrant of the $B-H$ curve, where the direction of the external field and the magnetization are the same. Magnets can also operate in the second quadrant, where the external field and the magnetization are in opposite directions. However, this is only possible above the region where the $B-H$ curve starts to bend, referred to as the knee of the curve.

Avoiding demagnetization is a crucial step during the design process, therefore a criterion is needed to check whether demagnetization occurs.

However, when checking for demagnetization, not only the external field of a magnet should be taken into consideration. Also, the field of the magnet itself should be taking into account. It might sound counter-intuitive, but a magnet actually "tries" to demagnetize itself. The easiest way to understand this concept is by imagining that a permanent magnet is split into two halves (see figure 2.5a). From this figure, it can clearly be seen that the magnetic field produced by the top half of the magnet is in the opposite direction of the magnetization of the bottom half of the magnet. To the bottom magnet it, therefore "feels" like the top half of the magnet is trying to demagnetize it. The total field that a magnet produces that is trying to demagnetize itself is called the demagnetizing field of the magnet (see figure 2.5b) and is denoted by the symbol H_d.

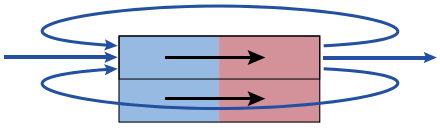

(a) The magnetic field of the top half opposes the direction of magnetization of the bottom half.

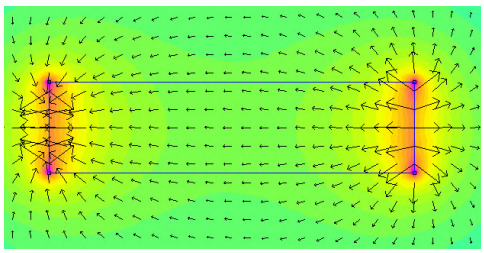

(b) Self demagnetizing field H_d produced by a permanent magnet

Figure 2.5: Self demagnetization of permanent magnets

To avoid demagnetization, the sum of both the demagnetizing field and the externally applied field should remain below the intrinsic coercivity ($H_{c,i}$) of the permanent magnet. Usually, also a safety factor of 0.8 is applied, therefore the criterion to avoid demagnetization can now be written as

$$0.8 \cdot H_{c,i} \geq H_{total} = H_d + H_{ext.}. \tag{2.6}$$

Important to note is that, as the H represents a vector field, the direction of H_{total} with respect to the direction of magnetization should also be considered.

A few examples of the application of this criterion can be observed in figures 2.6a, 2.6b, and 2.6c. In these figures, the magnetic field B is plotted as a vector field to show the magnetization of the magnets involved. The color plot indicates the magnitude of the H field where the color scale has been specified such that all pink areas indicate demagnetization. On the left, two magnets with opposing magnetization are simulated. As the magnets here are placed slightly apart one can see that the value of H_{total} remains below the demagnetization criterion. However, when the magnets are placed together such that their north poles almost touch (figure 2.6b), partial demagnetization occurs in a small area around the facing poles (indicated with the pink color). Demagnetization can also occur when two magnets are placed on either side of a third magnet which has a magnetization in the opposite direction (figure 2.6c). In this case, the middle magnet gets demagnetized.

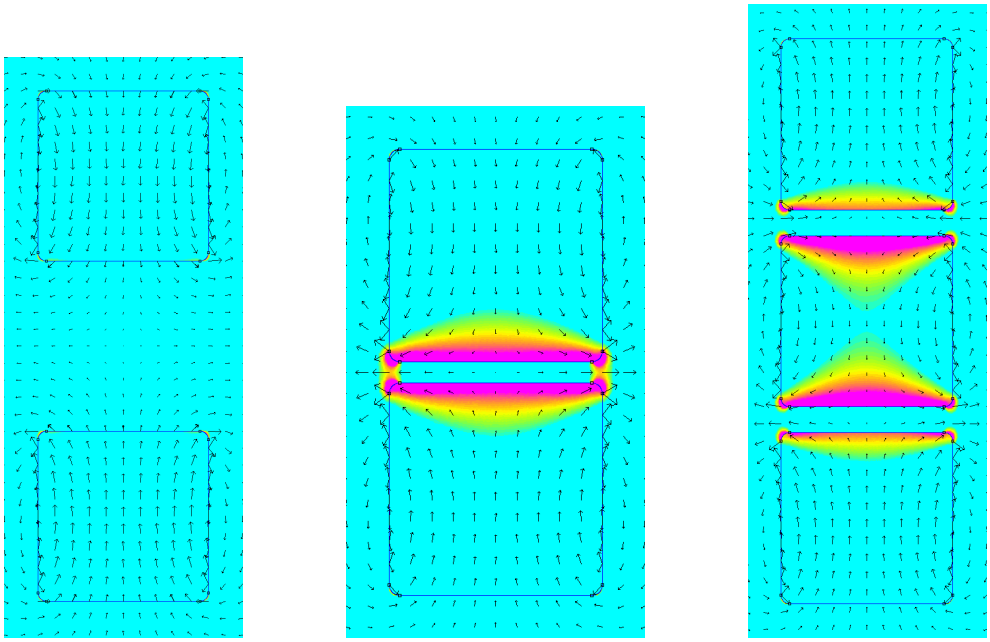

(a) No demagnetization.

(b) Demagnetization occurs at the facing surfaces.

(c) Demagnetization of (mainly) the middle magnet.

Figure 2.6: Examples of demagnetization of permanent magnets.

2.1.4. TEMPERATURE DEPENDENCY OF MAGNET PARAMETERS

So far, the parameters B_r, $H_{c,B}$, and $H_{c,i}$ have been discussed. These are the most important as they provide the information needed to model permanent magnets. Up to this point these parameters have been assumed fixed, however, in practice, these are temperature dependent. The remanence B_r decreases with increasing temperature. At higher temperatures the thermal kinetic energy of molecules is higher, therefore increasing their random movement, and reducing the alignment of the magnetic domains. For the coercivity, a similar argument can be made. The temperature dependency is generally expressed as a percentage per degree Celsius of temperature change. Typical values for the reversible temperature coefficients are listed in table 2.2.

Table 2.2: Typical Temperature Dependency of Rare-Earth Magnets (values are taken from [1] section 1.20, table 1.9).

	$SmCo_5$	$NdFeB$
Maximum service temperature ($^\circ C$)	250	150
B_r Reversible temperature coefficient [%/$^\circ C$]	−0.04	−0.12
$H_{c,i}$ Reversible temperature coefficient [%/$^\circ C$]	−0.30	−0,60

2.2. MODELING OF PERMANENT MAGNETS

Four different modeling techniques were found in the literature that can be used to find the interaction forces between permanent magnets. Each will be explained in detail in the following subsections, along with some of their pros and cons.

2.2.1. DIPOLE MODEL

The simplest method for calculating the force between two magnets is to represent both as an infinitesimally small current loop referred to as a dipole. The concept of a dipole is similar to the concept of a point charge in the electrical domain, however, as magnetic monopoles do not exist, a dipole is used. Mathematically the dipole is represented as a vector $\boldsymbol{m}$.

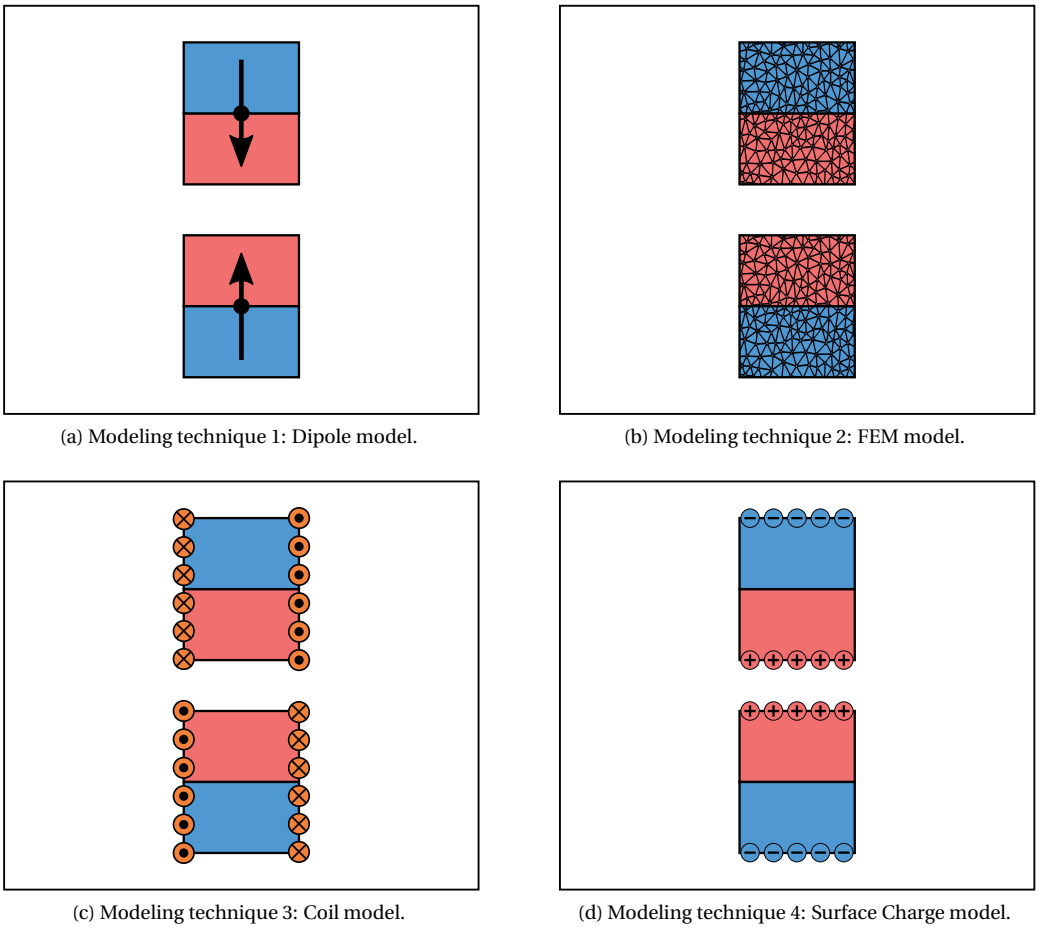

(a) Modeling technique 1: Dipole model.

(b) Modeling technique 2: FEM model.

(c) Modeling technique 3: Coil model.

(d) Modeling technique 4: Surface Charge model.

Figure 2.7: Four modeling techniques for the calculation of the interaction forces between permanent magnets.

The force on a magnetic dipole in an external magnetic field can be calculated using

$$\boldsymbol{F} = \nabla(\boldsymbol{m} \cdot \boldsymbol{B}), \tag{2.7}$$

where ∇ is the differential operator. If the assumption is made that the magnetization over the magnet is uniform, the size of the dipole vector $\boldsymbol{m}$ can be determined by integrating the magnetization over the volume V of the permanent magnet.

$$\boldsymbol{m} = \int_V d\boldsymbol{m} = \int_V \boldsymbol{M} d\tau' = \boldsymbol{M} \int_V d\tau' = \boldsymbol{M}V \tag{2.8}$$

From equation 2.2 and the $B-H$ curve, it can be seen that for $H = 0$ the magnetic field $B_r = \mu_0 M$. The size of the magnetization can therefore be computed as

$$|\boldsymbol{m}| = m = \frac{1}{\mu_0} B_r V. \tag{2.9}$$

The magnetic field produced by a dipole can be determined using

$$\boldsymbol{B}(\boldsymbol{r})_{dip} = \frac{\mu_0}{4\pi} \frac{1}{r^3} \left[3(\boldsymbol{m} \cdot \hat{\boldsymbol{r}})\hat{\boldsymbol{r}} - \boldsymbol{m}\right]. \tag{2.10}$$

Here $\boldsymbol{r}$ represents the field point at which the magnetic field is to be determined, and $\boldsymbol{m}$ is the dipole moment of the permanent magnet ([3]). $\hat{\boldsymbol{r}}$ and r are the unit vector from the location of the magnet and the field point $\boldsymbol{r}$, and the total distance between the magnet and point $\boldsymbol{r}$ respectively. The force on magnet a due magnet b can now be computed using equation 2.7, where the field B_{ext} is computed 2.10.

An example calculation is presented here, where the interaction force F is to be determined between two equal and opposing magnets (see figure 2.8a), where F is the force on magnet a due to magnet b. Firstly, equation 2.7 is expanded using Cartesian coordinates. In matrix notation this results in

$$\begin{bmatrix} F_x \\ F_y \\ F_z \end{bmatrix} = \begin{bmatrix} m_x \frac{\partial B_x}{\partial x} + m_y \frac{\partial B_y}{\partial x} + m_z \frac{\partial B_z}{\partial x} \\ m_x \frac{\partial B_x}{\partial y} + m_y \frac{\partial B_y}{\partial y} + m_z \frac{\partial B_z}{\partial y} \\ m_x \frac{\partial B_x}{\partial z} + m_y \frac{\partial B_y}{\partial z} + m_z \frac{\partial B_z}{\partial z} \end{bmatrix}. \tag{2.11}$$

Here m_x, m_y, and m_z represent the dipole moments of magnet a in the $x-$, $y-$, and $z-$directions. In the example situation $\boldsymbol{m}_a$ and $\boldsymbol{m}_b$ are both aligned with the $z-$ axis, therefore resulting in $m_x = m_y = 0$. This allows for the simplification of equation 2.11 into

$$\begin{bmatrix} F_x \\ F_y \\ F_z \end{bmatrix} = \begin{bmatrix} m_z \frac{\partial B_z}{\partial x} \\ m_z \frac{\partial B_z}{\partial y} \\ m_z \frac{\partial B_z}{\partial z} \end{bmatrix}. \tag{2.12}$$

The field created by magnet b can be calculated using equation 2.10 by taking $\boldsymbol{m_b} = m_z\hat{\boldsymbol{z}}$, $\hat{\boldsymbol{r}} = \hat{\boldsymbol{z}}$, and $r = z$, resulting into

$$\boldsymbol{B}_b = \frac{2\mu_0 m_a}{4\pi z^3}\hat{\boldsymbol{z}}. \tag{2.13}$$

Combining equations 2.12 and 2.13 the force F on magnet a results in the simple expression

$$\begin{bmatrix} F_x \\ F_y \\ F_z \end{bmatrix} = \begin{bmatrix} 0 \\ 0 \\ \frac{3\mu_0 m_a m_b}{2\pi z^4} \end{bmatrix}. \tag{2.14}$$

From this result, the exponential character of the force-displacement curve can be recognized, which is also plotted for two identical cuboidal magnets a and b, where $m_a = m_b = 1.05\,[Am^2]$ of dimensions $width \times depth \times height = 10 \times 10 \times 10$ $[mm]$ with a remanence of 1.33 $[T]$.

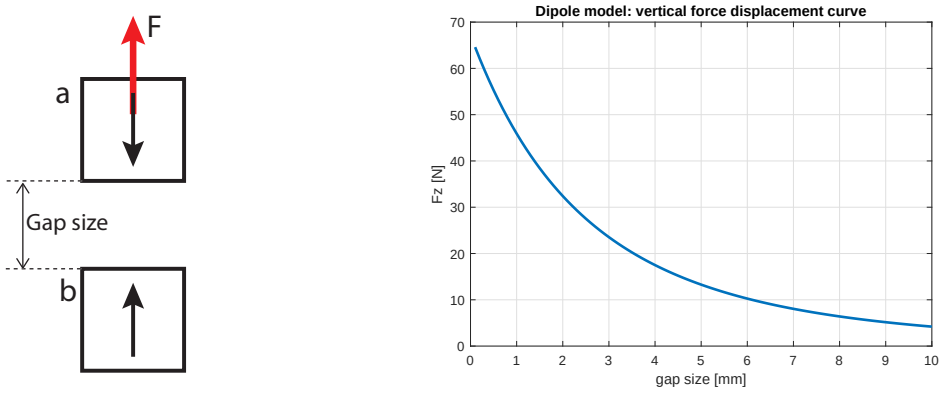

(a) Two facing magents with dimensions $w \times d \times h$ and gapsize g.

(b) Graph of the force F versus gapsize g.

Figure 2.8: Force interaction between two equally sized, opposing magnets calculated with the dipole model.

The general equation for calculating the force between two permanent magnets can be found by combining 2.7 and 2.10 (presented in [4]), resulting into

$$\boldsymbol{F} = \frac{3\mu_0}{4\pi r^4}\left[(\hat{\boldsymbol{r}} \times \boldsymbol{m}_a) \times \boldsymbol{m}_b + (\hat{\boldsymbol{r}} \times \boldsymbol{m}_b) \times \boldsymbol{m}_a - 2\hat{\boldsymbol{r}}(\boldsymbol{m}_a \cdot \boldsymbol{m}_b) + 5\hat{\boldsymbol{r}}((\hat{\boldsymbol{r}} \times \boldsymbol{m}_a) \cdot (\hat{\boldsymbol{r}} \times \boldsymbol{m}_b))\right]. \tag{2.15}$$

An advantage of this model is that it is easy to implement as only simple vector operations are required, making it also a computationally light model. Also, there are no issues caused by numerical noise since it is an analytical model.

The disadvantages are that the dipole representation of a permanent magnet is a very crude approximation. Only the total volume of the magnet is used to calculate the magnetic dipole while the shape of the magnet is completely neglected. Generally, as a rule of thumb, it is advised to only use the dipole model as an approximation for cases where the distance between the magnets is at least larger than 5 times the longest magnet dimension. This presents a huge limitation on the usability of this model as small gap sizes are expected. This limitation is visualized in figure 2.9, where the magnetic field produced by a magnet and a small current loop are compared. From this figure it can be observed that at larger distances the fields are very comparable, however, in close proximity, this is no longer the case.

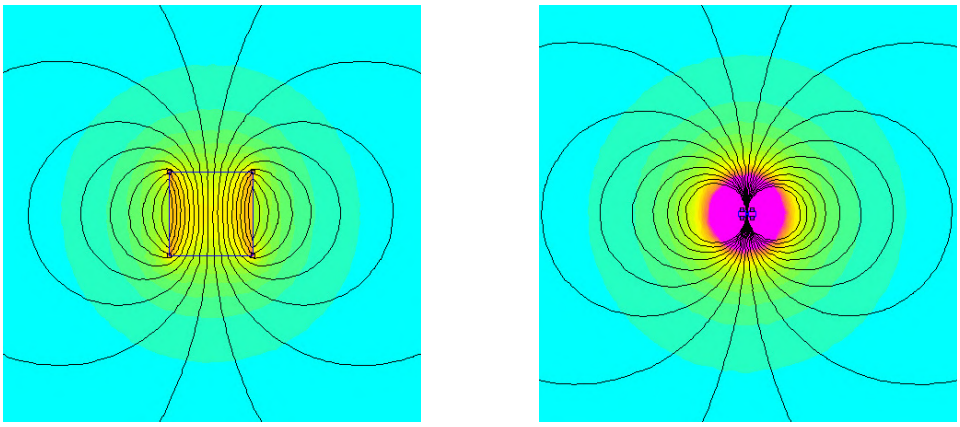

(a) Magnetic field created by a permanent magnet.

(b) Magnetic field created by a very small current loop.

Figure 2.9: Comparison of the magnetic field produced by a magnet and a small current loop.

2.2.2. FINITE ELEMENT METHOD MODEL

When using a Finite Element Method approach, permanent magnets and the air surrounding them are subdivided into small discrete regions called elements. Material properties are specified for all the elements together with boundary conditions on the edges of the finite domain of the simulation. When all information is specified, the computer solves the needed differential equations to find the resulting magnetic fields. In figure 2.10 an example of these steps can be seen where a magnet is modeled in free space, and the magnetic field is computed. When the magnetic field is calculated, the force on permanent magnets can be calculated by integrating the Maxwell Stress Tensor over a surface around the geometry. Generally, a function to do this has already been implemented in the software.

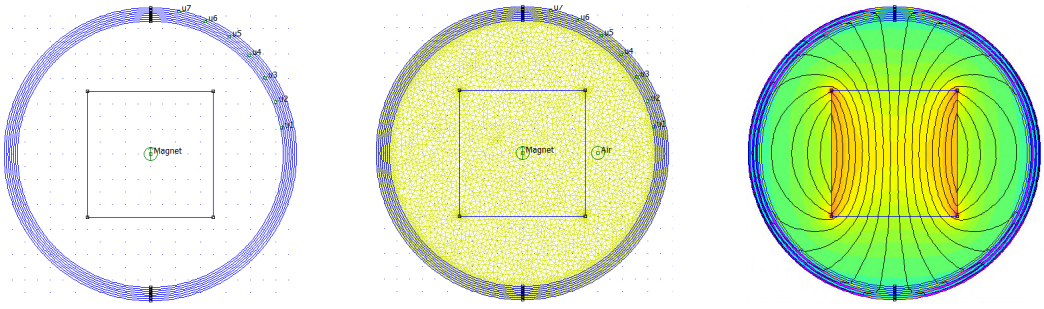

(a) Problem definition.

(b) Mesh.

(c) Results.

Figure 2.10: Example of the steps involved with the FEM workflow.

There are many different commercially available finite element software packages capable of performing such simulations. A few examples are COMSOL, Ansys MAXWELL, and Finite Element Method Magnetics (FEMM). This last package is a simple, yet very capable 2D package that is available for free. It can be linked with MATLAB and other scripting languages, therefore allowing for iterative calculations. This is very useful when force-displacement curves need to be determined, like with a gravity compensator.

Permanent magnets are modeled by defining their $B-H$ curve. In the non-linear case, points on the $B-H$ curve can directly be entered into the material definition options. However when modeling linear materials, like rare-earth magnets, only two parameters need to be defined namely: the normal coercivity $H_{c,B}$, and the relative permeability μ_r. This completely defines the material in the linear case as can be seen from equation 2.3.

Special care must be taken when defining the magnetic material using the supplier's datasheet. Directly using the specified value for $H_{c,B}$ can lead to an incorrect definition, depending on the material. This is visualized in figure 2.11. In the case that the knee of the $B-H$ curve is located below the H axis (2.11a), the datasheet value for $H_{c,B}$ can directly be used in the material definition section of the FEM software. However, when this is not the case (2.11b), the linear section of the $B-H$ curve needs to be extrapolated, to find the needed $H^*_{c,B}$ that correctly models the specified material. It is therefore advised to always check the $B-H$ diagrams of the supplier, and not only rely on the numerical values specified in the material tables.

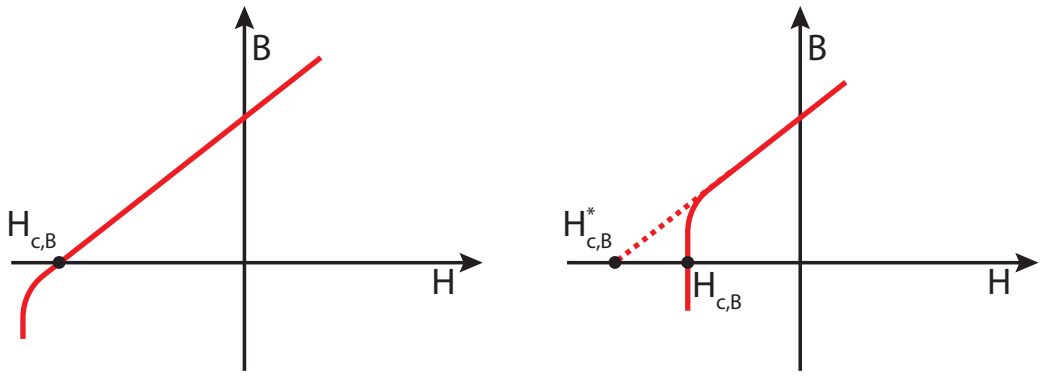

(a) Magnetic material where the knee of the curve is below the H axis.

(b) Magnetic material where the knee of the curve is above the H axis, therefore extrapolation is required.

Figure 2.11: Typical $B-H$ curves for rare-earth permanent magnets.

The advantages of using FEM software are that it is generally easy to use. The complicated mathematical expressions and calculations are taken care of by the computer. The interface of the program generally allows for easy post-processing and visualization of the results without the need for programming. Also, the geometrical form freedom is an advantage, as the shape of the magnets can be chosen completely free. Furthermore, the modeling of soft ferromagnetic materials can be handled easily by FEM packages. These last two points are not the case for other modeling methods. Finally, as already mentioned earlier, some of these packages can be linked with scripting languages like MATLAB and Python, allowing for iterative calculations, making it a strong design tool.

The disadvantages are that FEM packages are very slow, as the differential equations need to be solved over the entire domain, which is a computationally heavy process. Also, the level of numerical noise is much higher than with analytical models. For the design of a gravity compensator, noise is a serious limitation of this modeling technique. This can be explained by looking at a schematic example where the force-displacement curves are calculated using FEM, from which the stiffness needs to be derived (figure 2.12).

For this purpose, the force onto a magnet is determined in two positions with distance Δx. Due to the numerical noise, an error e is present in the force calculation. To simplify the example it is assumed that the error in the obtained force is zero at location 1. The computed stiffness K between points 1 and 2 can now be calculated as

$$K = \frac{\Delta F}{\Delta x} = \frac{F_2 - F_2}{\Delta x} = \frac{K_{true} \cdot \Delta x + e}{\Delta x} = K_{true} + \frac{e}{\Delta x}, \tag{2.16}$$

where K_{true} is the true stiffness of the magnetic configuration. For magnetic designs with a high true stiffness the contribution of the error force is low. This is visualized in 2.12a, however, as the stiffness of the magnetic design is reduced, the error e with respect to the true stiffness increases, which results in larger errors in the computed stiffness (figure 2.12b). This poses a serious limitation of this modeling technique as low stiffnesses are required for a magnetic gravity compensator. The only way to reduce the error is to increase the mesh size which also increases the computational time. An actual example of this problem can be seen in figure 2.13,

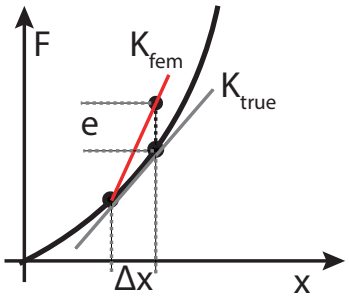

(a) A design with a high true stiffness results in smaller errors in the computed stiffness.

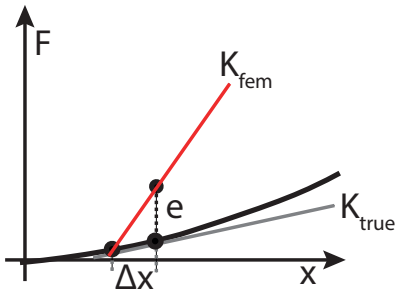

(b) A design with a low true stiffness results in high errors in the computed stiffness.

Figure 2.12: Schematic visualization of the stiffness computation using FEM which show that, in designs with low stiffness, noise becomes more significant.

where the force displacement curve is calculated over the $x-$ and $z-$directions. Subsequently, the stiffnesses are computed, from which is clear that the noise level is making it difficult to determine the true stiffness of the design.

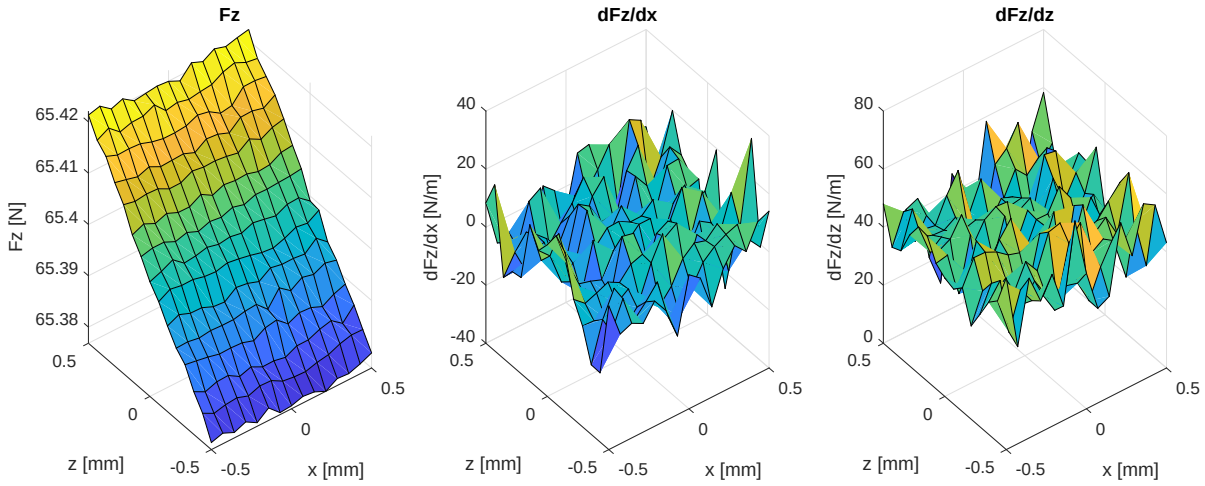

Figure 2.13: Noise in the force-displacement curve (left) from FEM results in very noisy and unclear stiffness plots (middle and right).

2.2.3. COIL MODEL

In this modeling technique, permanent magnets are represented by a coil equivalent. To understand why this is possible, one needs to go back to the magnetic domains discussed in section 2.1. Let us consider a thin piece of uniformly magnetized material as shown with all magnetic domains aligned. All the magnetic domains can be represented by a small current loop as explained in subsection 2.2.1. This is visualized in figure 2.14a. From this figure, it can be observed that all the adjacent currents in fact cancel, except for those around the perimeter of the magnetic material. Therefore, the magnet can be seen as a surface current carried over the outside surfaces of the material (figure 2.14b).

To find the magnetic field produced by a current distribution, the Biot-Savart law can be used. For a surface current this can be written as

$$\boldsymbol{B}(\boldsymbol{r}) = \frac{\mu_0}{4\pi} \int \frac{\boldsymbol{K}(\boldsymbol{r}') \times \hat{\boldsymbol{\imath}}}{\imath^2} da', \tag{2.17}$$

where $\boldsymbol{r}$ represents the field point at which the magnetic field is to be determined. $\boldsymbol{r}'$ is the location of the source point and $\boldsymbol{\imath}$ is the vector from the source point to the field point (equation is taken from [3]). What this equation implies is that to find the field at a point in space due to a current distribution, the integral over

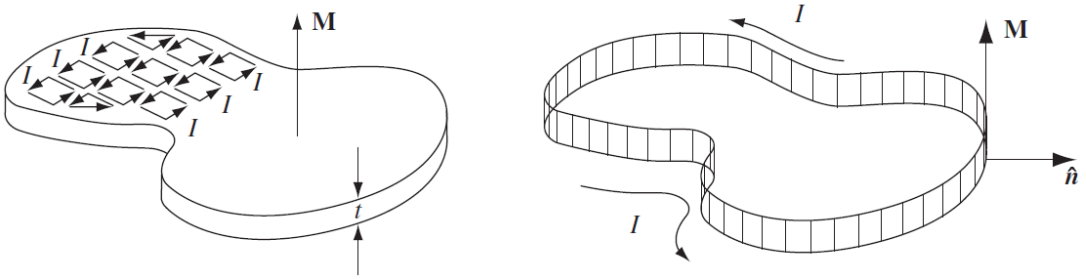

(a) Uniformly magnetized material represented as a collection of current loops (dipoles).

(b) The internal currentloops cancel, resulting in a current around the perimeter of the material.

Figure 2.14: Schematic visualization of the coil representation of a permanent magnet (images taken from [3]).

the current distribution should be taken.

To illustrate that this method can be used, a comparison is made using FEM, where a magnet is modeled both as a permanent (left) and as a thin current sheet (right). As can be seen from the results in figure 2.15, the fields are very comparable.

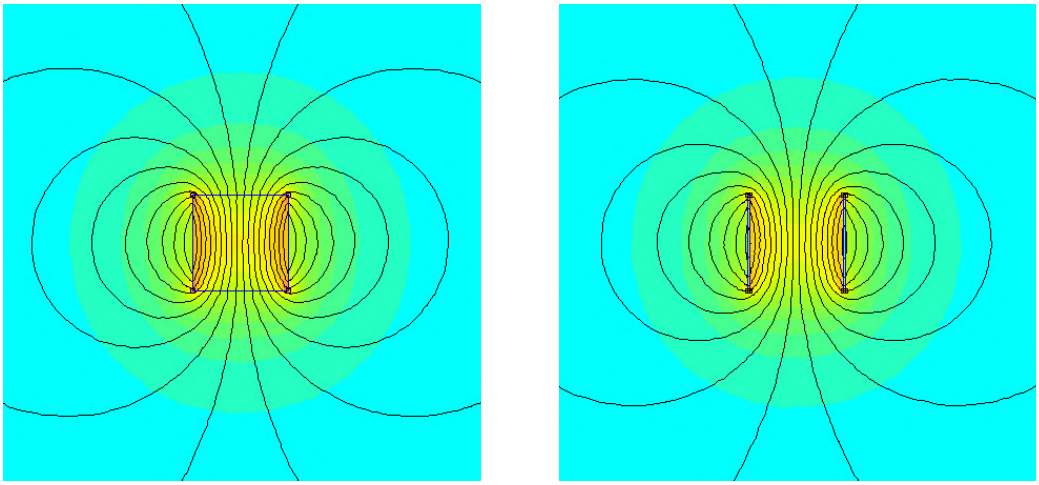

(a) Magnetic field created by a permanent magnet.

(b) Magnetic field created by a thin current sheet.

Figure 2.15: Comparison of the magnetic field produced by a permanent magnet and a thin current sheet.

The next step in this modeling technique is to find the force on a magnet inside a present magnetic field. This can be accomplished using the Lorentz Force law which gives the force on a charged particle moving through a magnetic field. For current sheets, this results in

$$\boldsymbol{F}_{mag} = \int (\boldsymbol{K} \times \boldsymbol{B}) da. \tag{2.18}$$

Here $\boldsymbol{K}$ is the vector describing the equivalent surface current, and $\boldsymbol{B}$ is the external field. So in other words, the cross-product between the current sheet of the magnet and the external field needs to be integrated over the entire surface of the magnet.

The surface current of the magnet is equal to $\frac{1}{\mu_0} B_r$. It is here that rare-earth magnets show their modeling advantage. As explained, rare-earth magnets have a μ_r close to one, meaning that their magnetization is very independent on external fields. Therefore, the external field can be neglected, and the magnetization can be assumed constant. In other words, the surface current can also be assumed constant, therefore simplifying the implementation substantially.

The advantage of this modeling approach is that it can also be implemented analytically with all the accompanying advantages (computationally light and low noise levels).

The disadvantages however are that unfortunately only a few analytical expressions are known for the Biot-Savart law for different geometries. This limits the form freedom if more exotic magnet shapes are desired. Luckily for cuboidal magnets, the expressions are known. However, the expressions are still rather cumbersome.

However, the coil model is really useful for the design of a magnetic gravity compensator in 2D, especially in combination with Finite Element Modeling. In this case, FEM can be used to calculate the magnetic field resulting from the stator for example. This can be done using a very fine mesh, as it is only required to do this once, after which the magnetic field can be extracted. Subsequently, the Lorentz force law can be used in a numerical integration over the mover magnet geometry giving the resulting force. This numerical integration is also relatively light, therefore making this a fast and easy modeling method. The advantage of this approach is that it omits the need for the Biot-Savart law, resulting in higher form freedom.

There is, however, an even greater advantage to these combined methods as the coil representation provides a huge understanding of the fundamental principles of how a gravity compensator works. This will be discussed in more detail in section 4.2.

2.2.4. SURFACE CHARGE MODEL

The last model under consideration is the surface charge model, where a permanent magnet is represented as positive and negative charges on the pole surfaces. Similar to the coil model, the surface charge model can only be used for magnets with a μ_r close to one, as is the case for rare-earth magnets. The surface charge density should be taken equal to $\frac{1}{\mu_0} B_r$.

Many studies have been done exploring the possibilities of this model for different magnet geometries and orientations. The most relevant for this study the cases where the interaction force between cuboidal magnets is calculated between two magnets with parallel and perpendicular magnetization.

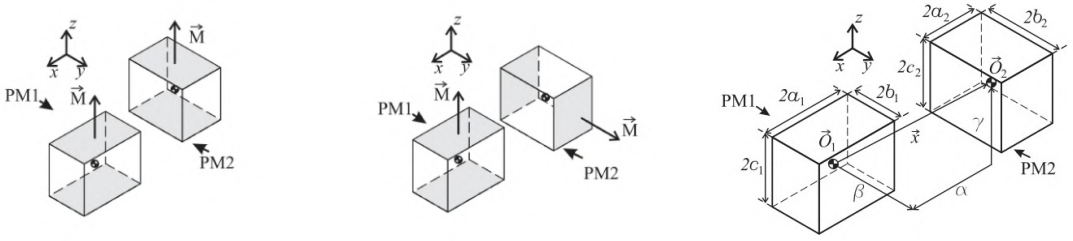

(a) Coordinate definitions in the case of parallel magnetization.

(b) Coordinate definitions in the case of perpendicular magnetization.

(c) Definitions of dimensions and relative displacment.

Figure 2.16: Definitions that need to be used in the surface charge model (figures taken from [5]).

The general equation for the force between two cuboidal magnets is given by ([5])

$$\boldsymbol{F} = \frac{B_{r1} B_{r2}}{4\pi\mu_0} \sum_{i=0}^{1}\sum_{j=0}^{1}\sum_{k=0}^{1}\sum_{l=0}^{1}\sum_{m=0}^{1}\sum_{n=0}^{1} (-1)^{i+j+k+l+m+n} \boldsymbol{\xi}(u,v,w). \tag{2.19}$$

Here B_{r1} and B_{r2} are the remnant flux densities of magnet 1 and 2 respectively. For the parallel case the $\boldsymbol{\xi}$ is given by

$$\xi_x = \frac{1}{2}\left(v^2 - w^2\right)\log\left(r-u\right) + uv\log\left(r-v\right) + vw\arctan\left(\frac{uv}{rw}\right) + \frac{1}{2}ru \tag{2.20}$$

$$\xi_y = \frac{1}{2}\left(u^2 - w^2\right)\log\left(r-v\right) + uv\log\left(r-u\right) + uw\arctan\left(\frac{uv}{rw}\right) + \frac{1}{2}rv \tag{2.21}$$

$$\xi_z = -uw\log\left(r-u\right) - vw\log\left(r-v\right) + uv\arctan\left(\frac{uv}{rw}\right) - rw, \tag{2.22}$$

and for the perpendicular case $\boldsymbol{\xi}$ is given by

$$\begin{aligned}\xi_x = \frac{1}{2}\Big[&\left(\tan^{-1}\left(\frac{w}{u}\right)+\tan^{-1}\left(\frac{vw}{uR}\right)\right)u^2+2vu-3wu-2uv\log(w+R)-2v^2\tan^{-1}\left(\frac{u}{v}\right)\\&+w\left(w\left(2\tan^{-1}\left(\frac{u}{w}\right)+\tan^{-1}\left(\frac{w}{u}\right)+\tan^{-1}\left(\frac{uv}{wR}\right)\right)-2v\log(u+R)+2u\log(R-v)\right)\\&+v^2\tan^{-1}\left(\frac{uw}{vR}\right)\Big]\end{aligned} \tag{2.23}$$

$$\begin{aligned}\xi_y = \frac{1}{2}\Big[&[w(r-2u)-(u-v)(u+v)\log(w+r)\\&+2u\left(v\left(\tan^{-1}\left(\frac{w}{v}\right)+\tan^{-1}\left(\frac{uw}{vr}\right)\right)+w\log(r-u)\right)\Big]\end{aligned} \tag{2.24}$$

$$\begin{aligned}\xi_z = \frac{1}{2}\Big[&[v(r-2u)+\left(w^2-u^2\right)\log(v+r)\\&+2u\left(w\left(\tan^{-1}\left(\frac{v}{w}\right)+\tan^{-1}\left(\frac{uv}{wr}\right)\right)+v\log(r-u)\right)\Big].\end{aligned} \tag{2.25}$$

The intermediary variables u, v, w, and r depend on the dimensions and the relative position of the two magnets.

$$u = \alpha-(-1)^i a_1+(-1)^j a_2 \tag{2.26}$$

$$v = \beta-(-1)^k b_1+(-1)^l b_2 \tag{2.27}$$

$$w = \gamma-(-1)^m c_1+(-1)^n c_2 \tag{2.28}$$

$$r = \sqrt{u^2+v^2+w^2} \tag{2.29}$$

A very important aspect in this model is that the definitions of the axis systems and magnet dimensions should be implemented in accordance with the definitions seen in figures 2.16a, 2.16b, 2.16c.

The pro's of this model is that it is computationally light as it is an analytical model. Meaning it is fast and that the noise levels are very low. Also, as it has been studied in multiple pieces of research, the reliability is high.

The downsides of this model is that the equations are very cumbersome. Even though implementing them into a scripting language is not difficult, the chances of making typos are high. Also, they do not provide any design insight. Finally, the application is limited to the cases that have been studied and for which equations have been derived, therefore posing some limitations on the usability.

2.3. COMPARISON BETWEEN MODELS

A comparison between all the models was made with the purpose to determine the limitations and the usability of all the models. The implemented models are the dipole model, the finite element method using FEMM, a combination between FEM and the coil model, and the 3D surface charge model. Important to mention is that both the direct FEM model and the hybrid between FEMM and the coil model, are 2D models. For the comparison, two simple calculations of the force-displacement curve have been implemented which are shown in figures 2.17a and 2.17b. The magnets have opposing magnetization in both cases, but in 2.17a the top magnet is moved in the vertical direction w.r.t. the bottom one. While in 2.17b the top magnet is moved in the horizontal direction. The following two subsections show the results and the most significant conclusions.

2.3.1. LIMITATIONS DIPOLE MODEL

As described in subsection 2.2.1 has serious limitations in terms of applicability. This is shown in the following two comparisons. For the first case the magnet dimensions are taken as $w \times d \times h = 10 \times 10 \times 10$ $[mm]$. From the results seen in the top figures of 2.18 (case 1), it can be concluded that all models are showing similar force-displacement curves. However, when the dimensions of both magnets are changed to $w \times d \times h = 40 \times 40 \times 10$ $[mm]$ (case 2), a huge overestimation of the force by the dipole model is observed (see bottom figures 2.18). This is not the case with the other models. This shows that the dipole model is indeed a crude approximation and that it has only very limited applicability.

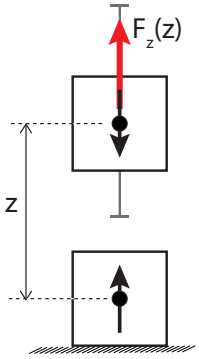

(a) Force displacement curve of the vertical force F_z as a function of z.

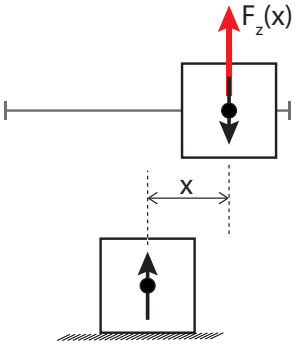

(b) Force displacement curve of the vertical force F_z as a function of x.

Figure 2.17: Schematic representation of the calculated force-displacement curves.

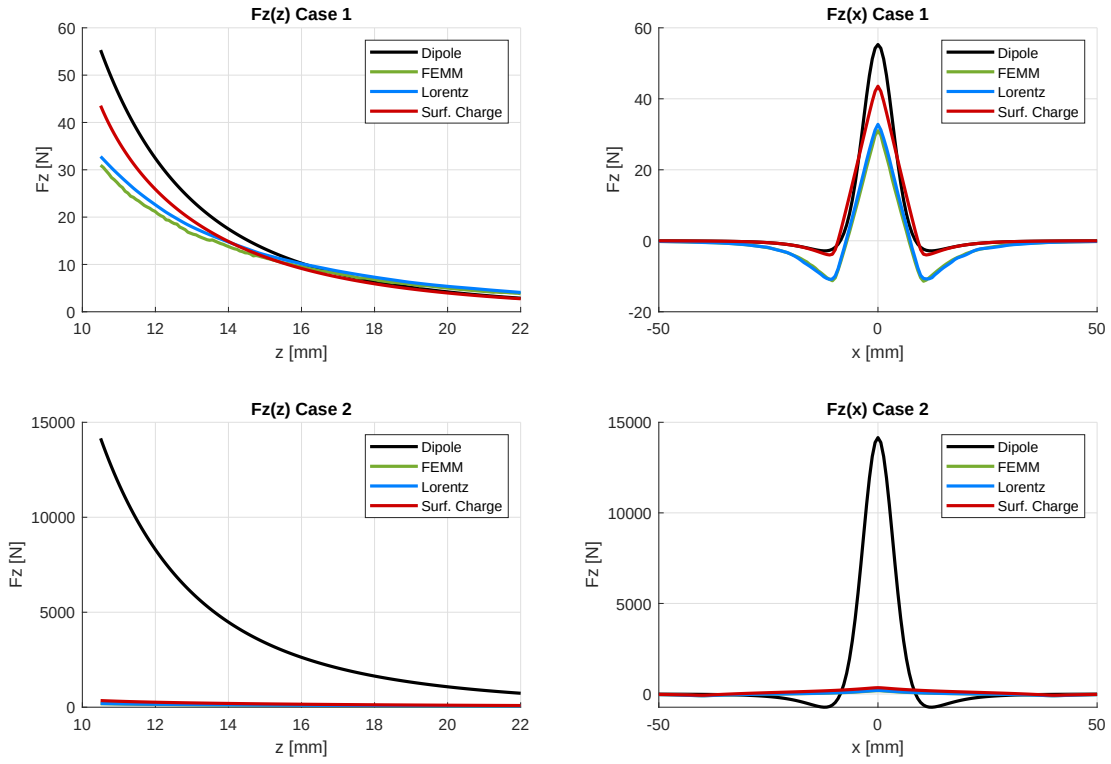

Figure 2.18: Force displacement curves of all models showing the limitations of the dipole model.

2.3.2. LIMITATIONS 2D FINITE ELEMENT MODELING

As mentioned above, the model implementation of the finite element method and the FEM-coil model hybrid are implemented in 2D. To find out what the limitations are of these 2D models, a comparison is made with the 3D surface charge model. This is done for different depths of the magnets. The dipole model is left out of this comparison to make the results more readable. The depths that are used are $d = 100$, $d = 10$, and $d = 1$ $[mm]$. It is expected that the greater the depth of the magnets, the better the 2D approximation as the 3D effects become less significant for greater magnet depths. The results are shown in figure 2.19.

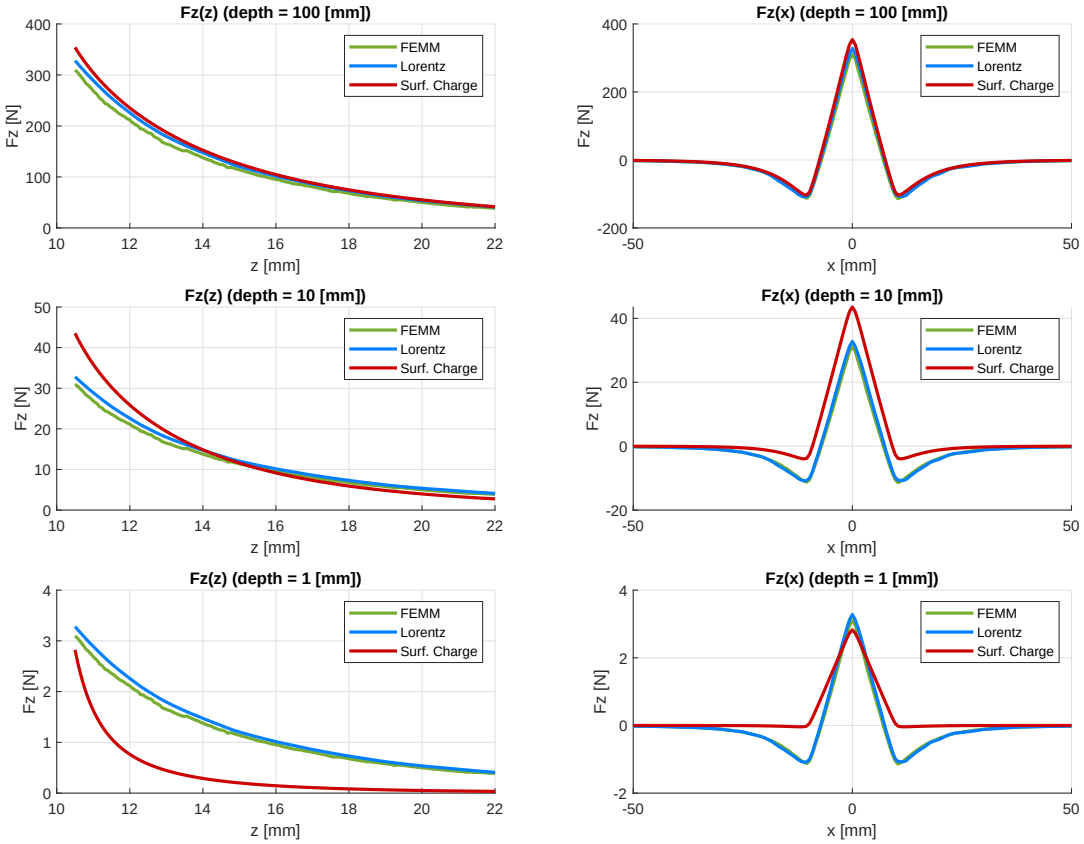

Figure 2.19: Force displacement curves showing the limitations of 2D modeling of the interaction forces between permanent magnets.

The results show indeed that magnets where the depth is a factor 10 times higher than the other dimensions, the results are good. However, when the depth is in the same order of magnitude as the other dimensions, the maximum error is already approximately 25%, and for the case of $d = 1$ $[mm]$ the results are quite bad. The results from the 2D model also show the same behavior, which is just scaled in accordance with the depth of the magnets. While on the other hand, the 3D model shows that the depth of the magnet also influences the shape of the force-displacement curve.

2.3.3. CONCLUSIONS

The comparison between the different models has shown that the dipole model does not give the correct interaction forces between permanent magnets reliably. It only works in special cases, where the magnet dimensions are in the same order of magnitude. Due to this limitation, it is concluded that the dipole model is not a suitable design tool for a magnetic gravity compensator.

Even though the dipole approximation cannot be used as a design tool, it still is an important fundamental quantity in the theory of electromagnetism, and it is used in the measurement of permanent magnet parameters, as will be explained in more detail in section 5.4. Therefore it is still a valuable concept to understand.

From the comparison presented in subsection 2.3.2 it is concluded that 2D models can be used as a design tool, however, it is advised to check the results using a three-dimensional method. For the initial design of the magnetic gravity compensators, it is chosen to use the hybrid model making use of the advantages from FEM (easy implementation) and the coil model (provides design insight). This will be elaborated in section 4.2.

3

State of the Art Study

The force between two repelling magnets increases exponentially with the inverse of the distance between the magnets. This can be seen from the comparison between the models (figure 2.19) and from equation 2.14, which can be used to make a quick estimation of the stiffness by taking the derivative to z, resulting in

$$\frac{dF_z}{dz} = \frac{-6\mu_0 m_a m_b}{\pi z^5}. \tag{3.1}$$

Equation 3.1 can be used to find the distance at which the stiffness equals the maximum 1000 $\left[\frac{N}{m}\right]$ from the requirements. If the same magnets are used as in the example described in subsection 2.2.1, the center to center distance required is

$$z = \left(\frac{6\mu_0 m_a m_b}{1000\pi}\right)^{\frac{1}{5}} = \left(\frac{6\mu_0 \cdot 1 \cdot 1}{1000\pi}\right)^{\frac{1}{5}} \approx 0.019\ [m] \approx 19\ [mm]. \tag{3.2}$$

From figure 2.19 it can be seen that for this center-to-center distance between the magnets, equation 2.14 is a good approximation when the magnets are placed further apart. The load capacity created by the repelling force at that distance equals

$$F_z = \frac{3\mu_0 m_a m_b}{2\pi z^4} = \frac{3\mu_0 \cdot 1 \cdot 1}{2\pi \cdot 0.019^4} \approx 4.8\ [N]. \tag{3.3}$$

To obtain the needed load capacity of 196.2 $[N]$ the dimensions of the magnets would have to be increased to roughly $63 \times 63 \times 63$ $[mm]$, with an air gap of 123 $[mm]$. From these estimations, it is clear that two opposing magnets are not capable of providing the required combination of load capacity and low stiffness within the given design volume. Therefore, a literature study has been conducted into magnetic configurations that can provide this required combination. Findings of this investigation are discussed in section 3.1. Subsequently, in section 3.2, a trade-off is made between the different configurations, resulting in two chosen designs that will be investigated in further detail in chapter 4.

Besides the magnetic configurations, also literature regarding the design and implementation of long-stroke gravity compensators has been sought. Unfortunately without much success. The only study into a long stroke gravity compensation system has been found in [6]. Even though this gravity compensator is indeed capable of making a relatively large stroke, the design cannot be used, as the long stroke is in the gravitational direction. Where, for the application in this study, the long-stroke direction is required in the horizontal direction, perpendicular to gravity.

3.1. Magnet Configurations

Four fundamental magnet configurations have been found in the literature that provides a load capacity together with a low stiffness. They are depicted in figures 3.1a through 3.1d. The shading in these figures indicates the magnets that are part of the stator. The remaining magnet, referred to as the mover magnet, feels a resulting upwards force due to the stator magnets, and can therefore be used in a passive support structure like a gravity compensator.

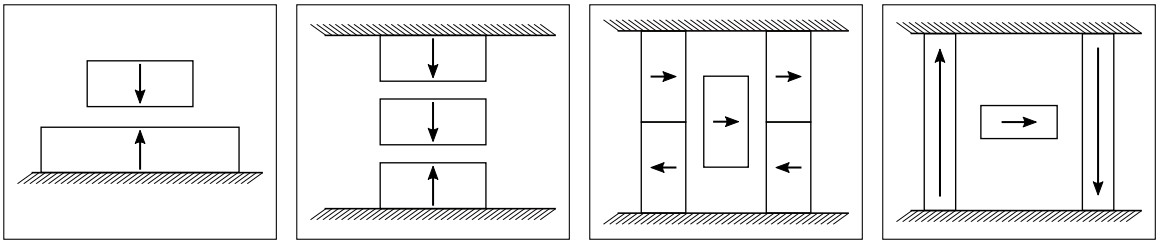

(a) Configuration 1. (b) Configuration 2. (c) Configuration 3. (d) Configuration 4.

Figure 3.1: Fundamental magnetic configurations suitable for the application into a magnetic gravity compensator.

Using a simple FEM analysis, the force-displacement curves in the vertical direction are computed to show the low stiffness characteristic described in the literature. The results of these simulations can be seen in 3.2. Important to note is that the low stiffness only occurs in a local region (indicated with the red rectangles). All the configurations are discussed in more detail in the following subsections.

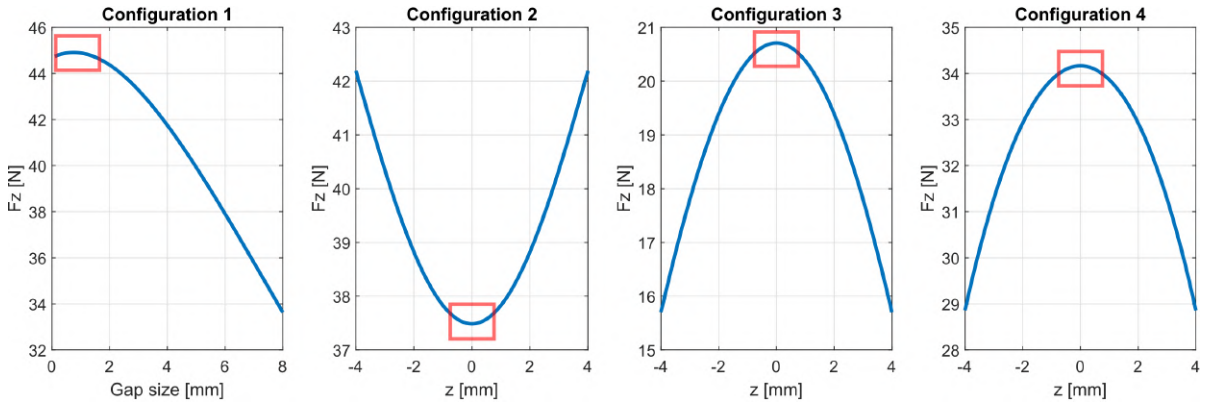

Figure 3.2: Vertical force on the mover magnet as function of the z displacement (or gap size) for all configurations.

3.1.1. CONFIGURATION 1

The first configuration is mainly investigated in the group of Electromechanics and Power Electronics of the Eindhoven University of Technology. As explained in [7] the gravity compensator was intended for a high load application (between 1 and 10 $[kN]$). Another design criterion was to have a simple design with only a single air gap. At first magnets with equal dimensions were studied, but it was concluded that in this case, the stiffness remains too high. By reducing the size of the top magnet, a low stiffness is observed for small air gaps. In [7] and in further studies like [8] and [9] the achievable performance of this topology was examined in detail. It was mainly investigated if a relationship could be found between the number of magnets and their dimensions, and the resulting load capacity and stiffness of the design. Also, the passive limitations of this topology were investigated in [10]. This configuration is also investigated in [5].

3.1.2. CONFIGURATION 2

Configuration two combines a positive stiffness with a negative stiffness to obtain a low total effective stiffness on the mover magnet. This is done by placing a magnet with opposite magnetization below the mover and a magnet with parallel magnetization above the mover. The bottom magnet provides a positive stiffness, while the top magnet provides a negative stiffness, therefore causing a cancellation of the stiffnesses. The load capacity, however, is the summation of the forces from both the bottom and top magnet, resulting in a combination of low stiffness and high load capacity (compared to only two opposing magnets).

A detailed study into the design parameters of this configuration is performed in [11], where the effects of dimensions on load capacity and stability are investigated. Also, a patent was found using this configuration described as a magnetic support system [12].

A slightly more advanced version was designed and validated in [13] where Halbach magnets were used.

3.1.3. CONFIGURATION 3

Magnet configuration number three is the most frequently applied and studied configuration. Even though significant research on configuration one is performed in [7] and [5], the final configuration applied in the experimental setup was configuration three. The static behavior of this configuration was examined and validated in [14].

In [15] and [16] the effects of adding Halbach elements were investigated. On the contrary, in [17], [18], and [19], the topology was reduced to only the top magnets of the stator. In this case, a low stiffness can still be obtained, but it does reduce the force density of the design significantly.

3.1.4. CONFIGURATION 4

Configuration four was first investigated in [20] for a similar application as is required in this study. The magnetic bearing (as it is referred to in this publication) is intended for a nanometer precision application, where it has to be integrated with the actuator. This posed serious limitations on the design space and configurations possible. The study was continued and is described in detail in [21] and [22].

In [23] configuration 3 and 4 were combined also resulting in a good performance. However, this choice was also made to accommodate the integration of the gravity compensator and a Lorentz actuator.

Later the design was slightly adapted for a similar application as described briefly in [24]. This variation was also adopted in [25] for an application in nano-metrology.

3.2. CONFIGURATION TRADE OFF AND CHOICE

To limit the design space, a trade-off is made between the found configurations, where the two most promising options are selected for further investigation. In subsections 3.2.1 and 3.2.2 the criteria and the trade-off choice are discussed respectively. Important to note here is that the information here is mainly based on the reported performance specifications found in the literature. Since the requirements set in each of the studies are quite different, this trade-off is a difficult one. However, as time was also limited in this investigation, a choice had to be made with the available information.

3.2.1. TRADE OFF CRITERIA

The following criteria are used in the trade off:

- **Load capacity**: The reported load capacity found in the literature. Here a higher load capacity is considered positive, as less build volume or magnetic material is required, which is advantageous for the implementation of the gravity compensator.
- **Stiffness**: The reported stiffness found in literature. Clearly, a lower stiffness is considered better than a high stiffness.
- **Build volume**: The total volume described in the literature. This is taken as the outer dimensions, so not only the volume of the magnets but the outer dimensions of the whole design.
- **Force density**: The load capacity per unit of volume. This is generally not specified directly in the literature but can be calculated easily when load capacity and dimensions are given.
- **Stroke**: The possible strokes as reported in the literature.
- **Risk of demagnetization**: Configurations with opposing magnetization have a higher risk of demagnetization. A high risk relates to a high score in this category. This is the only criterion that is not directly taken from literature but judged solely on the orientation of the magnets with respect to each other.

3.2.2. CONFIGURATION CHOICE

The information from the literature that is presented in the trade off table 3.1 is taken mainly from the following publications:

- **Configuration 1:** Information is mainly taken from [7] and [9]
- **Configuration 2:** Information is mainly taken from [11]
- **Configuration 3:** Information is mainly taken from [7], [15], and [16]

- **Configuration 4:** Information is mainly taken from [21].

Table 3.1: Trade Off Matrix between the four fundamental magnet configurations.

Criterion	Config. 1	Config. 2	Config. 3	Config. 4
Load Capacity (Lit.)	$1-10$ $[kN]$	4.9 $[N]$	$1000-71000$ $[N]$	84 $[N]$
Stiffness (Lit.)	$1-2000$ $\left[\frac{kN}{m}\right]$	$30-170$ $\left[\frac{N}{m}\right]$	$700\left[\frac{N}{m}\right]$	$140\left[\frac{N}{m}\right]$
Build volume (Lit.)	Not Specified	$66\times20\times20$ $[mm]^3$	$100\times50\times160$ $[mm^3]$	$32\times\pi\cdot48.5^2$ $[mm^2]$
Force density (Lit.)	-	$1.9\cdot10^{-4}$ $\left[\frac{N}{mm^2}\right]$	$13\cdot10^{-4}$ $\left[\frac{N}{mm^2}\right]$	$3.5\cdot10^{-4}$ $\left[\frac{N}{mm^2}\right]$
Strokes (Lit.)	-	$0.2-7.8$ $[mm]$	2 $[mm]$	2 $[mm]$
Demagnetization Risk	10	6	8	3

In addition to the information found in the literature, the performance of configuration 1 was also briefly investigated using a simple finite element simulation. This resulted into the force-displacement curve seen in figure 3.2. This curve was used to obtain the stiffness in figure 3.3a. From this plot it can be concluded that an air gap below roughly 2.3 $[mm]$ is required to result in a stiffness below 1000 $\left[\frac{N}{m}\right]$. For this low gap size, it was found that the magnets would be demagnetized severely (figure 3.3b where the pink color indicates demagnetized areas). It should be mentioned that at the time of this decision, only the simulation of configuration 1 was made. The force-displacement curves of the other designs seen in figure 3.2 were made later for the purpose of this report.

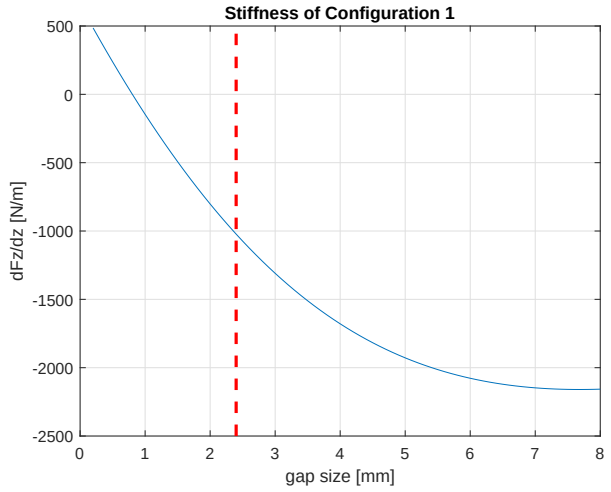

(a) Stiffness of configuration 1 calculated from the force displacement curve from figure 3.2.

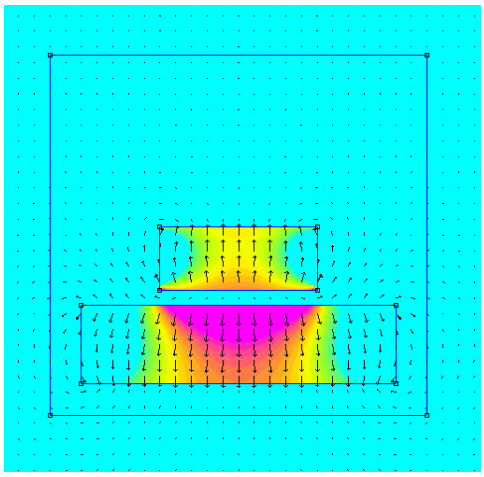

(b) Demagnetization of configuration 1.

Figure 3.3: Performance of configuration 1.

This resulted in the decision to eliminate configuration 1 from the possible options. Subsequently, configuration 3 and 4 were chosen as both have a higher force density than configuration 2. In conclusion: topology 3 and 4 were selected for further investigation which is presented in detail in chapter 4.

4

MAGNETIC DESIGN

4.1. GOALS

In this chapter, the magnetic design is presented. Using the information found in literature the two most promising magnet configurations were selected (see chapter 3). These will be investigated in further detail, to result in a design suitable for the application in a long stroke gravity compensator. The goals to achieve this are:

- **Magnet dimensioning**: Dimension both configurations such that they fulfill the design requirements. As this thesis is exploratory research, it has been decided to limit the design space to only cuboidal magnets.
- **Effect of magnet tolerances and demagnetization**: investigate both the effect of the magnet tolerances and the risk of demagnetization for all configurations. This information can subsequently be used to make a trade-off between the magnet configurations and select the best design for the long stroke gravity compensator.
- **Damping estimation**: The damping is estimated to determine if the design requirement will be met with the chosen design.

To achieve these goals, first the underlying working principles of gravity compensators are investigated (section 4.2). This information is subsequently used in section 4.3 to dimension the magnet configurations under the assumption of ideal magnets. The effect of the magnet tolerances is discussed in section 4.4, after which the risk of demagnetization is evaluated in section 4.5. The results from these two sections are used for the design trade-off (section 4.6). In section 4.7, the final dimensions of the chosen design are determined using a 3D modeling approach where also the required stator length margin is calculated. The damping is estimated in section 4.8, after which the final conclusions are summarized in section 4.9.

4.2. WORKING PRINCIPLES OF MAGNETIC GRAVITY COMPENSATORS

At the beginning of chapter 3 it was shown that not all magnetic configurations are suitable for a gravity compensator. This is due to the required combination of load capacity and a low stiffness. This can only be achieved with certain magnetic configurations like the ones presented in section 3.1. This section will focus on understanding the working principles of the chosen magnet configurations. This information will be crucial for determining the magnet dimensions such that the design requirements are met.

To understand how the chosen configurations work, the coil model is used to analyze the force on the mover magnet as a function of the magnetic field created by the stator. For a magnet with its magnetization in the $x-$direction the resulting coil is shown in figure 4.1b. To simplify the involved equations the analysis is carried out in 2D.

From figure 4.1c it can be seen that the relevant surfaces of the mover magnet are the top and bottom. Using the Lorentz force equation on these surfaces, the force on the mover can be expressed as a function of the

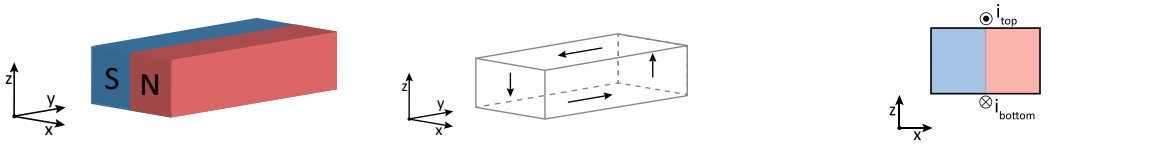

(a) Mover magnet of both configuration 3 and 4 is magnetized in the positive $x-$direction.

(b) Resulting surface current over the surfaces of the mover magnet.

(c) Resulting surface current over the top and bottom surface of the mover magnet.

Figure 4.1: Coil representation of the mover magnet.

magnetic field created by the stator. The general case of the Lorentz force is given by equation 2.18. For the top and bottom surfaces, the current densities are given by

$$\boldsymbol{K}_{top} = -\frac{B_r}{\mu_0}\hat{\boldsymbol{j}}, \tag{4.1}$$

$$\boldsymbol{K}_{bot} = \frac{B_r}{\mu_0}\hat{\boldsymbol{j}}, \tag{4.2}$$

and the magnetic field at the top and bottom surfaces are

$$\boldsymbol{B}_{top} = B_x\hat{\boldsymbol{i}} + B_y\hat{\boldsymbol{j}} + B_z\hat{\boldsymbol{k}} \tag{4.3}$$

$$\boldsymbol{B}_{bot} = B_x\hat{\boldsymbol{i}} + B_y\hat{\boldsymbol{j}} + B_z\hat{\boldsymbol{k}}. \tag{4.4}$$

The symbols $\hat{\boldsymbol{i}}$, $\hat{\boldsymbol{j}}$, and $\hat{\boldsymbol{k}}$ indicate the unit vectors in the $x-$, $y-$, and $z-$directions respectively. Note also that the magnetic field components B_x, B_y, and B_z, are functions of the spatial coordinates x, y, and z, however, this is omitted in the notation here for legibility purposes.

The force on the top and bottom surfaces can now be expressed as

$$\boldsymbol{F}_{top} = \int_{top}\left[\left(-\frac{B_r}{\mu_0}B_z - 0\cdot B_y\right)\hat{\boldsymbol{i}} - (0\cdot B_z - 0\cdot B_x)\,\hat{\boldsymbol{j}} + \left(0\cdot B_y + \frac{B_r}{\mu_0}\cdot B_x\right)\hat{\boldsymbol{k}}\right]da = \frac{B_r}{\mu_0}\int_{top}\left[-B_z\hat{\boldsymbol{i}} + B_x\hat{\boldsymbol{k}}\right]da \tag{4.5}$$

$$\boldsymbol{F}_{bot} = \int_{bot}\left[\left(\frac{B_r}{\mu_0}B_z - 0\cdot B_y\right)\hat{\boldsymbol{i}} - (0\cdot B_z - 0\cdot B_x)\,\hat{\boldsymbol{j}} + \left(0\cdot B_y - \frac{B_r}{\mu_0}B_x\right)\hat{\boldsymbol{k}}\right]da = \frac{B_r}{\mu_0}\int_{bot}\left[B_z\hat{\boldsymbol{i}} - B_x\hat{\boldsymbol{k}}\right]da. \tag{4.6}$$

From equations 4.5 and 4.6 the resulting force on the mover magnet in the $z-$ direction can be expressed as

$$F_z = F_{z,top} + F_{z,bot} = \frac{B_r}{\mu_0}\left(\int_{top} B_{x,top}\,da - \int_{bot} B_{x,bot}\,da\right). \tag{4.7}$$

As a load capacity is required in the positive $z-$ direction, it is required that this expression should not equal to zero, meaning that the magnetic field on the top and the bottom should not be equal. In fact the stator designs of configuration 3 and 4 are both symmetrical such that $B_{x,top} = -B_{x,bot}$. This will later be shown in subsections 4.2.1 and 4.2.2.

The stiffness in the $x-$ and $z-$direction can be derived from equation 4.7 by taking the derivative to the $x-$ and $z-$ coordinates respectively, resulting in

$$\frac{dF_z}{dx} = \frac{B_r}{\mu_0}\left(\int_{top}\frac{dB_{x,top}}{dx}\,da - \int_{bot}\frac{dB_{x,bot}}{dx}\,da\right) \tag{4.8}$$

$$\frac{dF_z}{dz} = \frac{B_r}{\mu_0}\left(\int_{top}\frac{dB_{x,top}}{dz}\,da - \int_{bot}\frac{dB_{x,bot}}{dz}\,da\right). \tag{4.9}$$

As the stiffnesses are required to be low, the situations are examined when equation 4.9 equates to zero. The most trivial case is when the derivatives of the field on both the top and the bottom are zero $\left(\frac{dB_{x,top}}{dz} = 0,\quad \frac{dB_{x,top}}{dz} = 0\right)$, meaning that the magnetic fields are constant. The other option is that the derivatives on the top and bottom

surface are equal $\left(\frac{dB_{x,top}}{dz} = \frac{dB_{x,top}}{dz} = const.\right)$, which can be achieved by creating a linearly growing field with a constant derivative. Note that the same conclusions can be drawn for the derivative in the $x-$direction.

Similar equations for the force in the $x-$ direction and the accompanying stiffnesses can be derived. These are given in equations 4.10 through 4.12. The difference for the force in $x-$direction is that no force is required. This will be elaborated in more detail in the following subsections.

$$F_x = F_{x,top} + F_{x,bot} = \frac{B_r}{\mu_0}\left(-\int_{top} B_{z,top}\, da + \int_{bot} B_{z,bot}\, da\right) \tag{4.10}$$

$$\frac{dF_x}{dx} = \frac{B_r}{\mu_0}\left(-\int_{top} \frac{dB_{z,top}}{dx}\, da + \int_{bot} \frac{dB_{z,bot}}{dx}\, da\right) \tag{4.11}$$

$$\frac{dF_x}{dz} = \frac{B_r}{\mu_0}\left(-\int_{top} \frac{dB_{z,top}}{dz}\, da + \int_{bot} \frac{dB_{z,bot}}{dz}\, da\right). \tag{4.12}$$

To summarize: if a load capacity is required in the $z-$ direction, the B_x field at the top should not equal the B_x field at the bottom. Furthermore, to result in a low stiffness the derivatives of B_x on the top and bottom surfaces of the mover magnet should either be zero if the stator is designed such that it produces a constant magnetic field. Alternatively, the derivatives can also be made equal on the top and bottom by making a linearly growing field. In the next two subsections, the will be investigated for magnetic configurations 3 and 4.

4.2.1. CONFIGURATION 3: CONSTANT MAGNETIC FIELD

To understand the working principles of magnet configuration 3, the magnetic field created by the stator is investigated. This is done by means of a FEM simulation of the stator magnets only, where the magnetic field is extracted around the mover magnet. This is visualized in figure 4.2a.

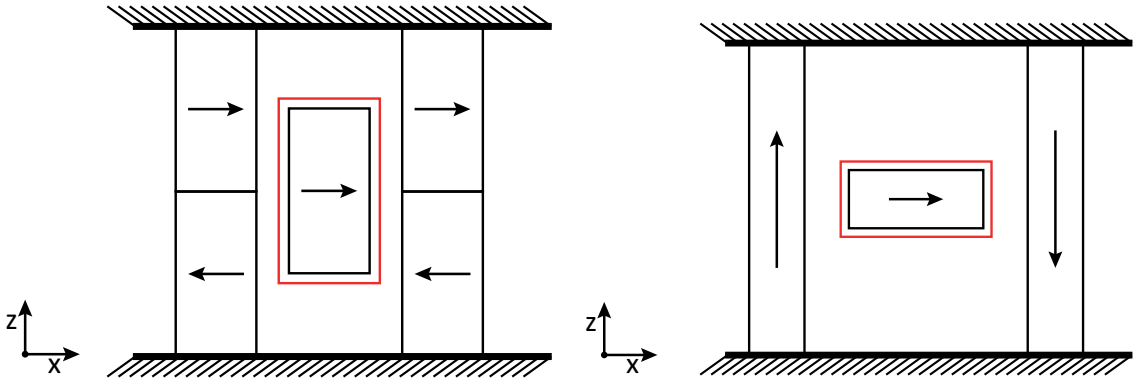

(a) Congiuration 3. (b) Congiuration 4.

Figure 4.2: Regions around the mover magnet, where the magnetic field components B_x and B_z are extracted.

The resulting magnetic fields are plotted as function of the $x-$ and $z-$coordinate in surface plots presented in figure 4.3. The contour of the mover magnet is indicated with the red line.

From figure 4.3 it can be seen that the B_x field at the top and bottom are constant, where $B_{x,top} = -B_{x,bot}$ resulting in a positive force in the $z-$direction providing the needed load capacity. The constant B_x field results in $\frac{dB_x}{dx} \approx 0$ and $\frac{dB_x}{dz} \approx 0$ for both the top and the bottom of the mover magnet, causing the stiffness of F_z to be low. The B_z field is zero around the top and bottom, meaning that no force in the $x-$direction is created. Similarly to the B_x field, the derivatives of B_z are close to zero, resulting in low stiffness of the F_x force.

4.2.2. CONFIGURATION 4: LINEAR MAGNETIC FIELD

Similarly to the analysis of configuration 3, the magnetic field of the stator of configuration 4 is examined around the mover magnet (see 4.2b). The resulting B_x and B_z fields are plotted as function of the $x-$ and

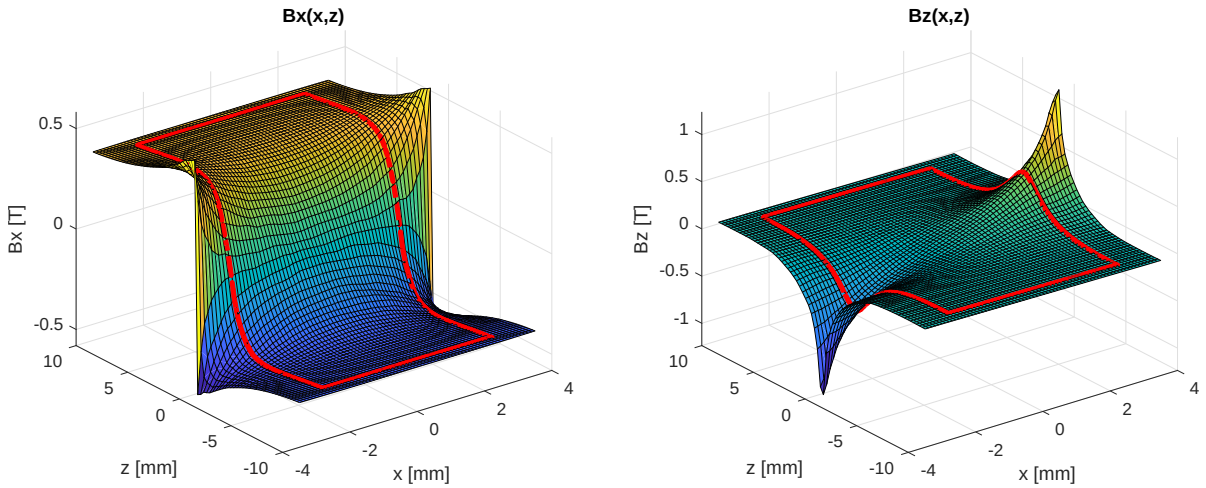

Figure 4.3: Magnetic field components $B_x(x,z)$ and $B_z(x,z)$ produced by stator of configuration 3.

$z-$coordinates in figure 4.4.

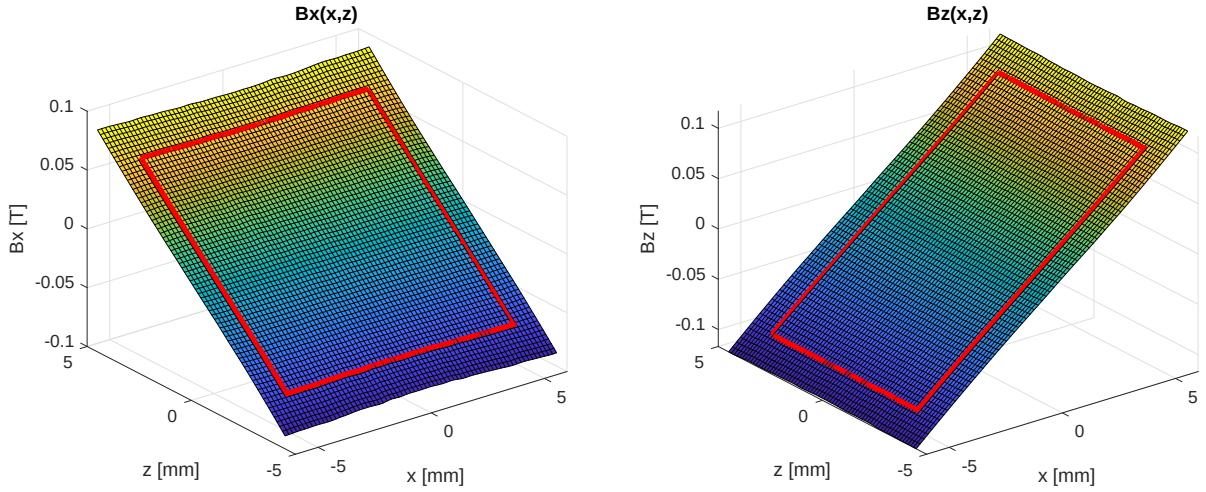

Figure 4.4: Magnetic field components $B_x(x,z)$ and $B_z(x,z)$ produced by stator of configuration 4.

From figure 4.4 it can be seen that the B_x field indeed grows linearly with the $z-$coordinate and that $B_{x,top}$ equals to $-B_{x,bot}$, resulting in a positive force in the $z-$direction. The B_x field in the $x-$direction is constant, meaning that $\frac{dB_x}{dx} = 0$ for the top and bottom, resulting in a low stiffness. In the $z-$direction it has a constant derivative, meaning $\frac{dB_{x,top}}{dz} = \frac{dB_{x,bot}}{dz} = constant$, which also results in a low stiffness. This can be understood as that the force change of the top is equal but opposite to the force change on the bottom surface, resulting in a zero net force change.

The resulting B_z field also grows linearly but in the $x-$direction. Due to the symmetry over the $z-$axis, the B_z field on the top and bottom are equal, resulting in a zero net force in the $x-$ direction, as is desired. The stiffnesses $\frac{dF_x}{dx}$ and $\frac{dF_x}{dz}$ are also both low as the B_z field is constant over the $z-$coordinates, and grows linearly in the $x-$direction.

4.2.3. CONCLUSIONS

- **Configuration 3**: From the analyses of the magnetic field of configuration 3, it is found that the working principle of this configuration is to create a constant magnetic field in the $x-$direction (B_x). This results in an upwards force on the mover. Additionally, the constant field causes low derivatives due to which low stiffness is obtained.
- **Configuration 4**: In configuration 4 the low stiffnesses are the result of a cancellation of the change in

the force on the top and the bottom surface of the mover magnet. This is achieved by creating a linearly growing B_x field.

4.3. DIMENSIONING WITH IDEAL MAGNETS

In the previous section, the working principles were investigated of the magnet configurations 3 and 4. This information will here be used to dimension these configurations to meet the design requirements from table 1.1. This design step is required as these dimensions are yet unknown. Additionally, the stiffnesses that can be obtained with each configuration, are calculated. For this analysis NdFeB magnets of grade N42 of the standard sintered magnets are used from Bakker Magnetics ([26]).

4.3.1. APPROACH

The approach used is based on analyzing the magnetic fields in the $x-$ and $z-$direction (B_x, and B_z) produced by the stator magnets of the configuration under investigation. For this, a 2D FEM simulation of the stator magnets is performed from which the magnetic field components are extracted. Using the knowledge of the working principles, design changes are proposed for changes in the magnet dimensions and gap sizes.

The effect on the performance is subsequently determined by calculating the resulting stiffnesses and the peak-to-peak change of the stiffness. This is accomplished using a hybrid between FEM and the coil model to calculate the forces on the mover magnet as a function of the position. The positions of the mover magnet at which these forces are calculated is defined by a grid in the $x-$ and $z-$direction (short-stroke). In both directions a stroke of 1 $[mm]$ is used (see table 1.1). The forces are calculated with the help of the extracted magnetic field from a FEM simulation. These fields are integrated numerically over the magnet upper and lower surface (as explained in section 4.2) and multiplied with the surface current density $\frac{B_r}{\mu_0}$ to obtain the forces on the mover magnet. This is done for each position to obtain the force-displacement curve.

Important in this 2D approach is to understand that the force, and therefore also the resulting stiffness, are a function of the magnet length, and not only the in-plane magnet dimensions. The way that this is treated is as follows. Firstly the force-displacement curves of the mover magnet are calculated under the assumption that the mover (and stator) are 1 $[m]$ in length. In other words, the force per meter length is determined. From the force in the nominal $x-$ and $z-$position, the required length of the magnets is determined to meet the load capacity requirement. This length is subsequently used as a scaling factor for the force-displacement curves determined. From these re-scaled force-displacement curves the resulting stiffnesses are determined. This process is visualized in figure 4.5.

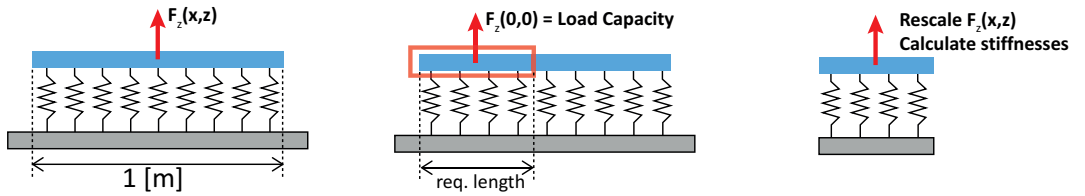

(a) Calculation of the force-displacement curves per meter magnet length.

(b) Determine the required magnet length from the nominal force and the required load capacity.

(c) Rescale the force displacement curces and determine the resulting stiffnesses.

Figure 4.5: Schematic visualization of the design approach and computation steps.

This approach is required due to the fact that there is a strong relationship between the load capacity and the stiffness per meter length of the magnetic design. In other words, this means that if the stiffness per meter length is reduced (by improving the cross-sectional magnet dimensions), the load capacity per meter length also reduces, meaning that a longer magnet is needed to meet the load capacity. This in turn increases the total effective stiffness again of the design. This is schematically shown in figure 4.6.

This coupling between stiffness and load capacity complicates the design process, as improving the design based on the 2D analysis of the magnetic field of the stator could result in a lower stiffness per meter length. However, this unfortunately does not guarantee that the design is actually performing better (as shown in figures 4.6a and 4.6b).

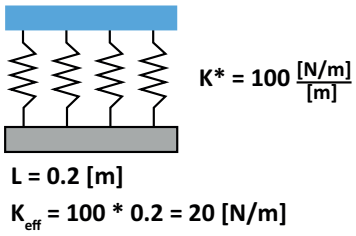

(a) Design A, with a high stiffness per meter length, but a lower effective stiffness.

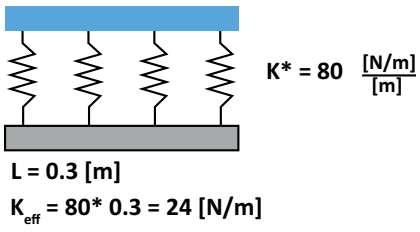

(b) Design B, with a lower stiffness per meter length, requireing a longer magnet, therefore resulting in a higher effective stiffness.

Figure 4.6: Schematic visualization between the coupling of the stiffness and the load capacity, and the resulting effect on the effective stiffness

In the following subsections, the results of the design process are presented for each configuration. Important to know is that for all designs it was found out that three gravity compensators were required to meet the load capacity and the requirements of the maximal allowed cross-sectional dimensions. Due to this, the design requirements presented in table 1.1 are translated to requirements that are valid for one gravity compensator.

Table 4.1: Design Requirements for 1 Gravity Compensator.

Design Specification	Value	Unit
Load Capacity and Force Error		
Load capacity	65.4	$[N]$
Maximum force error in nominal position	0.33	$[N]$
Parasitic Stiffness and Damping		
Parasitic stiffness	333	$[N/m]$
Peak to Peak Change of Stiffness	66	$[N/m]$
Parasitic damping	0.33	$[Ns/m]$
Number and Size Constraints		
Maximum height of the gravity compensator(s)	50	$[mm]$
Maximum width of the gravity compensator(s)	50	$[mm]$

4.3.2. CONFIGURATION 3A

For this configuration the design parameters are the height and width of the stator magnets (h_{stat} and w_{stat}), the horizontal gap size (g) between the stator and the mover magnets, and finally the dimensions of the mover magnet (h_{mvr} and w_{mvr}).

The starting point of the dimensions for the design process are taken from [27] (section 4.3) which result in a maximum stiffness of 50 $[N/m]$ and a peak to peak change of 100 $[N/m]$. As was discussed in subsection 4.2.1, the working principle behind this gravity compensator is to choose the dimensions such that the field around the top and bottom of the mover magnet is as constant as possible. During the design process, it was discovered that this can be achieved by choosing the correct ratio between the stator and mover magnet heights. This results in the magnetic field created by the stator from figure 4.3. The resulting dimensions together with the obtained performance are given in table 4.2, from which can be seen that indeed very low stiffnesses are obtained.

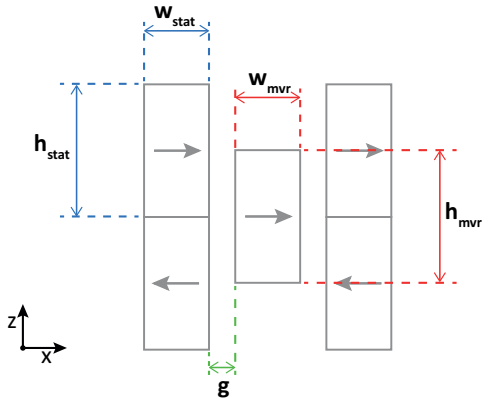

Figure 4.7: Design parameters configuration 3A.

Table 4.2: Dimensions and performance of configuration 3A.

Dimensions				Performance	
h_{stat}	19.00 $[mm]$	w_{stat}	5.00 $[mm]$	load capacity	65.4 $[N]$
g	1.00 $[mm]$			max. stiffness	7.7 $[N/m]$
h_{mvr}	18.00 $[mm]$	w_{mvr}	5.00 $[mm]$	max. change of stiffness	15.2 $[N/m]$
$depth$	15.58 $[mm]$				

4.3.3. CONFIGURATION 3B

Previously it was stated that the working principle of this configuration is to create a constant magnetic field at the top and bottom surface of the the mover magnet. However, if the gap size between the stator magnets is added to the design parameters, a design variation can be obtained.

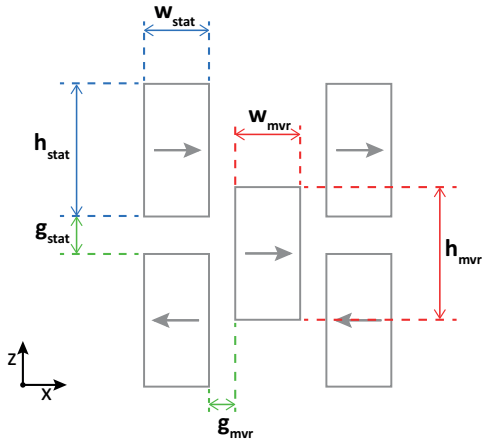

Figure 4.8: Design parameters configuration 3B.

In this case, the field created near the mover magnet actually is linearly growing, similar to configuration 4. This can be achieved by making large air gaps between the stator magnets, both in the vertical and horizontal direction. The mover magnet should be placed in the center where the magnetic fields are linearly growing. The B_x and B_z fields are plotted in 4.4. The design dimensions and the accompanying performance parameters are listened in table 4.3.

4.3.4. CONFIGURATION 4

For configuration 4, the included design parameters are the stator magnet height and width, the horizontal gap size, and the mover magnet dimensions.

Table 4.3: Dimensions and performance of configuration 3B.

Dimensions				Performance	
h_{stat}	14.30 $[mm]$	w_{stat}	7.15 $[mm]$	load capacity	65.4 $[N]$
g_{stat}	19.50 $[mm]$	g_{mvr}	13.00 $[mm]$	max. stiffness	28.8 $[N/m]$
h_{mvr}	10.40 $[mm]$	w_{mvr}	6.50 $[mm]$	max. change of stiffness	57.6 $[N/m]$
$depth$	107.57 $[mm]$				

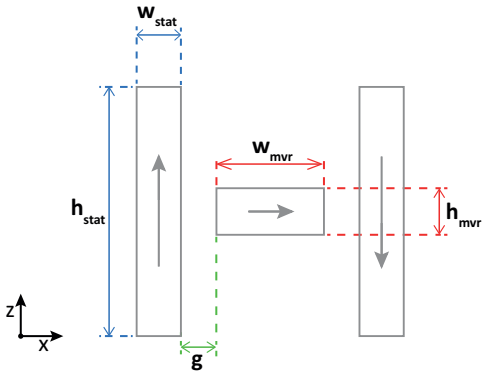

Figure 4.9: Design parameters configuration 4.

From an analysis of the magnetic field, it is concluded that the linearly growing field only happens in the center of the design. Therefore, a relatively small mover magnet should be placed in between two larger stator magnets with a relatively large airgap. The resulting fields are shown in figure 4.4. The dimensions obtained from the design process and the resulting performance parameters are listed in table 4.4.

Table 4.4: Dimensions and performance of configuration 4.

Dimensions				Performance	
h_{stat}	25.00 $[mm]$	w_{stat}	9.00 $[mm]$	load capacity	65.4 $[N]$
g	5.00 $[mm]$			max. stiffness	16.4 $[N/m]$
h_{mvr}	7.00 $[mm]$	w_{mvr}	10.00 $[mm]$	max. change of stiffness	31.3 $[N/m]$
$depth$	42.39 $[mm]$				

4.3.5. CONCLUSIONS

From the results obtained, the following can be concluded: first of all, the 2D dimension method has proven to be a very useful and potent design tool. The coil model approach has provided the necessary insight and understanding for the dimensioning of the magnetic configurations. This process has resulted in 3 potential designs for the long stroke gravity compensator, from which indeed very low stiffnesses were obtained. From the design process, the requirement of the maximum peak to peak change of the stiffness has proven to be the most difficult to meet.

In the next section the effect of the magnet tolerances on the obtained performance is investigated.

4.4. EFFECT OF MAGNET TOLERANCES

In the previous section, the dimensions of the magnets were determined for three different designs using ideal magnets. However, in practice magnets suffer from manufacturing tolerances, like any fabricated part. Therefore, the goal of this section is:

- **Effect of magnet tolerances**: determine the effect of the magnetic tolerances on the performance parameters such as stiffnesses and force errors.

This is valuable information for two reasons: first of all, it will provide information on the expected performance of the gravity compensator. Secondly, it can be used for the design trade-off as a low sensitivity to magnetic tolerances is especially favorable in a long stroke magnetic gravity compensator. This because of

the fact that, due to the large dimension in the long stroke direction, the magnets cannot be manufactured from one single magnet. This entails that the stator will consist of multiple, smaller, magnets, all with their individual tolerances. Having a low sensitivity to these tolerances means that it will be easier to meet the design requirements, therefore making it a more suitable design.

The approach used is, to fix the dimensions of the magnets of the designs obtained in the previous section. Subsequently, the designs are all subjected to the same magnetic tolerances. The resulting stiffnesses, peak to peak change of the stiffness, and the force errors are calculated. Additionally, the effect of the rotation of the mover magnet is investigated. The same modeling approach as used for the dimensioning is applied by incorporating the magnet tolerances as design parameters.

4.4.1. MAGNET TOLERANCES VALUES

The included magnet tolerances are deviations in:

- **Magnetization strength**: The magnetization strength varies from magnet to magnet. In data-sheets generally, a typical value and a minimum value are specified. From the supplier's info of Vacuumschmelze [28], Bakker Magnetics [26], and Goudsmit [29], the variation of the magnetization strength is determined. The maximum value obtained is a deviation of 5 %, which is also stated in [21].

- **Magnetization angle**: The magnetization angle is the deviation of the magnetization with respect to the magnet's geometry (or the ideal magnetization direction). This tolerance is caused by the warping of the magnets during the sintering process, or due to the cutting of smaller magnets from a larger piece of magnetized material (described in [30]). In [21] and [31] angle deviations of 3 $[deg]$ to 5 $[deg]$ are mentioned.

- **Magnet dimensions**: The tolerances on the mechanical dimensions of the magnets are specified differently by each supplier. In [28] the maximal tolerances achievable on the pole surfaces of magnets are specified as ± 0.02 $[mm]$. For the non-pole (side) surfaces tolerances of ± 0.1 $[mm]$ to ± 0.2 $[mm]$ are stated depending on the nominal size of the magnets.

The final tolerance values used for the analysis performed in this study are listen in table 4.5. The mechanical

Table 4.5: Tolerance values used.

Tolerance type	Value used
Variation in magnetization strength	5 %
Variation in magnetization angle	3 $[deg]$
Variation in magnet dimension pole side	0.02 $[mm]$
Variation in magnet dimension non-pole side	0.2 $[mm]$

dimensions are implemented such that the gap sizes from section 4.3 will be maintained. The means that it is assumed that the magnets of the gravity compensator are aligned with a reference surface during the assembly process. The way this is implemented in the model for each configuration is visualized in figures 4.10a, 4.10b, and 4.10c.

4.4.2. RESULTS

The results of the investigation into the effect of the magnetization tolerances for configurations 3A, 3B, and 4 are given in tables 4.6, 4.7, and 4.8 respectively. Besides the tolerances on the magnets, also the effect of the rotation of the mover magnet is included. The used rotation is 0.5 $[mrad]$, as specified in table 1.1.

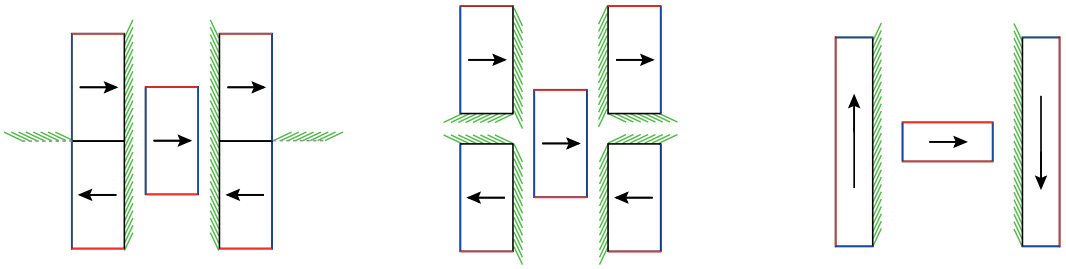

(a) Dimensional tolerances inplemented for configuration 3A.

(b) Dimensional tolerances inplemented for configuration 3B.

(c) Dimensional tolerances inplemented for configuration 4.

Figure 4.10: Schematic visualization of the implementation of the mechanical tolerances for all the configurations (green indicates fixed surfaces, red indicates non-pole surfaces, blue indicates pole surfaces).

Table 4.6: Effects of magnet tolerances on configuration 3A.

Tolerance Type	Max. Stiffness	Max. Var. Stiffness	Max. Force Error
Ideal case	7.7 $[N/m]$	15.7 $[N/m]$	0 $[N]$
Magnet Dimensions			
Case 1: maximum stiffness	102.3 $[N/m]$	16.8 $[N/m]$	0 $[N]$
Case 2: maximum force error	15.5 $[N/m]$	30.1 $[N/m]$	0.2 $[N]$
Magnetization Strength			
Case 1: maximum stiffness	314.4 $[N/m]$	21.6 $[N/m]$	3.3 $[N]$
Case 2: maximum force error	8.5 $[N/m]$	16.7 $[N/m]$	6.7 $[N]$
Magnetization Angle			
Case 1: maximum stiffness	371.8 $[N/m]$	15.6 $[N/m]$	0 $[N]$
Case 2: maximum force error	8.5 $[N/m]$	16.2 $[N/m]$	0.2 $[N]$
Combined			
Maximum stiffness	427.8 $[N/m]$	33.1 $[N/m]$	0 $[N]$
Mover Magnet Rotation	7.4 $[N/m]$	15.6 $[N/m]$	0 $[N]$

Table 4.7: Effects of magnet tolerances on configuration 3B.

Tolerance Type	Max. Stiffness	Max. Var. Stiffness	Max. Force Error
Ideal case	28.8 $[N/m]$	57.6 $[N/m]$	0 $[N]$
Magnet Dimensions			
Case 1: maximum stiffness	77.6 $[N/m]$	36.3 $[N/m]$	1.4 $[N]$
Case 2: maximum force error	30.4 $[N/m]$	60.6 $[N/m]$	1.9 $[N]$
Magnetization Strength			
Case 1: maximum stiffness	386.4 $[N/m]$	60.6 $[N/m]$	3.3 $[N]$
Case 2: maximum force error	31.7 $[N/m]$	63.4 $[N/m]$	6.7 $[N]$
Magnetization Angle			
Case 1: maximum stiffness	371.2 $[N/m]$	60.7 $[N/m]$	0 $[N]$
Case 2: maximum force error	41.2 $[N/m]$	50.8 $[N/m]$	0.3 $[N]$
Combined			
Maximum stiffness	559.0 $[N/m]$	60.2 $[N/m]$	1.2 $[N]$
Mover Magnet Rotation	28.83 $[N/m]$	57.6 $[N/m]$	0 $[N]$

Table 4.8: Effects of magnet tolerances on configuration 4.

Tolerance Type	Max. Stiffness	Max. Var. Stiffness	Max. Force Error
Ideal case	16.4 $[N/m]$	31.3 $[N/m]$	0 $[N]$
Magnet Dimensions			
Case 1: maximum stiffness	104.9 $[N/m]$	32.4 $[N/m]$	0 $[N]$
Case 2: maximum force error	13.6 $[N/m]$	26.1 $[N/m]$	2.9 $[N]$
Magnetization Strength			
Case 1: maximum stiffness	275.7 $[N/m]$	43.0 $[N/m]$	0 $[N]$
Case 2: maximum force error	18.0 $[N/m]$	34.5 $[N/m]$	6.7 $[N]$
Magnetization Angle			
Case 1: maximum stiffness	266.7 $[N/m]$	31.2 $[N/m]$	0 $[N]$
Case 2: maximum force error	5.9 $[N/m]$	54.7 $[N/m]$	0.1 $[N]$
Combined			
Maximum stiffness	287.3 $[N/m]$	33.3 $[N/m]$	1.8 $[N]$
Mover Magnet Rotation	16.3 $[N/m]$	31.2 $[N/m]$	0 $[N]$

4.4.3. DISCUSSION OF RESULTS

In this subsection the most important observations from the results of the effects of the magnetic tolerances are discussed. For this configuration 4 is used as an example, but the conclusions apply to all configurations.

WORST CASE FOR STIFFNESS

It has been observed that high stiffnesses are the result of assymmetries present in the stator magnets. This is the case for the magnet dimensions, however, the effects are much stronger with the magnetization strength and magnetization angle tolerances (see tables 4.6, 4.7, and 4.8). The cases in which these particularly high stiffnesses are observed, are shown in figures 4.11a and 4.11b.

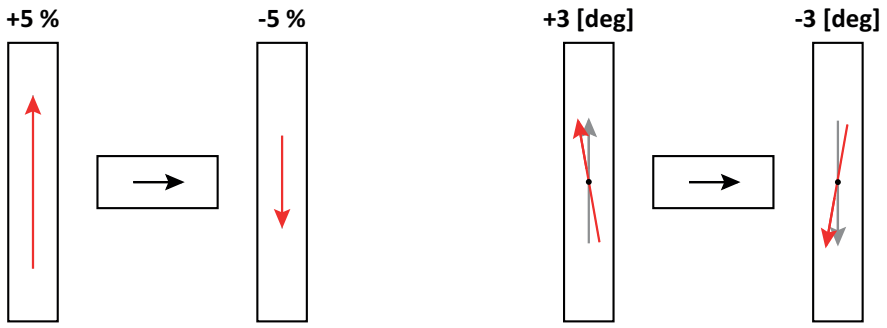

(a) Worst case of the magnetization strength tolerances for the stiffness.

(b) Worst case of the magnetization angle tolerances for the stiffness.

Figure 4.11: Worst cases of the stator tolerance values for the stiffness.

An important fact is that if the tolerances are specified in the opposite case, the sign of the stiffnesses obtained flips. This can be seen in table 4.9. This is very likely to pose a challenge to meet the maximum peak to peak change of the stiffness requirement. This design specification states that the peak to peak change of the stiffness cannot exceed 66 $[N/m]$ per gravity compensator. However, from table 4.9 it can be concluded that (for the tolerance values used in this study) the maximum change of the stiffness could reach values of $275.7 - -275.7 = 515.4$ $[N/m]$ in the case of a long stroke gravity compensator. This is due to the fact that multiple magnets need to be used for the stator in the long stroke direction. This leads to the conclusion that configurations with a low worst-case stiffness are more suitable for a long stroke gravity compensator.

An additional conclusion from table 4.9 is that the cases for which a high stiffness is obtained, actually produce a very low force error. This is relevant information that is elaborated in further detail in chapter 7.

Table 4.9: Effects of magnet tolerances on configuration 4.

Tolerance Type	Left	Right	Max. Stiffness	Max. Force Error
Magnetization Strength	+5 %	−5 %	−275.7 $[N/m]$	0 $[N]$
	−5 %	+5 %	275.7 $[N/m]$	0 $[N]$
Magnetization Angle	+3 $[deg]$	−3 $[deg]$	266.7 $[N/m]$	0 $[N]$
	−3 $[deg]$	+3 $[deg]$	−266.7 $[N/m]$	0 $[N]$

WORST CASE OF FORCE ERROR

In contrast to the worst case stiffness, the worst case force error is actually obtained in a symmetrical case, when the magnetization strength deviation is the same on both stator sides.

The worst case is then reached when all involved magnets are 5 % stronger (or weaker). This actually results in a force error of $\frac{6.7}{65.4} \cdot 100 = 10.3$ %. this can be explained by understanding that the force on the mover magnet scales with the product of the remanences of the stator and mover magnets. In the nominal case this can be written as

$$F_{nom} = F_{stator,left} + F_{stator,right} = CB_1B_3 + CB_2B_3, \tag{4.13}$$

where the remanence of the left stator magnet, the right stator magnet, and the mover magnet are B_1, B_2, B_3 respectively. The maximum force can subsequently be determined as

$$F_{max} = C(B_1 \cdot 1.05)(B_3 \cdot 1.05) + C(B_2 \cdot 1.05)(B_3 \cdot 1.05) \tag{4.14}$$

$$= 1.05^2 CB_1B_3 + 1.05^2 CB_2B_3 = 1.05^2(CB_1B_3 + CB_2B_3) \tag{4.15}$$

$$\approx 1.103 \cdot F_{nom}. \tag{4.16}$$

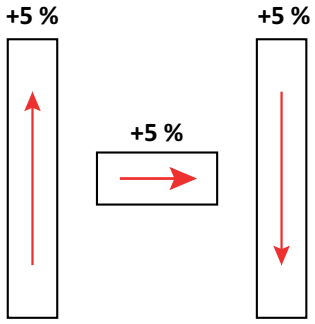

Figure 4.12: Worst cases of the stator tolerance values for the force error.

This explains why the force errors are equal for all configurations. Extending the calculation actually shows that the maximal force error percentage scales linearly with the tolerance for the magnetization strength δ (for small values).

$$\frac{F_{max}-F_{nom}}{F_{nom}}\cdot 100 = \left(\left(\frac{\delta}{100}\right)^2 + 2\frac{\delta}{100}\right)\cdot 100 \approx 2\delta \tag{4.17}$$

EFFECT OF TOLERANCES AND ROTATION OF MOVER MAGNET

From the analysis performed in this section it was observed that the tolerances and the rotation of the mover magnet do not have a strong influence on the stiffness parameters. This can be seen from the data presented in table.

Table 4.10: Effects of mover magnet tolerances and rotation.

Tolerance Type		Max. Stiffness	Max. Var. Stiffness	Max. Force Error
Magnet Dimensions	Max. Dims.	15.5 $[N/m]$	30.6 $[N/m]$	2.0 $[N]$
Magnetization Strength	+5 %	17.2 $[N/m]$	32.8 $[N/m]$	3.27 $[N]$
Magnetization Angle	+3 $[deg]$	16.7 $[N/m]$	32.0 $[N/m]$	0 $[N]$
Rotation	+0.5 $[mrad]$	16.3 $[N/m]$	31.2 $[N/m]$	0 $[N]$

4.5. DEMAGNETIZATION OF DESIGNS

As explained in subsection 2.1.3, demagnetization is very important as it can destroy permanent magnets. This could not only harm the performance of the gravity compensator, but it could event damage the entire machine if overlooked. All designs are therefore checked for demagnetization using the criterion presented in equation 2.6. From the data-sheet, the intrinsic coercivity $H_{c,i}$ is specified as 955 $[kA/m]$ resulting in the criterion to be checked:

$$0.8\cdot H_{c,i} = 0.8\cdot 955\left[\frac{kA}{m}\right] = 764\left[\frac{kA}{m}\right] \geq H_d + H_{ext.}. \tag{4.18}$$

This is accomplished using a FEM simulation with the dimensions obtained from section 4.3. The H field is plotted as a vector field and its magnitude is indicated with the color plot. The scale is chosen such that the maximum value equals 764 $\left[\frac{kA}{m}\right]$ meaning that, in all pink colored areas, the total H field is larger than 764 $\left[\frac{kA}{m}\right]$. If the vector field in those areas also is in the opposite direction of the magnetization, demagnetization will occur there. The results for all topologies are shown in figures 4.13a, 4.13b, and 4.13c.

From these figures, it can be concluded that demagnetization will occur in configuration 3A in the bottom half of the mover magnet. For the other two designs demagnetization does not pose any problems. This

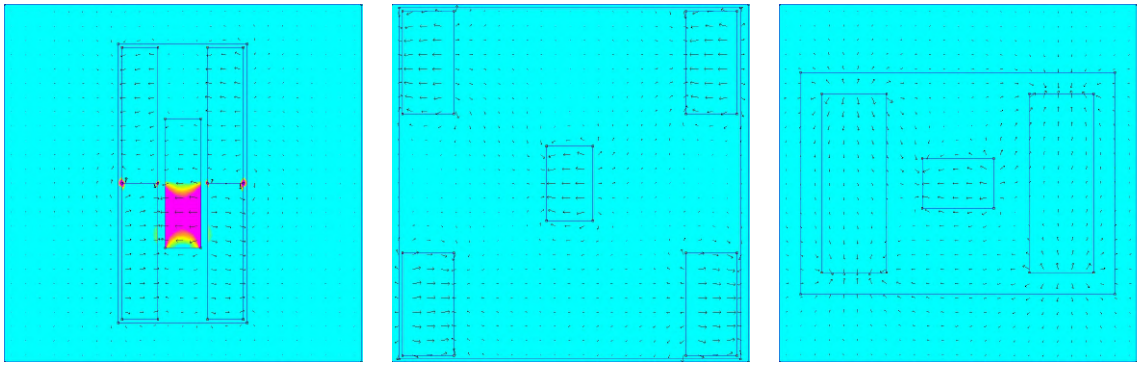

(a) Configuration 3A showing demagnetization of the mover magnet.

(b) Configuration 3B showing no demagnetization.

(c) Configuration 4 showing no demagnetization.

Figure 4.13: Demagnetization check for all designs

is as expected as in configuration 3B the magnets are placed much further apart, and in configuration 4 no magnets are placed with opposing magnetization.

4.6. TRADE-OFF AND DESIGN CHOICE

Using the information generated from the analysis performed in sections 4.3, 4.4, and 4.5 a comparison is made between all the magnetic designs. The configurations are compared on the bases of the performance parameters, demagnetization, and their dimensions. In table 4.11 the trade-off between all the designs can be found.

Table 4.11: Trade-Off table between configurations 3A, 3B, and 4.

Criterion		Configuration 3A	Configuration 3B	Configuration 4
Max. Stiffness	Ideal Magnets	7.7 $[N/m]$	28.8 $[N/m]$	16.4 $[N/m]$
	Non-ideal Magnets	427.8 $[N/m]$	559.0 $[N/m]$	287.3 $[N/m]$
Max. Stiffness Var.	Ideal magnets	15.7 $[N/m]$	57.6 $[N/m]$	31.3 $[N/m]$
	Non-ideal magnets	32.6 $[N/m]$	86.6 $[N/m]$	76.2 $[N/m]$
Dimensions	Cross-section	38×17 $[mm]$	48.1×46.8 $[mm]$	25×38 $[mm]$
	Mover length	15.58 $[mm]$	107.57 $[mm]$	42.39 $[mm]$
Force Density	Force per Total Volume	0.47 $[N/cm^3]$	0.09 $[N/cm^3]$	0.28 $[N/cm^3]$
Demagnetization		yes	no	no

From the trade-off table the following can be concluded:

- **Lowest Stiffness**: configuration 4 has the lowest worst-case stiffness thereby making it actually the only design that meets the requirement of a maximum absolute stiffness of 333 $\left[\frac{N}{m}\right]$. Having a low stiffness is also advantageous for the peak to peak change of the stiffness requirement. As explained in 4.4.3 the worst-case stiffness could appear both as positive and negative case, resulting in large variations of the stiffness. Therefore, having a low worst-case stiffness is especially advantageous for the long stroke gravity compensator.
- **Dimensions and force density configuration 3B**: In contrast to configuration 4, configuration 3B actually has the highest stiffness and the highest in-plane variations of the stiffness. Additionally, the mover magnet is very long and the force density is very low. Having a long mover magnet is especially inconvenient for a long stroke gravity compensator, as this also increases the required stator length. These

points combined make configuration 3B not a suitable design for a long stroke gravity compensator.

- **Demagnetization of 3A**: Besides the fact that configuration 3B has a higher stiffness than configuration 4, it also has the problem of demagnetization. This means that either the design must be changed (resulting in higher stiffnesses), or that the mover magnet has to be made of expensive, high coercivity magnets.

From the arguments above it has been decided that configuration 4 is the best design for a long stroke magnetic gravity compensator. In the following subsections, the final dimensions will be determined, and the damping will be estimated.

4.7. FINAL MAGNET DIMENSIONS

From the comparison between the models presented in section 2.3 it was concluded that it is best practice to check the results of a 2D analysis using a 3D modeling method. The final dimensions of the design will therefore be determined using the surface charge model. The goals of this analysis are:

- **Stator margin**: determine the needed length margin of the stator magnets in the long stroke direction. This cannot be determined using a 2D modeling technique.
- **Length of mover magnet**: The final length of the mover magnet will be determined. This can be done after the stator length margin has been determined.

Both these are discussed in the following subsections. For this analysis nominal magnet parameters are used (i.e. the magnet tolerances are not included in the model).

4.7.1. STATOR LENGTH MARGIN

The stator length margin is required to limit the stiffnesses at the end of the long-stroke where the field of the stator weakens. The total length of the stator magnets is determined by the summation of the required stroke, the length of the mover magnet, and the required margin.

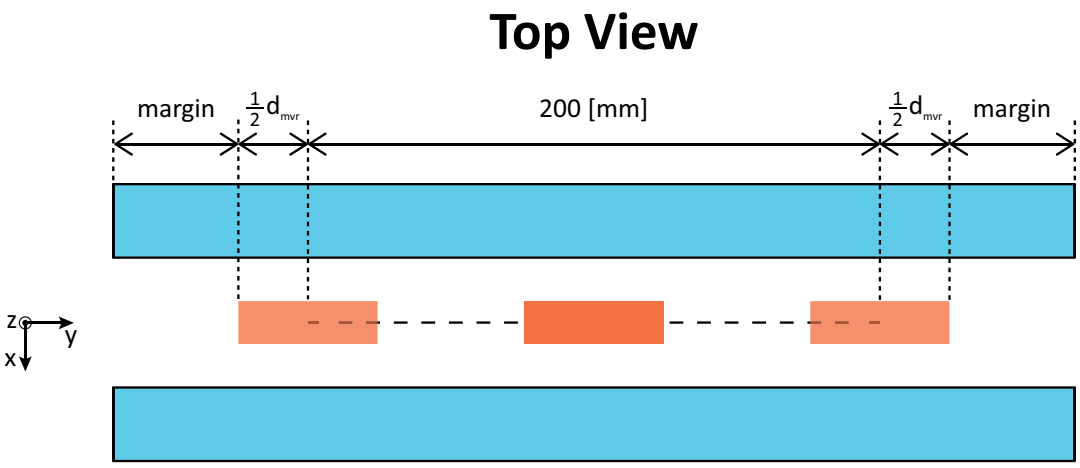

Figure 4.14: Schematic visualization of the required stator length.

The approach to find this margin is to incrementally increase the stator length until the resulting stiffness is low enough. The criterion used in this analysis is that the additional change of the stiffness should remain under 10 $[N/m]$. From subsections 4.3.4 and 4.4.2, the expected peak to peak change of the stiffness in the short stroke directions is approximately 30 $[N/m]$. The additional 10 $[N/m]$ due to the end of the stroke field weakening is chosen to leave a margin of $66-30-10 \approx 26$ $[N/m]$ for additional undetermined or unforeseen (3D) effects.

The reason why the change of the stiffness is chosen as a criterion is that the end of stroke effects always cause a positive and a negative stiffness. In figure 4.16 the force on the mover magnet is plotted in the nominal $x-$ and $z-$ coordinate over the entire long-stroke ($y-$) direction. From this figure it can be seen that the force

decreases slightly on both sides. This results in a positive stiffness on the left, and a negative stiffness on the right (see figure 4.15).

The stator length is varied between 330 $[mm]$ and 350 $[mm]$ with 5 $[mm]$ increments. The results are given in figure 4.15 and table 4.12. The margins are determined using the mover magnet length of 42.39 $[mm]$ resulting from the 2D analysis.

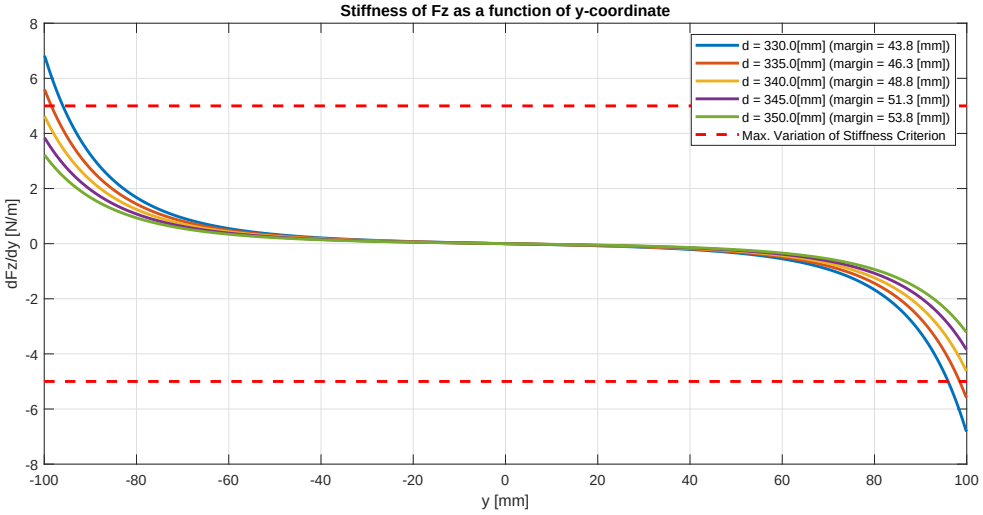

Figure 4.15: Resulting end of stroke stiffness for various stator lengths.

Table 4.12: Stiffness results for different stator length margins.

Stator Length	Resulting Margin	Changes of Stiffness
330 $[mm]$	43.8 $[mm]$	13.6 $[N/m]$
335 $[mm]$	46.3 $[mm]$	11.2 $[N/m]$
340 $[mm]$	48.8 $[mm]$	9.2 $[N/m]$
345 $[mm]$	51.3 $[mm]$	7.6 $[N/m]$
350 $[mm]$	53.8 $[mm]$	6.4 $[N/m]$

From these results it was chosen the use a length margin of 48.8 $[mm]$, which was rounded up to 50 $[mm]$.

4.7.2. FINAL LENGTH OF MOVER MAGNET

Using the found stator length, the force on the mover magnet was calculated over the entire long stroke direction in the nominal $x-$ and $z-$position. From this, the average force on the mover magnet was determined. Subsequently the mover magnet length was scaled such that the average force equals the required load capacity.

This resulted in a mover magnet length of 42.13 $[mm]$

4.8. DAMPING ESTIMATION

In the previous sections the focus was mainly on the stiffness and the force error requirements. However, also a maximum damping constant was specified in the design requirements (see table 1.1). Damping in a long stroke gravity compensator is caused by eddy currents in the stator, created by the changing magnetic field caused by the translating mover magnet (see figure 4.17).

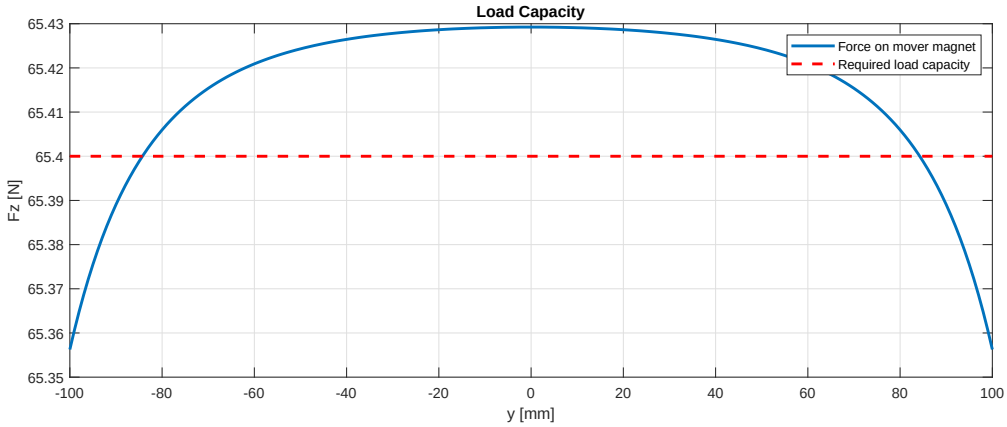

Figure 4.16: Force on the mover magnet over the long-stroke direction (in the nominal $x-$ and $z-$position).

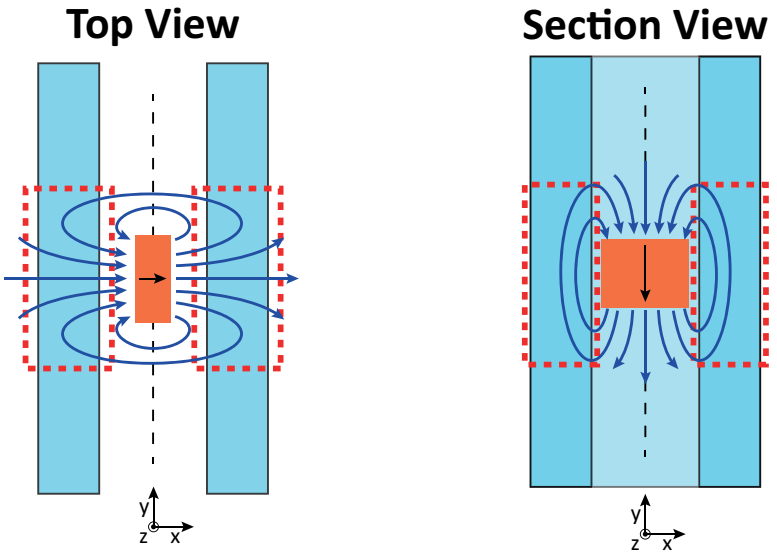

(a) Schematic visualization of the stator (indicated in blue) regions where eddy currents are generated.

(b) Schematic visualization of the regions where eddy currents are generated by a magnet falling through a conducting tube (indicated in blue).

Figure 4.17: Comparison between eddy currents in a magnetic gravity compensator and eddy currents in conducting tube due to a falling magnet.

In [32] a falling magnet in a conducting tube is investigated. A method for calculating the damping force is used to calculate the terminal velocity and the time it takes for the magnet to fall through a tube of a particular length. These calculations are then validated experimentally. The situation for a long stroke gravity compensator is very similar to the one of the falling magnet inside a conducting tube, therefore the model presented in [32] is used to estimate the expected damping of the long-stroke gravity compensator.

For this, the stator magnets were translated to a tube with the same frontal area where the middle of the tube was placed at the center of the stator magnets. The same was done for the mover magnet, where the length of the magnet was directly taken from the results of subsection 4.7.2. The velocity of the mover magnet was specified as $v = 250$ $[mm/s]$ (see table 1.1) and the conductivity of the NdFeB magnets as $\rho = 144$ $[\Omega m]$ (from [26]). The resulting forces and damping constants are listed in table 4.13. As the maximum allowable damping constant is 1 $[Ns/m]$ and the resulting estimation for the total damping is $1.7 \cdot 10^{-4}$ $[Ns/m]$, it is concluded that the damping due to eddy current damping in the stator magnets will not be an issue.

Table 4.13: Results of damping estimation.

Tolerance type	Value used
Force on one gravity compensator	$1.4 \cdot 10^{-5}$ $[N]$
Damping constant one gravity compensator	$5.5 \cdot 10^{-5}$ $[Ns/m]$
Force on three gravity compensators	$4.2 \cdot 10^{-5}$ $[N]$
Damping constant three gravity compensators	$1.7 \cdot 10^{-4}$ $[Ns/m]$

4.9. CONCLUSIONS

In this chapter, the magnetic design of the gravity compensator has been discussed in detail. The goals stated at the beginning of this chapter were to find dimensions for the magnetic configurations to meet the requirements, to evaluate the effect of the magnet tolerances, and to estimate the damping. From this process, the following can be concluded:

- **Dimensioning the magnetic configurations**: using the design principles derived in section 4.2, the required magnetic design were dimensioned to meet the required specifications from table 1.1. In this process a two-dimensional approach was used, combining FEM and the coil model, which has proven to be a very powerful design tool. In the case of ideal magnets, stiffnesses as low as ~ 23 $[N/m]$ were observed for the whole gravity compensator system.
- **Effect of magnet tolerances**: The effect of magnet tolerances on the performances was investigated, where it was observed that for all configurations the stiffness can increase significantly due to asymmetries in the stator magnets. Stiffness increases of roughly a factor of 20 (compared to the ideal case) should be expected. The force error suffers mostly from symmetrical variations in the magnetization strength, where the percentage error scales linearly with the specified tolerance by a factor of 2.
- **Chosen design**: Configuration 4 was chosen as the most suitable design for a long stroke gravity compensator as it showed the lowest sensitivity of the stiffness to the magnet tolerances. Stiffness in the order of ~ 850 $[N/m]$ should be expected for the whole gravity compensator system, when magnetic tolerances of ± 5 % strength variations and ± 3 $[deg]$ variation in the magnetization angle are present.
- **Damping estimation**: For the chosen configuration, the damping constant was estimated at $1.7 \cdot 10^{-4}$ $[Ns/m]$. With the requirement at 1 $[Ns/m]$ it is concluded that eddy current damping in the magnetic material of the stator will not cause any performance issues.

5

DESIGN OF EXPERIMENTAL SETUP

5.1. GOAL OF THE EXPERIMENTAL SETUP AND APPROACH

So far the focus of this study has been on calculating the expected performance using various modeling methods. However, to answer the question of whether a long stroke magnetic gravity compensator is suitable for a nanometer precision positioning application, also practical validation is required. For that purpose, an experimental setup is realized. The goals of this setup are:

- **Validate the concept and design**: the first goal is to validate the concept and design of the long-stroke magnetic gravity compensator from a practical perspective. This is mainly targeted towards the influence of magnet transition in the long stroke direction since the effects of these transitions have not yet been studied in the literature. The inherent modeling simplifications such as neglecting the rounded magnet edges might cause performance issues if local fluctuations in the magnetic field are created.
- **Validate the model**: By comparing the results from the model to the measurements, the validity of the model can be assessed. This will answer the question if the used modeling methods are reliable design tools.
- **Determine the performance**: The measurements can finally be used to determine the performance of the long-stroke gravity compensator. This will serve again as a validation of both the design and the model.

The chosen approach for practical validation is to measure the magnetic field of the stator. In subsection 4.4.3 it was concluded that the stator has the most influence on the performance of the gravity compensator, thereby making it a suitable parameter for the experimental validation.

The advantage of measuring the magnetic field over measuring the force directly is that no measurement noise is present due to friction and/or cross-talk between the different forces and moments. The downside of measuring the magnetic field is that a method is needed to translate the field measurements to performance parameters. This can be done using the coil model, as was done in the design process (see chapter 4).

It was chosen to limit the measurement to the $x-$component of the magnetic field (B_x). As explained in section 4.2, the B_x component translates directly to the force in the $z-$direction. Therefore making it possible to validate the force error, and the stiffnesses of the F_z force in the $x-$, $y-$, and $z-$directions.

The goal for the design of the experimental setup is therefore to measure the $x-$component of the magnetic field as a function of the $x-$, $y-$, and $z-$coordinates. To achieve this the following process steps are determined.

- **Choose sensors**: both the position in $x-$, $y-$, and $z-$, and the magnetic field need to be measured. For this, the measurement requirements need to be determined, and sensors need to be chosen.
- **Design and realize the setup**: the experimental setup has to be designed and manufactured.

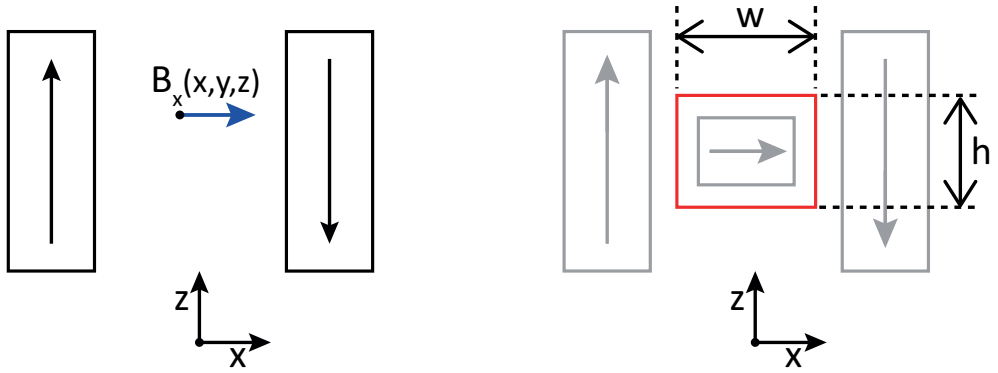

(a) Schematic of the B_x component in the airgap of the sator.

(b) Schematic of the measurement region between the two stator sides (w is the width of the mover magnet plus the stroke, h is the height of the mover magnet plus the stroke).

Figure 5.1: Schematic of the measurement approach and region.

- **Measurement of magnetic tolerances**: To be able to validate the model, the tolerances of the magnets needs to be known. Therefore, these will need to be measured. Next to the model validation, this will also provide information on the performance obtained with these specific magnetic tolerances.
- **Determine the measurement procedure**: To perform the measurements, a measurement procedure is required. This is mainly to determine the reference location of the measurement position.

These points will all be discussed in the following sections.

5.2. SENSOR REQUIREMENTS AND CHOICE

The first step towards the realization of the experimental setup is to determine the sensor requirements such as measurement range and resolution. This will be discussed for the position and magnetic field sensor in the following two subsections. In 5.2.3 the chosen measurement devices are discussed.

5.2.1. REQUIREMENTS FOR POSITION SENSOR

The measurement of the magnetic field will be done around the mover magnet coordinates where also the added distance of the strokes is taken into account. The resulting required movement ranges can be seen in 5.1b. The measurements will be conducted in a grid of 12×12 points. The step size in the $x-$ and $z-$direction will therefore be 1 $[mm]$ and 0.73 $[mm]$ respectively. The required resolution will be taken as $\frac{1}{10}$ times the smallest step size. The overview of all the requirements is given in table 5.1.

Table 5.1: Position sensor requirements.

Requirement	Value
Range $x-$direction	11 $[mm]$
Range $z-$direction	8 $[mm]$
Step size $x-$direction	1 $[mm]$
Step size $z-$direction	0.73 $[mm]$
Resolution	0.073 $[mm]$

5.2.2. REQUIREMENTS FOR MAGNETIC FIELD SENSOR

The position range from the previous section is used to determine the measurement range of the magnetic field. The expected field can be seen in figure 5.2.

The measurement range is thus from -90 $[mT]$ to $+90$ $[mT]$. The expect field change per measurement step is thus $\frac{180}{11} \approx 16.4$ $[mT]$. Similar to the resolution for the position measurement, the resolution for the magnetic

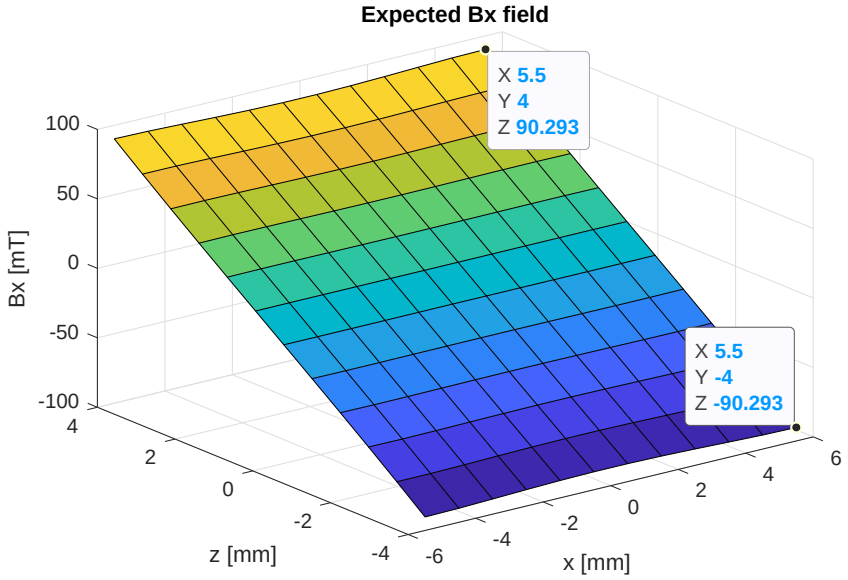

Figure 5.2: Expected magnetic field $B_x(x,z)$ created by the stator.

field sensor has been determined as $\frac{1}{10}$ of the expected step resulting in a resolution of $\approx 1.6\ [mT]$. The resulting requirements are summarized in table

Table 5.2: Magnetic field sensor requirements.

Requirement	**Value**
Range	$\pm 90\ [mT]$
Expected step	$16.4\ [mT]$
Step size $x-$direction	$1\ [mm]$
Resolution	$1.6\ [mT]$

5.2.3. CHOSEN MEASUREMENT DEVICES

For the position measurement and movement, linear stages from Thorlabs have been selected (see figure 5.3a). They have a movement range of 25 $[mm]$, and a resolution of 0.01 $[mm]$, which is well below the required 0.073 $[mm]$. The TU Delft has many of these stages available therefore creating the possibility to make an $xyz-$stage by stacking them.

For the measurement of the magnetic field, the Hirst GM07 is selected (figure 5.3b). It has four measurement ranges (see appendix A) from which ranges 2, 3, and 4 can be used, where the maximum resolution is 0.1 $[mT]$ in range 2. Other advantages of the measurement device are that it has a long probe that can easily be inserted into the air gap, and that the sensor at the tip of the probe is clearly visible. This makes positing an easy process. Finally, the device is also calibrated by the manufacturer.

The reproducibility of the magnetic field sensor was also tested in the relevant field range by performing consecutive measurements of the magnetic field of a magnet. A simple test jig was developed to place and keep the magnetic field sensor at the correct distance from a permanent magnet. The measurements were spaced out over an entire day. The simple measurement setup was placed inside this room the night before to minimize the effect of temperature changes. The results of the measurements can be seen in table 5.3. From these results it was concluded that the 3σ repeatability interval is $\approx \pm 0.04\ [mT]$.

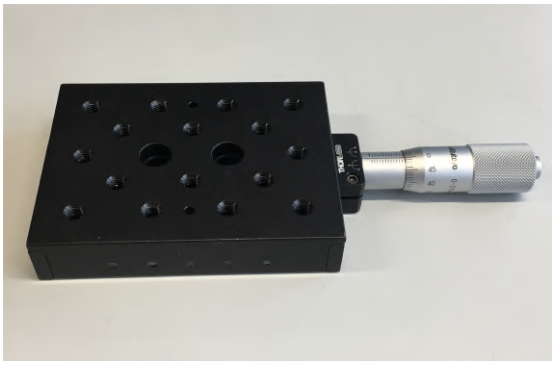

(a) Thorlabs manual linear stage.

(b) Hirst GM07 magnetic field sensor (Hall sensor principle).

Figure 5.3: Chosen sensor devices for the experimental setup.

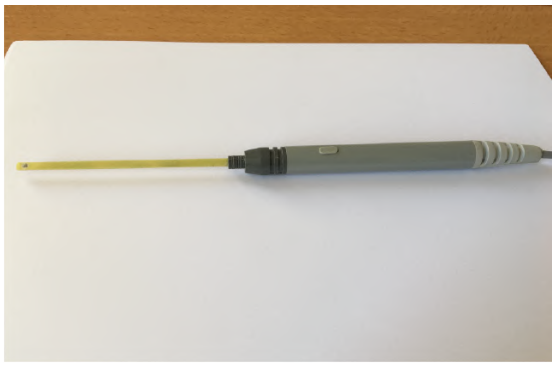

(a) The sensor probe of the GM07.

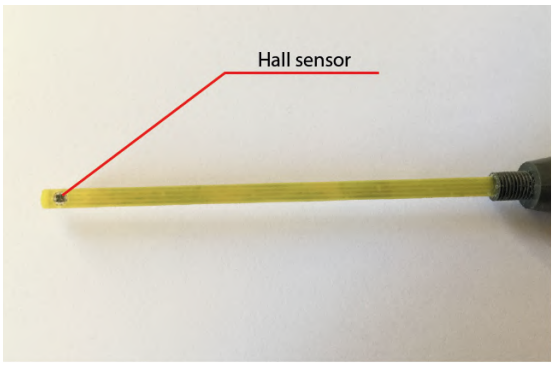

(b) Close up of the sensor probe with the Hall sensor located in the tip of the probe.

Figure 5.4: Sensor probe.

Table 5.3: Magnetic field sensor reproducibility measurement results.

Measurement Number	Time of Measurement	Measured Value
1	9 : 17	81.4 $[mT]$
2	10 : 21	81.3 $[mT]$
3	11 : 21	81.3 $[mT]$
4	12 : 20	81.3 $[mT]$
5	13 : 19	81.3 $[mT]$
6	14 : 39	81.3 $[mT]$
7	15.23	81.3 $[mT]$

5.3. DESIGN OF EXPERIMENTAL SETUP

In this section the final design of the experimental setup is presented. As the magnetic design is made with non-standard magnet dimensions, the closes match magnets needed to be found. These are QM-40x10x05-N from `https://www.magnet-shop.com` (see appendix B for the data-sheet). In total 90 magnets were ordered to make two stator arrays with the outer dimensions of $w \times d \times h = 10 \times 360 \times 25$ $[mm]$ by stacking 5 magnets on top of each other. For comparison: the original design of the stator magnets had the outer dimensions of $w \times d \times h = 9 \times 340 \times 25$ $[mm]$. The magnet properties as stated by the supplier are given in table 5.4. The final design can be seen in figure 5.5. A few parts of the design will be discussed in a bit more detail in subsections 5.3.1, 5.3.2, and 5.3.3.

Table 5.4: Properties of the magnets used in the experimental setup.

Magnetic Properties				**Dimensions**	
Magnetic grade	$N42$			Width	10 $[mm]$
B_r (range)	$1.29 - 1.32$ $[T]$	B_r (mean)	1.31 $[T]$	Depth	40 $[mm]$
$H_{c,B}$ (range)	$860 - 955$ $\left[\frac{kA}{m}\right]$	$H_{c,B}$ (mean)	908 $\left[\frac{kA}{m}\right]$	Height	5 $[mm]$
$H_{c,i}$	≥ 955 $\left[\frac{kA}{m}\right]$				
BH_{max} (range)	$318 - 334$ $\left[\frac{kJ}{m^3}\right]$	BH_{max} (mean)	326 $\left[\frac{kJ}{m^3}\right]$	Tolerance	± 0.1 $[mm]$

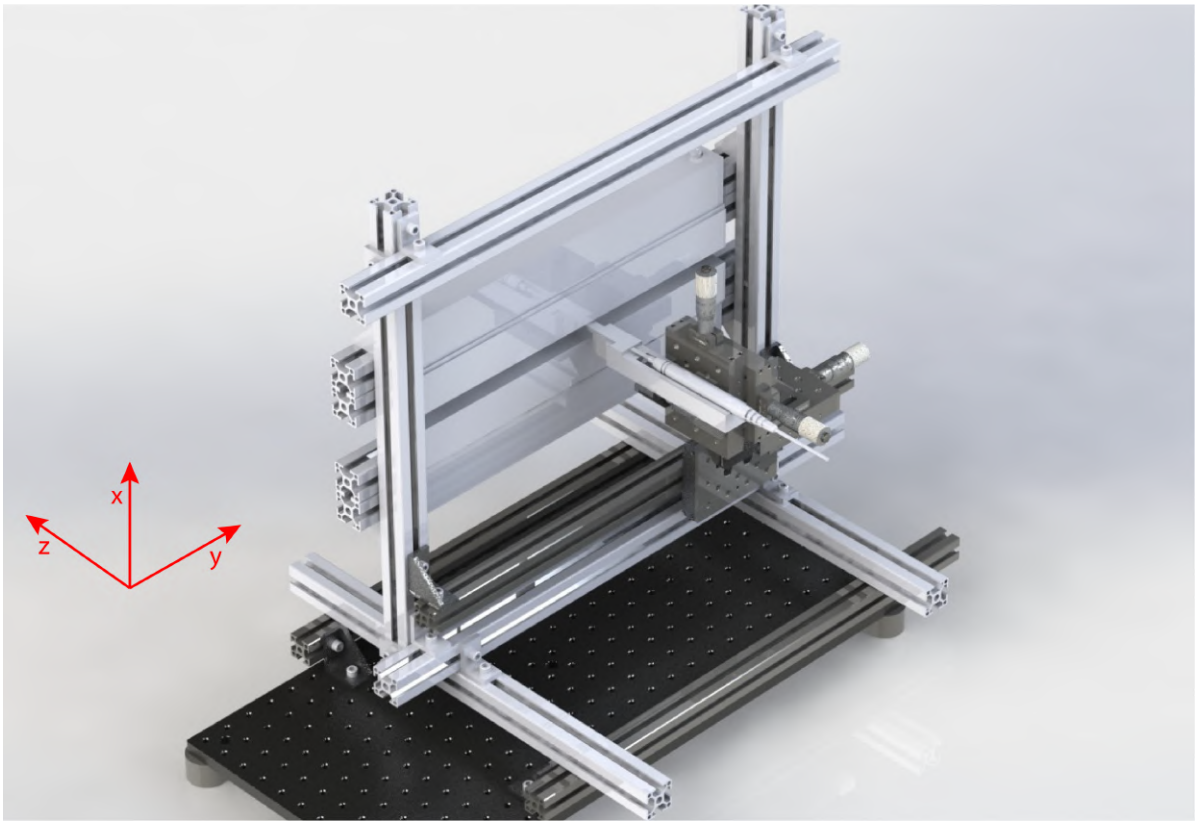

Figure 5.5: Render of the final design of the experimental setup.

5.3.1. MAGNET STATOR ASSEMBLY

As explained in subsection 4.4.1, the stator magnets aligned on the bottom and on the inside. This is achieved by means of an aluminium angle profile. The magnets are first glued in vertical stacks of five magnets, which are subsequently glued to the angle profile and to each other. The resulting array is depicted in 5.6a.

Using the model it is calculated that the attracting force between the two stator magnet arrays is approximately 220 $[N]$. Therefore, a structural element in the form of an aluminium box section is added (see figure 5.6b). The box section is attached to two aluminium extrusion profiles via T-screws in four locations, which allow for slight adjustability of the magnet arrays. This is needed to align the two stator sides. The aluminium extrusion profiles are attached to the main frame via corner brackets.

5.3.2. PROBE HOLDER

The probe of the GM07 was accurately modeled using SOLIDWORKS, to make a holder to attach it to the experimental setup. The most important features in the design of this probe holder are two referencing surfaces that have been added to ease the process of referencing. They are dimensioned such that when used in the referencing procedure, the sensor in the tip of the probe is in the position $(x, z) = (-5.5, 4)$ $[mm]$ (explained in more detail in section 5.6).

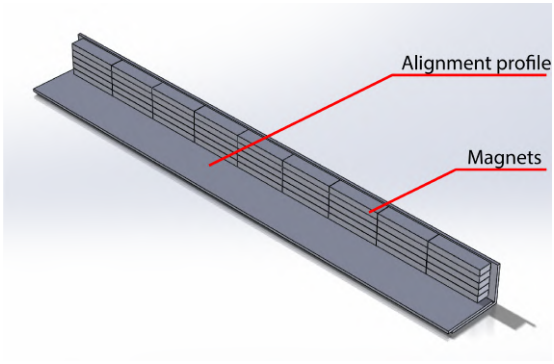

(a) Render of the magnets and the aluminium angle profile used for the alignment of the magnets.

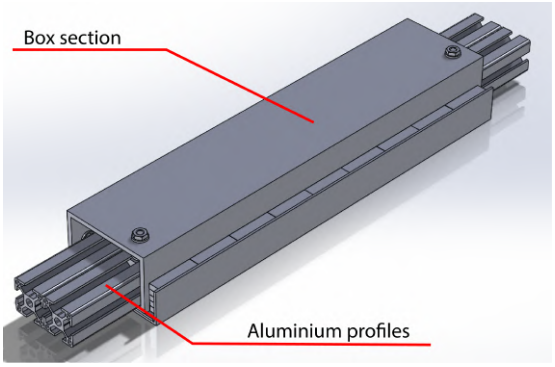

(b) Left stator assembly with the magnets attachted to the aluminium box section.

Figure 5.6: Renders of the stator design.

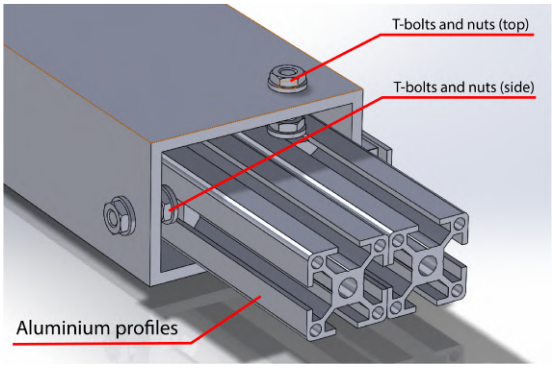

(a) Close up of the end of the left stator assembly where the adjustment bolts are located.

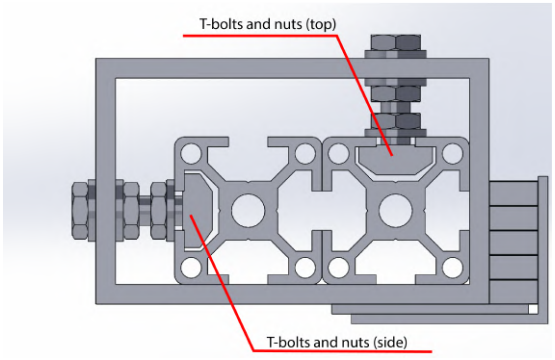

(b) Side view of the left stator assembly showing the T-bolts for the adjustibility in two directions.

Figure 5.7: Close ups of the adjustability mechanism of the stator assembly.

5.3.3. STAGE ASSEMBLY

As mentioned in section 5.2, Thorlabs linear stages were selected for the positioning of the sensor probe. In total, four of these manual stages were used in the design of the experimental setup. The top two provide the movements in the $x-$ and $z-$ directions. The bottom two are placed both in the $y-$ (long-stroke) direction. The reason why there are two is explained in section 5.6. The entire stage assembly is attached to a measurement frame consisting of a Thorlabs aluminium profile. This allows for the stage assembly to be placed anywhere besides the stator arrays.

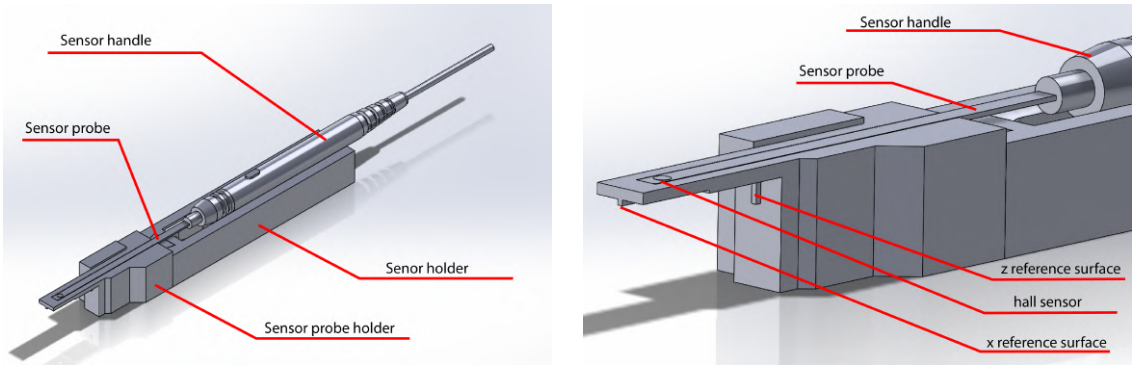

(a) Render of the sensor probe holding clamp.

(b) Close up of the tip of the sensor probe holding clamp showing the referening surfaces.

Figure 5.8: Renders of the parts holding the sensor clamp in place.

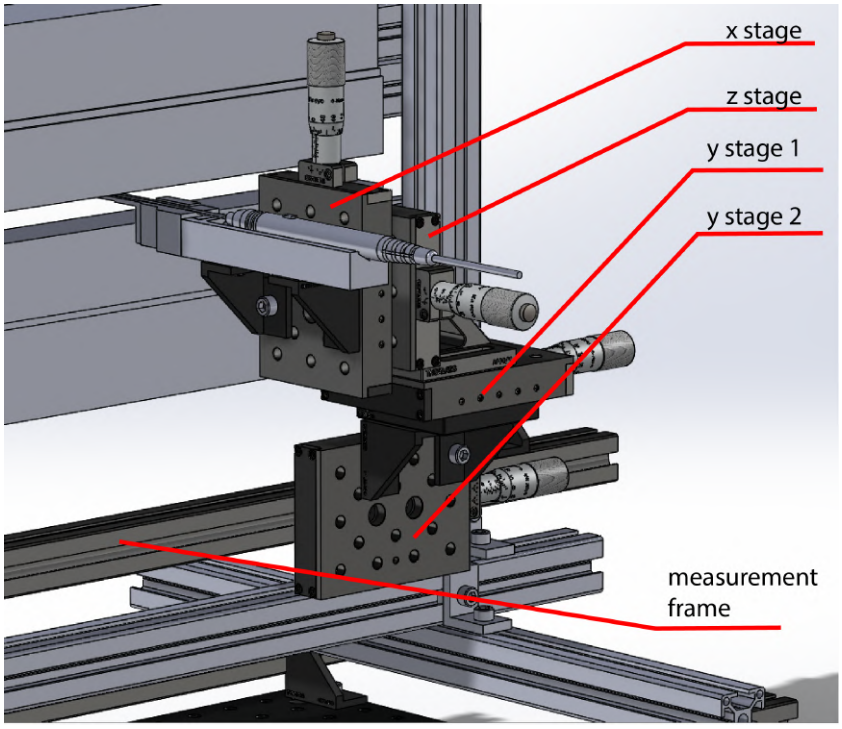

Figure 5.9: Render of the manual stage assembly used to move the sensor probe through the airgap.

5.4. MEASUREMENTS OF MAGNET TOLERANCES

As stated at the beginning of this chapter, the purpose of measuring all the magnetic tolerances provides the information to calculate the expected variations in the magnetic field. This will be very important to determine the 3σ uncertainty interval, which is needed for the model validation. Additionally, the magnetic tolerances can also be linked with the performance calculated from the measurement data which eventually can be used to determine what tolerances are acceptable in the final application.

There are several options for measuring the magnetic properties, which are all discussed in [33] and [34]. The three main options are the torsional pendulum, the magnetic field at a distance, and the Helmholtz method. However, for determining the magnetization strength and magnetization angle, the latter preferred as is also described in [35]. Therefore this method has been used to measure all magnetic properties of all the individual magnets.

5.4.1. MAGNET DIMENSIONS

This measurement is carried out using a standard caliper, where all dimensions were measured. The accuracy and reproducibility of the caliper were first determined by measuring a series of metric gauge blocks ranging from 1 to 50 $[mm]$. It was determined that both the accuracy and the reproducibility of the caliper were smaller than 0.01 $[mm]$. The results of the measurements of all the magnet dimensions are displayed in figure 5.10.

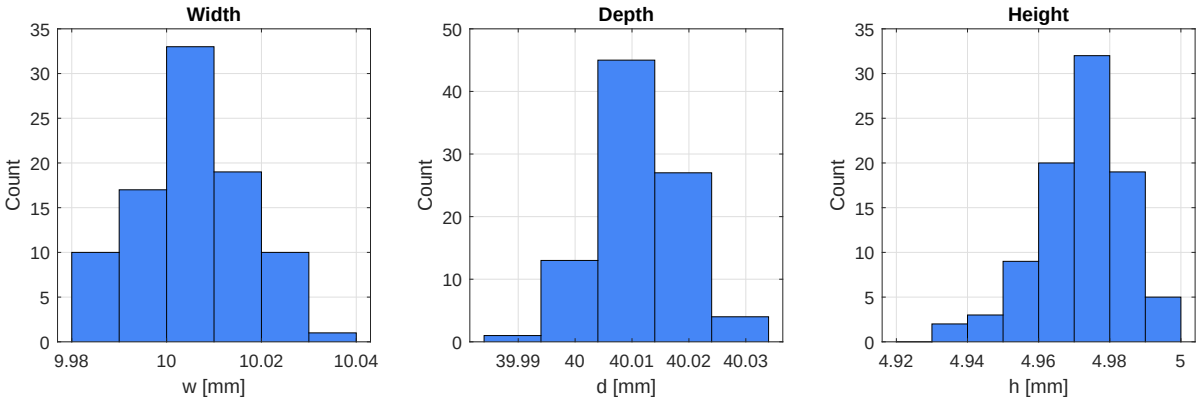

Figure 5.10: Measured magnet tolerances: dimensions.

Table 5.5: Measurement results of the dimensions.

Dimension	Mean	Std	Min.	Max.	Range
Width	10.00 $[mm]$	0.01 $[mm]$	9.98 $[mm]$	10.03 $[mm]$	0.05 $[mm]$
Depth	40.01 $[mm]$	0.01 $[mm]$	39.99 $[mm]$	40.03 $[mm]$	0.04 $[mm]$
Height	4.97 $[mm]$	0.01 $[mm]$	4.93 $[mm]$	4.99 $[mm]$	0.06 $[mm]$

5.4.2. MAGNETIZATION STRENGTH

As mentioned, all magnets were measured using a Helmholtz coils set. The measurements were performed by Bakker Magnetics in Eindhoven with an accuracy of 0.5 %. From these measurements the magnetic dipole moment can be determined. As described in subsection 2.2.1, the magnetization strength B_r can be determined if the dipole moment and the dimensions of the magnet are known (equation 2.9). However, the results are better if a correction factor is introduced that depends on the magnet dimensions as is described in [35]. This correction factor is referred to as the demagnetization factor, and they have been calculated using equations (1) and (2) as presented in [36] (for more info see also [37]) using the measurements of the dimensions. Finally the B_r values were calculated using

$$m = \frac{B_r}{1+(\mu_r-1)N_m} \cdot \frac{V}{\mu_0} \tag{5.1}$$

from [31], where V is the total volume of the magnet and N_m is the demagnetization factor in the principle magnetization direction. The results are visualized in figure 5.11. The statistical parameters are also listed in 5.6.

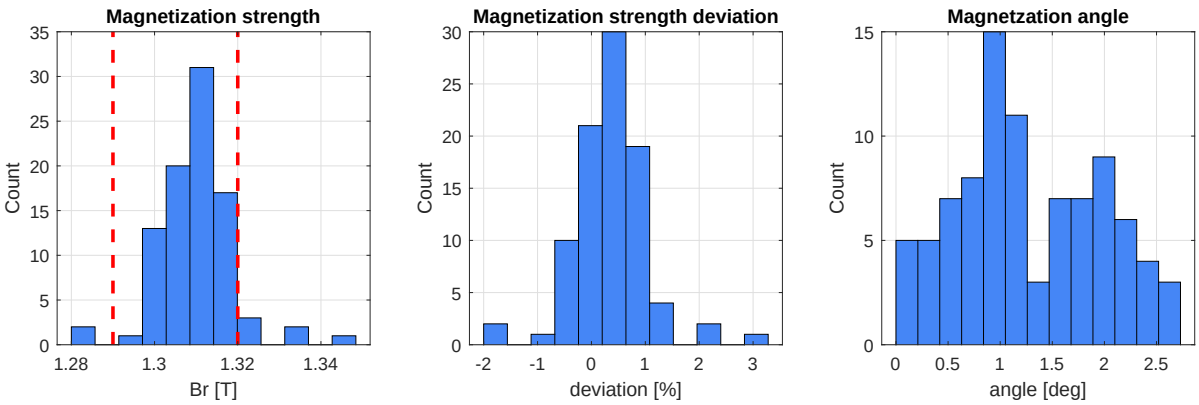

Figure 5.11: Measured magnet tolerances: strength and angle.

5.4.3. MAGNETIZATION ANGLE

With the 3D Helmholtz coil measurements also the magnetization angle of the magnets are measured. The tolerances on this parameter are not specified by the supplier. The resulting histogram of the magnetization angle can be seen in figure 5.11.

Table 5.6: Measurement results of the magnetization strength and angle.

Parameter		Mean	Std	Min.	Max.	Range
Magnetization strength	Absolute	1.31 $[T]$	0.01 $[T]$	1.28 $[T]$	1.34 $[T]$	0.06 $[mm]$
	Percentage	-	-	2.13 %	2.88 %	5 %
Magnetization angle		1.27 $[deg]$	0.68 $[deg]$	0.1 $[deg]$	2.7 $[deg]$	2.6 $[deg]$

5.4.4. CONCLUSIONS

From the measurements of the magnets the following points can be concluded:

- **Dimensions**: the dimensional tolerances are better than specified by the supplier. Also, the tolerances seem to be equal for all the dimensions, unlike what was used in the calculations in 4.4.

- **Magnetization strength**: the mean magnetization strength is indeed equal to the nominal magnetization strength specified by the supplier. However, the minimal and maximal values found for the magnetization strength are outside of the specified range. It is therefore advised to order extra magnets in the future. Also, the tolerances value of 5 % which was used in section 4.4 is higher than the range measured here.

- **Magnetization angle**: the magnetization angle variations measured were maximally 2.7 $[deg]$, meaning that the used 3 $[deg]$ in section 4.4 was a reasonable value.

5.5. REALIZATION OF EXPERIMENTAL SETUP

The experimental setup was realized as presented in the design. The final results is shown in figures 5.12.

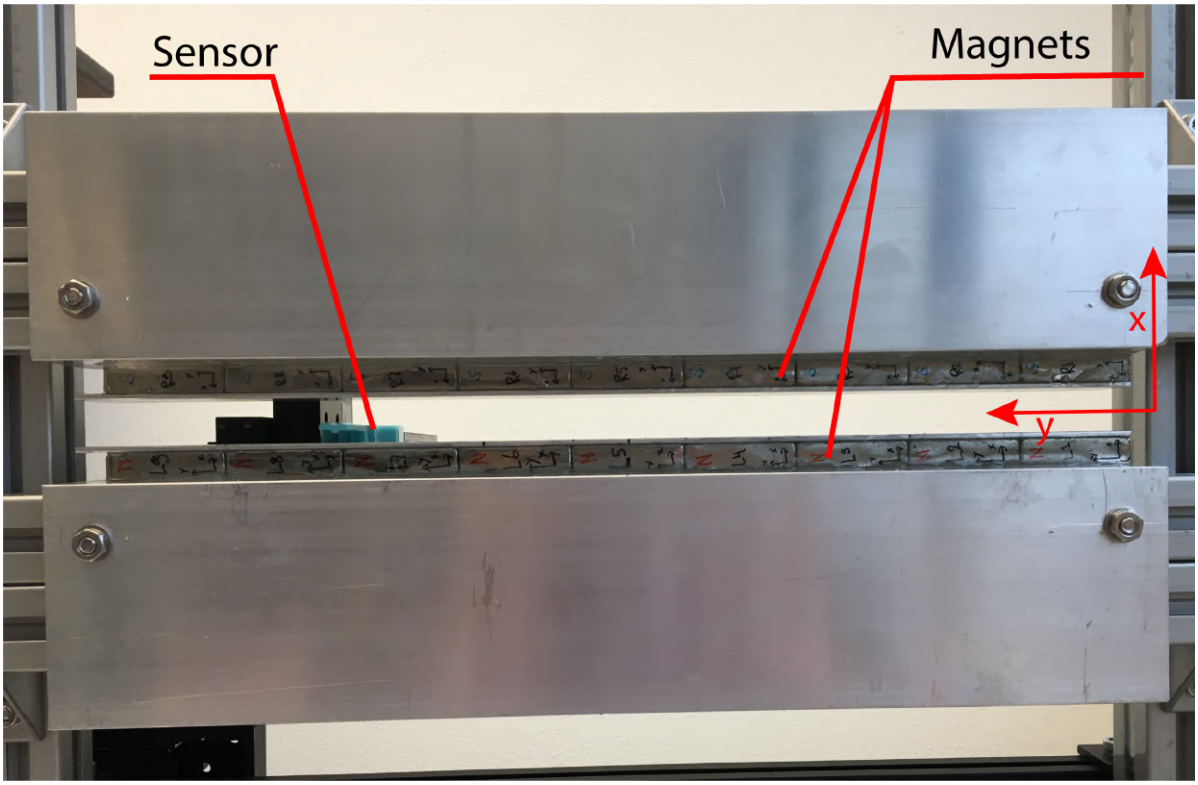

Figure 5.12: Picture of the built experimental setup showing the magnets and the sensor.

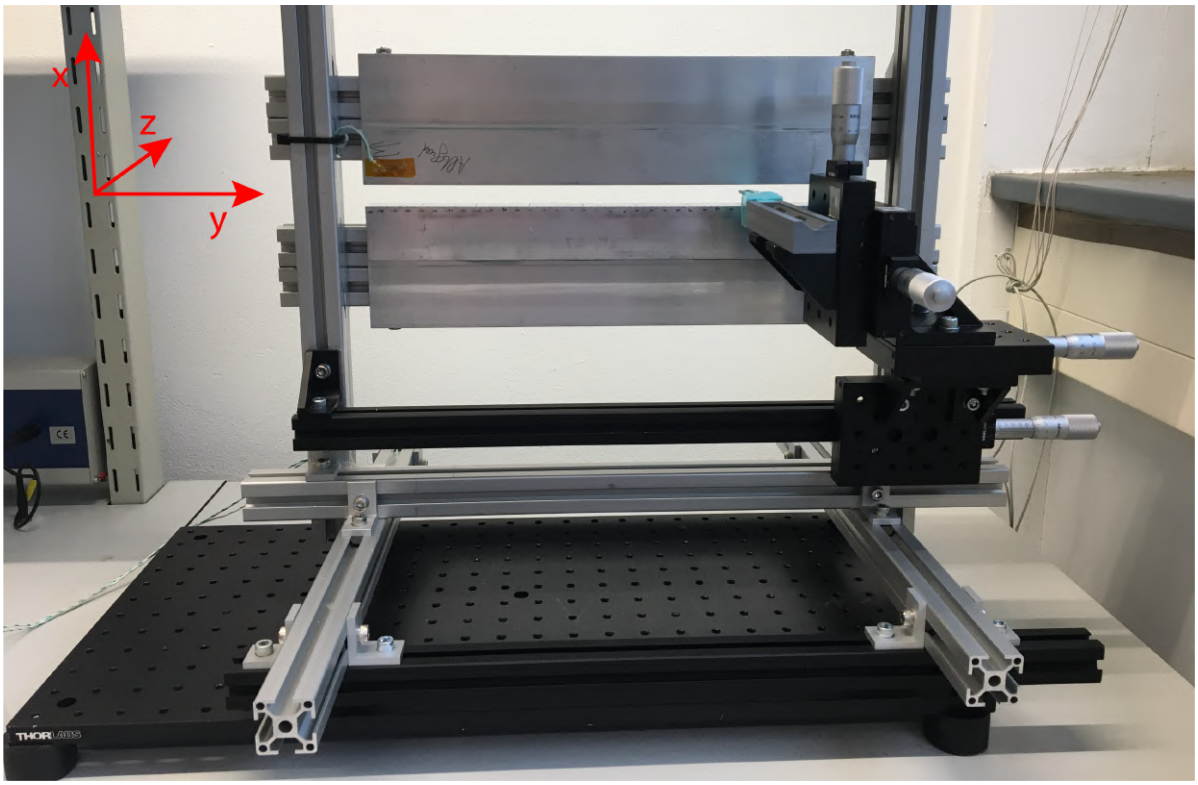

Figure 5.13: Picture of the built experimental setup showing the stage assembly as designed in figure 5.9 .

For the fasteners used to attache the stator assemblies to the main frame, a measurement was conducted to

evaluate their influence on the magnetic field. The conclusions from this experiment is that they are located at a sufficient distance from the measurement locations. Therefore it was concluded that no measurement errors are caused by these parts of the setup.

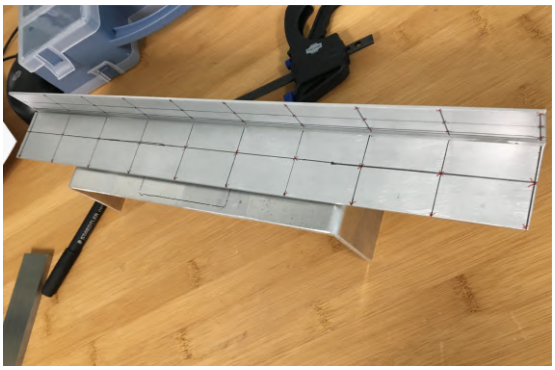

(a) Measurement grid over the alignmet profiles where the thickness is measured.

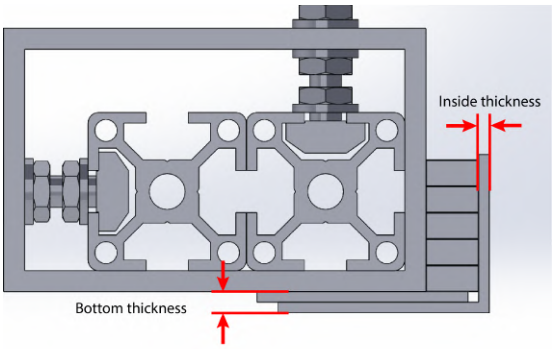

(b) Render indicating the inside and bottom thicknesses that were measured.

Figure 5.14: Thickness measurements of the inside and bottom thickness of the alignment profiles.

The thickness of the alignment strips was measured during the assembly process using a micrometer. For the thickness on the inside a variation range of 0.06 $[mm]$ was measured. On the bottom this was 0.2 $[mm]$, which is significantly larger. This was expected as two profiles are glued together causing a higher variation. These thickness variations are relevant as these surfaces will later be used for the determination of the reference position for the measurements (explained in more detail in the next subsection).

5.6. MEASUREMENT PROCEDURE

Before the measurements can be performed, a measurement procedure is required. For this experimental setup this mainly contains the steps required to determine the reference position of the sensor tip with respect to the magnets. This procedure is discussed for the $x-$ and $z-$directions (short strokes) in section 5.6.1, and in 5.6.2 for the long stroke direction.

5.6.1. REFERENCING POSITION IN x- AND z-DIRECTION

As mentioned in section 5.3.2, the holder of the sensor probe has two referencing surfaces. These are brought in contact with the surface of the aluminium profile to determine the reference position of the hall sensor (at the end of the probe) with respect to the magnets. They are dimensioned such that the Hall element, located at the tip of the flexible probe, is positioned in the location $(x,z) = (-5.5, 4)$ $[mm]$ which corresponds to the top left corner of the measurement grid seen in figure 5.1b. The readings of the $x-$ and $z-$ stage are then noted down, providing the mapping between the coordinates of the sensor and the stage readings. The reproducibility of this operation was determined which resulted in a 3σ repeatability interval of $\approx \pm 0.04$ $[mm]$.

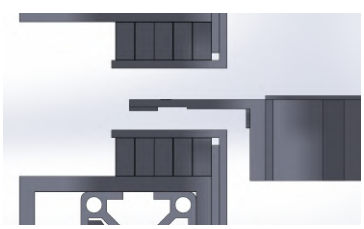

(a) Initial unreferenced state.

(b) Step 1: referening of the $z-$coordinate.

(c) Step 2: referencing of the $x-$coordinate.

Figure 5.15: Overview of the steps involved in the referencing procedure.

5.6.2. REFERENCING POSITION IN THE y-DIRECTION

The referencing in the $y-$direction was done using a tape measure and a camera. When measuring in the long stroke direction, the top $y-$stage (figure 5.9) was used to measure over a range of 25 $[mm]$. The endpoint of this stroke was captured in a picture of the probe tip along with the measurement tape, after which the entire $y-$stage assembly was repositioned on the measurement frame. Subsequently, the bottom $y-$stage ($y2$) was used to line up the end of the previous section, with the beginning of the next measurement section. The tape measure was removed when performing the measurements as it is made of ferromagnetic material, and would ruin the measurements.

(a) Measurement tape placed onto the experimental setup to determine the $y-$position of the sensor.

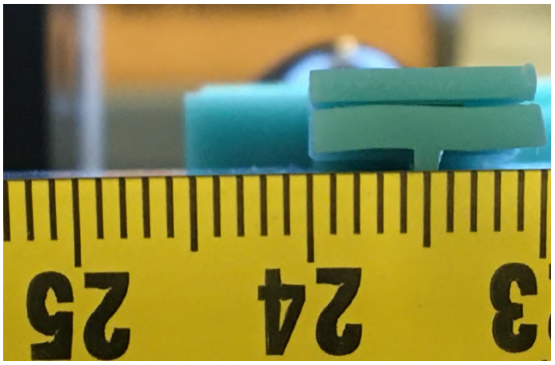

(b) Close up of the sensor along the measurement tape.

Figure 5.16: Referencing process for the $y-$direction.

5.7. CONCLUSIONS

In this chapter the design and realization of the experimental setup has been discussed. The most important conclusions are:

- **Approach**: The chosen approach for the experimental validation is to measure the magnetic field created by the stator as this is the most important factor in the performance of the magnetic gravity compensator.
- **Measurement devices**: The model was used to determine the requirements for the measuring devices. For the position measurement and movement of the sensor probe, linear stages from Thorlabs have been selected. The Hirst GM07 has been chosen for the measurement of the magnetic field.
- **Magnet Tolerance Measurements**: The tolerances of all the 90 stator magnets were measured, starting with the outer dimensions. Using a 3D Helmholtz coil set the magnetic properties were determined. This information from these measurements will be used to determine the expected variations in the magnetic field.

6

MEASUREMENTS AND RESULTS

As explained in chapter 5, the purpose of the experimental validation is threefold. The first goal is to validate the long-stroke concept from a practical perspective. Secondly, it is to validate the model used in the design process, and finally, the setup is used to estimate the performance that is obtained with the used magnets. All of these points will be investigated by measuring the $x-$component of the magnetic field in the air gap between the two stator magnet arrays (see figure 5.1).

In order to draw the necessary conclusions on the points described above, five main measurements have been identified. The measurements and their results are described in sections 6.1 through 6.5 respectively.

1. **Reproducibility measurement**: The first measurement that will be conducted, will be to investigate the reproducibility of the measurement setup. This will later be needed to determine the total uncertainty interval that will be required for the validation of the model.

2. **Validate linearity of magnetic field**: as described in 4.2, the working principle behind this magnet configuration is that the magnetic field in $x-$direction (B_x) grows linearly with the $z-$coordinate. The second measurement will, therefore, validate if the field is indeed linearly increasing with z, thereby adding to the validation of the magnetic configuration and design.

3. **Measure over magnet transition**: In section 5.1 it is explained that magnet transitions in the long-stroke direction, and the rounded magnets edges, could be incorporated in the models used. By measuring over such a transition, the shortcomings of the models are investigated while also providing information if performance issues could arise from these practical aspects.

4. **Measure over long-stroke**: to validate the model, a measurement over the full long-stroke direction will be conducted. This will show the variations in the magnetic field, which can be compared to the uncertainty level calculated in 6.1.2, to determine the validity of the model. Moreover, this measurement will also provide the needed information to estimate the performance of the gravity compensator.

5. **Field weakening at the end of long-stroke**: in section 4.7 the required stator length margin has been determined. This will be validated using a measurement of the magnetic field at the end of the long-stroke direction. This will provide some additional information for the validation of the design.

6.1. REPRODUCIBILITY MEASUREMENT AND UNCERTAINTY INTERVAL

A crucial piece of information to validate the model is to know the 3σ uncertainty interval. This is the interval in which the measurement data should be in, with a 99.7 % certainty. The range of this interval is comprised of several contributions such as variations in the magnet parameters, manufacturing and assembly inaccuracies, and errors due to the measurement procedure. The total value of the 3σ uncertainty level is determined in 6.1.2. However, an important contribution is the reproducibility of the measurement setup, which is discussed in subsection 6.1.1.

6.1.1. MEASUREMENT OF THE REPRODUCIBILITY

The reproducibility of a measurement device or setup describing its ability to repeatedly perform the same measurement. In the case of the experimental setup in this study, this mainly comes down to the combination of the ability to measure repeatedly in the same location, and the reproducibility of the sensor. The reproducibility is determined by means of performing multiple consecutive measurements where it is attempted to measure at the same locations. This is done in the long-stroke direction, at the coordinates:

$$x = -5\ [mm]$$
$$y = 0,\ 5,\ 10,\ 15,\ 20,\ 25,\ [mm]$$
$$z = 3.5\ [mm],$$

which are the coordinates of the left top corner of the mover magnet in the nominal $x-$ and $z-$ position. In total 5 sets of measurements are performed.

In between each measurement, the stage assembly is unscrewed and "re-positioned" at the same location. Then the referencing procedure (see section 5.6) is used to determine the $x-$ and $z-$ stage readings in the reference position, after which the measurements are taken. The measurement results can be seen in figure 6.1. From these measurements, the RMS error is determined over all the measurement locations, from which the reproducibility is calculated resulting in a value of $\pm 0.53\ [mT]$

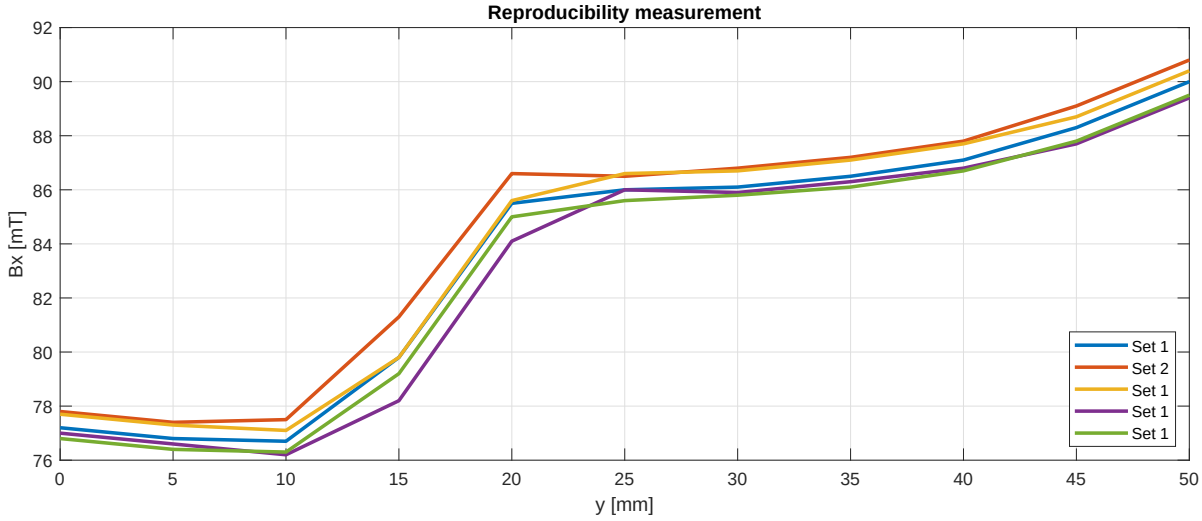

Figure 6.1: Measurement results of reproducibility measurement.

6.1.2. 3σ UNCERTAINTY INTERVAL

The uncertainty of the measurement is categorized into the following contributions:

- **Magnet tolerances**: these are the contributions to the variations in the measurements as a result of the magnet tolerances. They are quantified using 2D FEM simulations and the 3D analytical surface charge model. The input for the tolerances is taken from the measured values presented in section 5.4.
- **Magnet assembly and placement errors**: the magnet placement and orientation in the experimental setup is not perfect. Estimations of the errors in the positioning and orientation of the magnets are made and subsequently used as input to the model. This results in approximations of the contribution of these assembly inaccuracies to the measurement variations. The position errors used are 0.1 $[mm]$, and the rotation error (around the $y-$axis) is estimated at 0.1 $[deg]$. The error due to the gap size refers to the error in the distance between the two stator arrays and is estimated at a maximum of 0.1 $[mm]$.
- **Measurement procedure and referencing surfaces**: the uncertainty from the referencing procedure (and thus the measurement device) has been determined with the reproducibility measurement from the previous section. The inaccuracies of the reference surface refer to the non-uniformity in the thickness of the alignment strip as described in section 5.5.

- **Temperature**: finally, from the temperature measurements a variation of approximately 3 $[°C]$ in the temperature have been measured. Using the temperature coefficient of 0.1 $[\%/°C]$ for both the magnets and the measurement device, the measurement variation was determined.

Table 6.1: Overview of Contributions to Measurement Uncertainty

Contribution	**Value** $[mT]$	**Value Squared** $[mT^2]$
Magnet tolerances		
Magnetization strength	2.0	4.0
Magnetization angle	7.9	62.4
Mechanical dimensions: width	0.3	0.09
Mechanical dimensions: height	0.7	0.49
Magnet assembly and placement errors		
Magnet placement $x-$dir.	0.2	0.04
Magnet placement $y-$dir.	0.5	0.3
Magnet placement $z-$dir.	1.6	2.6
Rotation of full stack	5.0	25.0
Stator gap size	1.0	1.0
Measurement procedure and referencing surfaces		
Thickness variation in alignment strip	1.5	2.3
Reproducibility of setup	0.5	0.3
Temperature		
Magnets	0.3	0.09
Measurement device	0.3	0.09
	Sum	98.5
	Resulting 3σ value	$\sqrt{98.5} = 9.9$ $[mT]$

The total uncertainty is determined as the root-squared sum of all the contributions resulting in a value of 9.9 $[mT]$. This value will be used mainly in section 6.4 for the purpose of model validation. Note that in table 6.1 the tolerance for the dimensions of the depth is not taken into account. This is correct since the magnets are positioned such that the lengths of all magnets are matching in the depth direction (explained in detail in section 5.5). Variations in the depth directions have therefore no influence in the local magnetic field.

6.2. MEASUREMENT OF LINEARITY MAGNETIC FIELD

To verify the linearity of B_x with the $z-$coordinate, measurements have been conducted over a grid of $x-$ and $z-$coordinates at multiple $y-$coordinates. The minimal and maximal values of the $x-$ and $z-$coordinates are selected as the coordinates of the corners of the mover magnet in the extreme positions of the short-strokes (see figure 6.2).

The $y-$coordinates of the measurement are $y = -120$ $[mm]$ and $y = 10$ $[mm]$. The measurement results can be seen in figure 6.3, on the left. On the right, the results from the model are added for comparison.

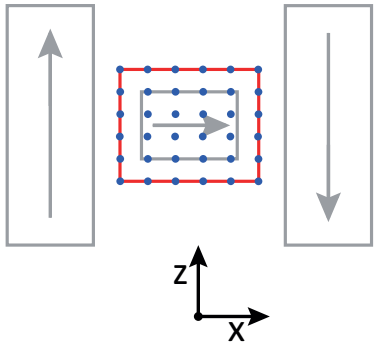

Figure 6.2: Measurement grid over the short-stroke directions (x and z).

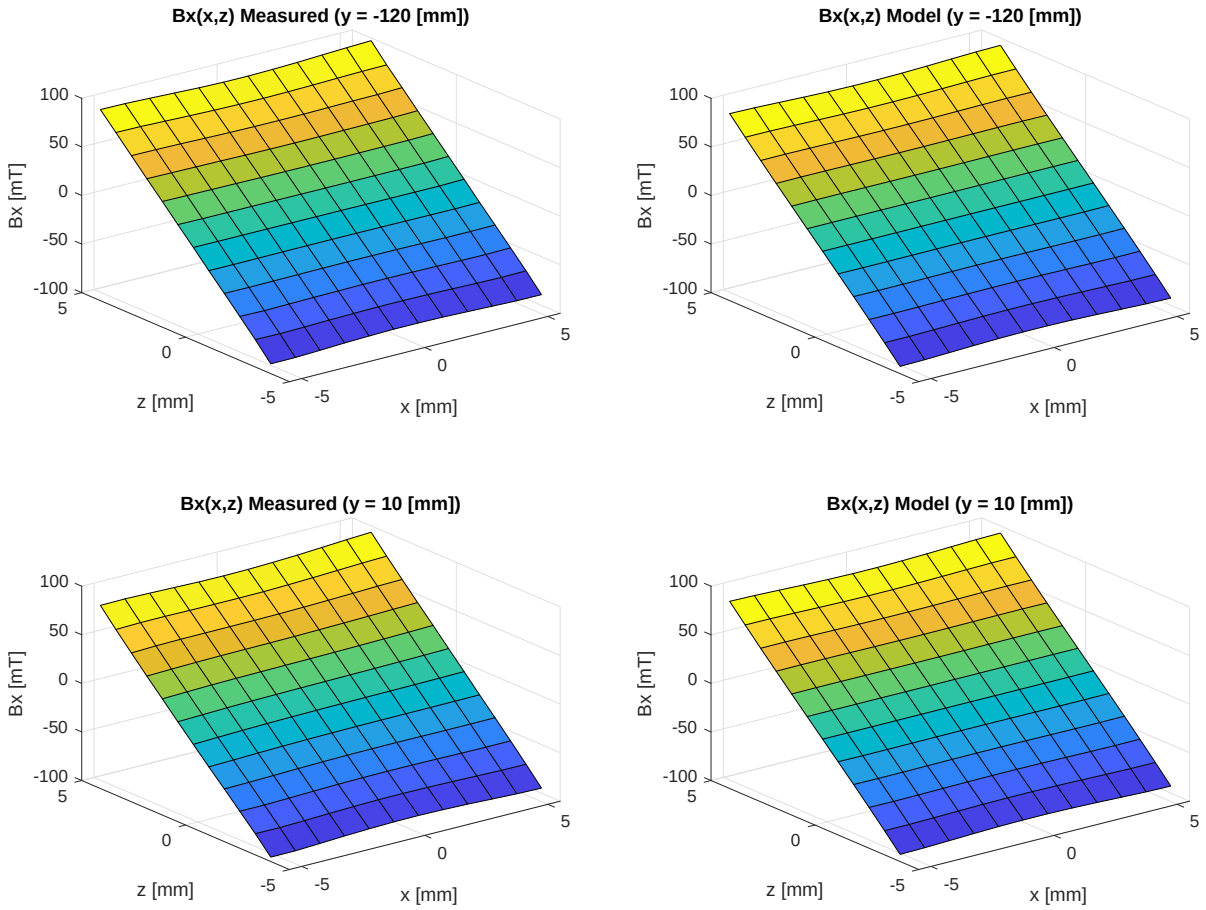

Figure 6.3: Measured magnetic field over the short stroke directions (x and z) compared to the expected values from the model.

Additionally, for $y = -120[mm]$ a comparison is made between the model, and the measurements over the $z-$coordinate for three $x-$positions (see 6.3 in the left top for clarity). The other three figures in 6.3 show the comparison in a 2D graph. The expected slope of the B_x field with the $z-$coordinate is 22.2 $[mT/mm]$. From the measurement results the average slope found to be 22.2 $[mT/mm]$, showing very good accordance with the model. Also, from all figures, it can be seen that the B_x component of the magnetic field is indeed linearly increasing with the $z-$coordinate in the required region of the mover magnet.

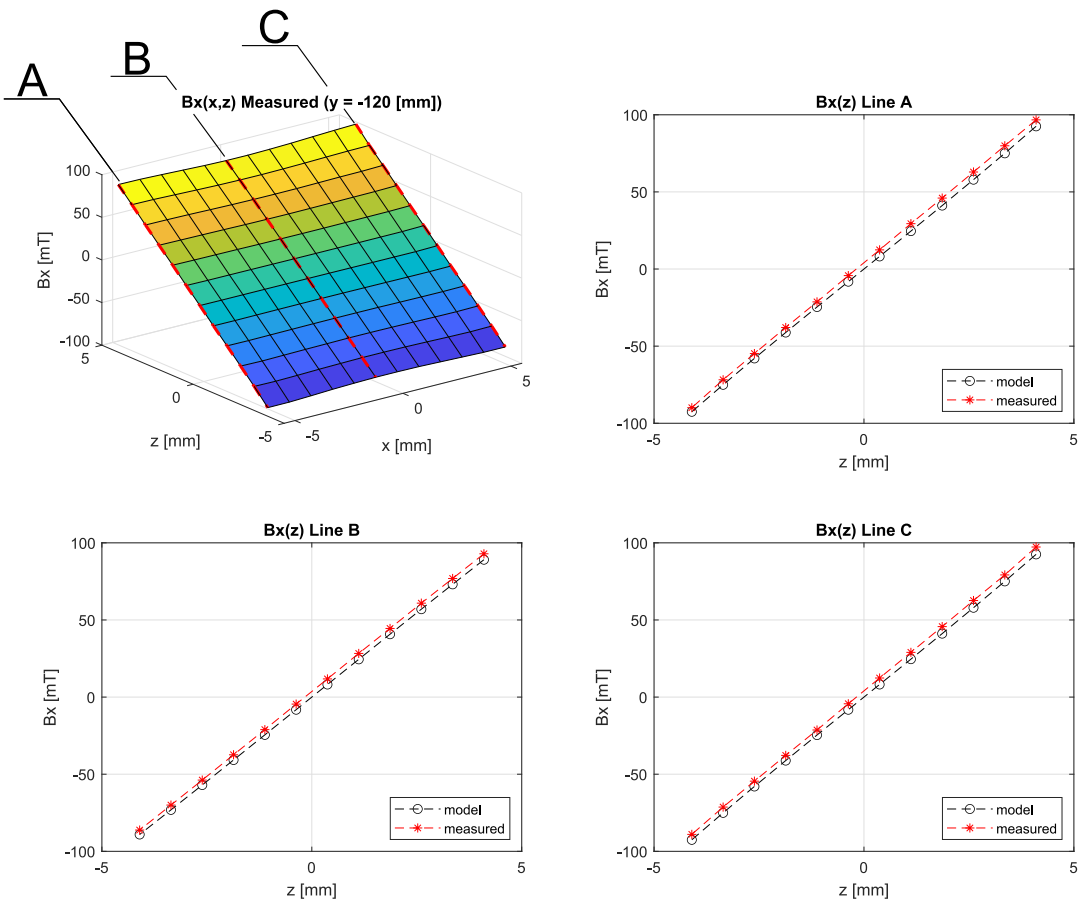

Figure 6.4: The linearity of the measured magnetic field with the z coordinate compared to the expected values of the model.

6.3. MEASUREMENT OF MAGNET TRANSITION

The purpose of this measurement is to investigate if local spikes in the magnetic field are present due to magnet transitions (in the long-stroke direction) and/or due to the rounded edges of the magnets. With this measurement, the simplification of modeling the magnets as perfectly cuboidal can be validated. Furthermore, if large fluctuations are observed, the resulting effect on the performance can be estimated.

To investigate this, a fine measurement over a magnet transition has been performed, using a very small step size: $dy = 0.05$ $[mm]$. The $x-$coordinate chosen for these measurements is $x = -4.90$ $[mm]$, as it is the closest possible coordinate to the left stator, therefore providing the most potential to measure a fluctuation in the field. Two measurement sets were obtained at different $z-$coordinates. The first one being at $z = 3.83$ $[mm]$ which is around the coordinate of the top surface of the mover magnet. This will result in a measurement of the field at the relevant field strength (around 85 $[mT]$). At this field strength, the resolution of the Hirst GM07 is 0.1 $[mT]$. The second measurement was performed at $z = 0.43$ $[mm]$ where the field expected is around 10.5 $[mT]$. This was done to be able to use a different measurement range of the Hirst GM07 with a higher resolution, namely 0.01 $[mT]$.

The measurement was conducted over a total stroke of 5 $[mm]$ in the $y-$direction, where the magnet transition was located at $y = 20$ $[mm]$. The results can be seen in figure 6.5.

From these figures, it can be concluded that the transitions between the stator magnets is gradual and that there no spikes are present in the magnetic field that are relevant for the functioning of the gravity compensator. In other words; the transitions between the magnets and the rounded edges do not pose any limitations on the performance of the long-stroke gravity compensator.

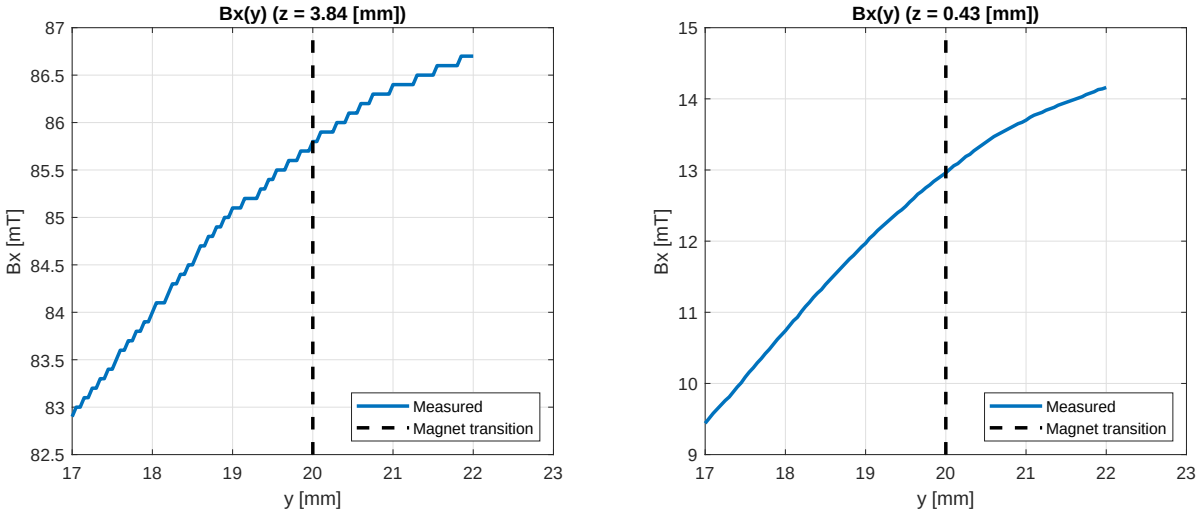

Figure 6.5: Measurement over magnet transition.

6.4. MEASUREMENT OF FULL LONG-STROKE

The purpose of this measurement is to validate the model and to estimate the performance of the gravity compensator built in the experimental setup. This is done by measuring the B_x field at the corners of the mover magnet (when it is in the nominal $x-$ and $z-$position), over the entire long-stroke direction.

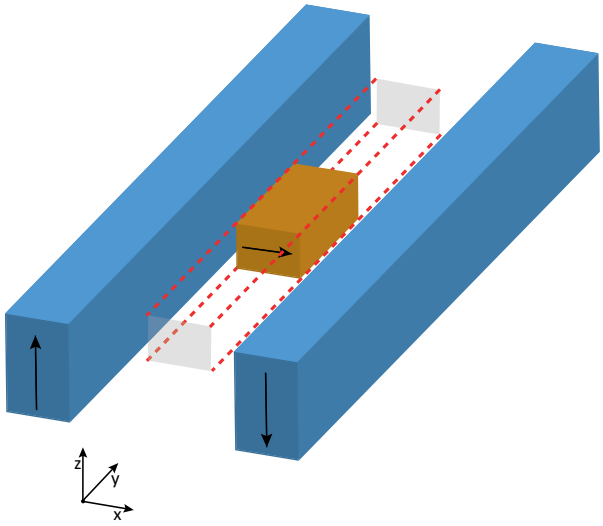

Figure 6.6: Measurement lines over the corners of the mover magnet (indicated in red) were used for the long-stroke measurement.

The model validation is done by examining the fluctuations in the measurement data and comparing it to the expected uncertainty interval calculated in subsection 6.1.2. The fluctuations will also be used to estimate the performance of the gravity compensator. How this is done is explained in subsection 6.4.2. The measurement results are presented in subsection 6.4.1 after which the performance is estimated in 6.4.3.

6.4.1. MEASUREMENT RESULTS

In figures 6.7a, 6.7b, 6.7c, and 6.7d the results can be seen of magnetic field measured over the long-stroke. The model prediction is indicated with the black dotted line, and the 3σ uncertainty interval is indicated with the two red dotted lines. The locations at which the magnet transitions take place are indicated with the vertical dotted lines.

Important to note is that the discontinuities seen in the figures, are caused by the measurement procedure, and are not caused by the magnets of the gravity compensator. As explained in section 5.6, the movement

range of the setup is limited to only 25 [mm]. In the long-stroke direction, it is, therefore, necessary to reposition the stage assembly after 25 [mm]. The end of the previous stroke, and the beginning of the next never perfectly line up, causing the discontinuities observed.

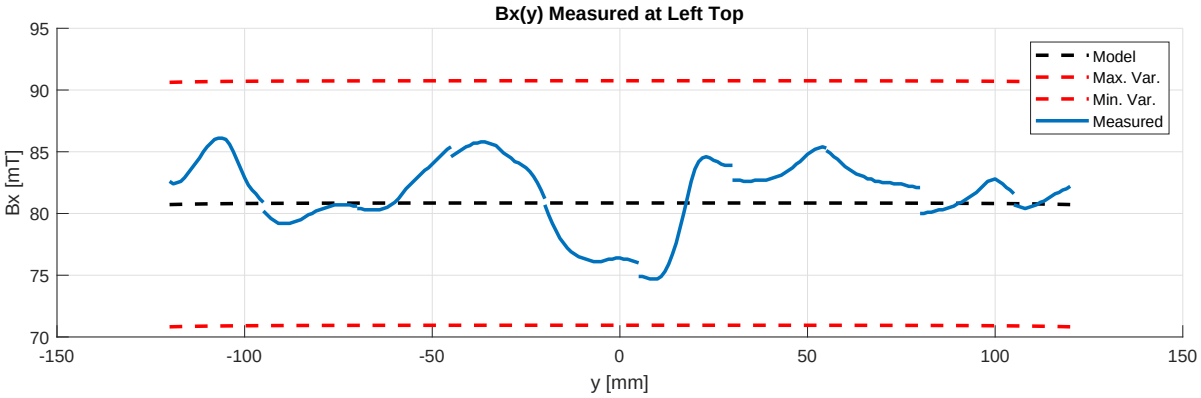

(a) Left top

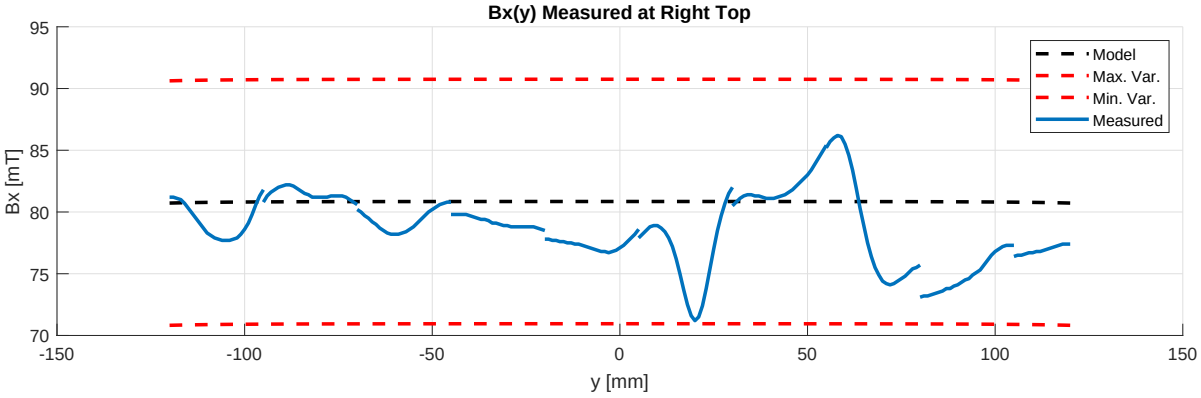

(b) Right top

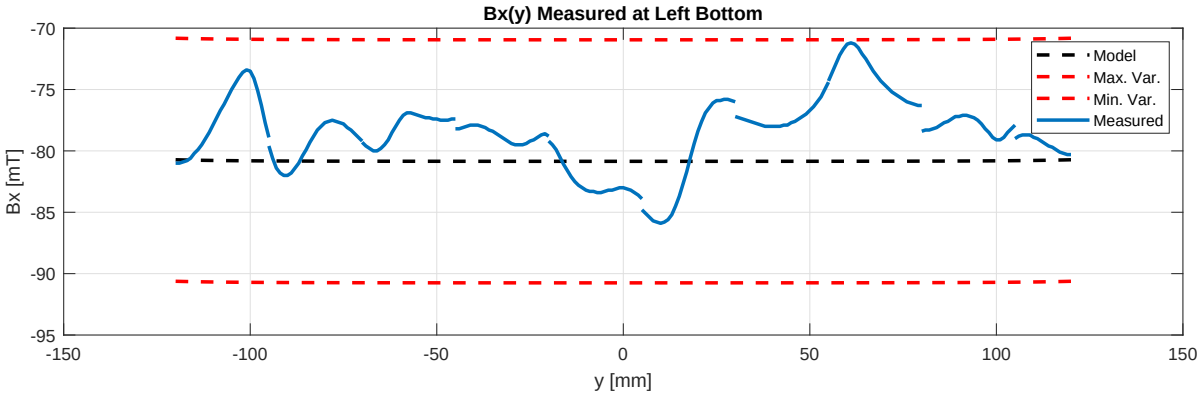

(c) Left bottom

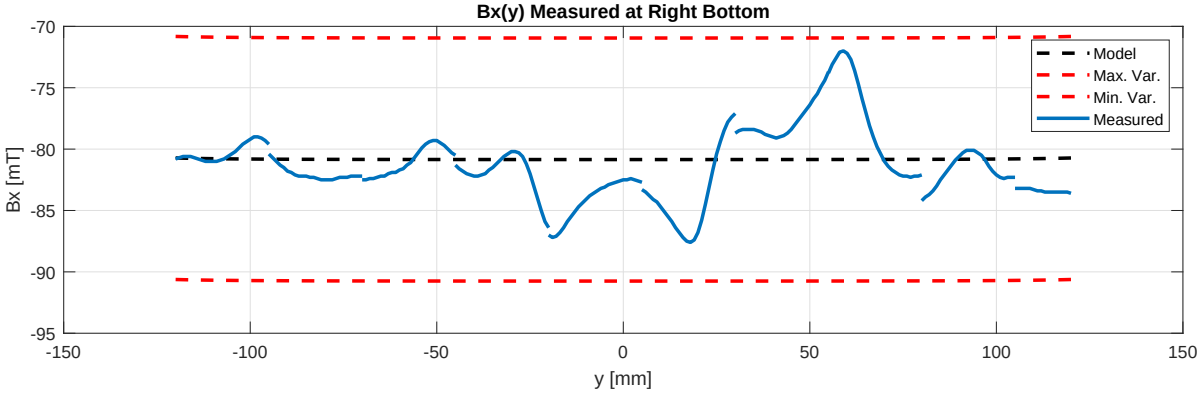

(d) Right bottom

Figure 6.7: long-stroke measurement results

From the results presented in figure 6.7 it can be seen that the measurement results remain within the expected 3σ uncertainty interval, therefore leading to validation of the model.

6.4.2. APPROACH TO PERFORMANCE ESTIMATION

To estimate the performance of the gravity compensator a method is necessary, to translate the measured magnetic field to the resulting forces and stiffnessess. In section 4.2 it was explained that the force on the mover is a result of the integral of the magnetic field over the surfaces of the mover magnet. This fact can be used to estimate the performance of the gravity compensator. The idea is to translate the force and stiffness requirements to maximum allowable variations in the magnetic field. These can subsequently be compared to the measurement data, to draw conclusions on the performance.

The first step is to find the relation between the magnetic field, B_x, at the top and bottom side of the mover magnet, and the resulting force. From the coil model the force on the mover magnet van be written as:

$$F = \left[\int (\boldsymbol{K} \times \boldsymbol{B}) da\right]_{top} + \left[\int (\boldsymbol{K} \times \boldsymbol{B}) da\right]_{bottom}. \tag{6.1}$$

In the ideal case (all magnets are nominal), the magnetic field over the top and bottom surfaces is constant. Also the current density $\boldsymbol{K}$, and obviously the magnet dimensions are also constant. Therefore equation 6.1 can be simplified into

$$F = CB, \tag{6.2}$$

where B equals the magnetic field felt by the top and bottom surfaces of the magnet, and C represents the integral of the current density over the magnets surfaces. Using the expected magnetic field, and the resulting force in the ideal case, the constant C can be determined. The force on the magnet in that case, is equal to the required load capacity (as it has been designed as such) of a single gravity compensator (65.4 $[N]$), and the magnetic field at the mover magnet surfaces equals 80.8 $[mT]$. Constant C thus equals

$$C = \frac{F}{B} = \frac{\frac{1}{3} \cdot 20\,[kg] \cdot 9.81\left[\frac{m}{s^2}\right]}{80.8\ [mT]} = \frac{65.4\ [N]}{80.8\ [mT]} = 0.81\left[\frac{N}{mT}\right]. \tag{6.3}$$

Equation 6.2 together with the found value for C can now be used to translate the force and stiffness requirements to requirements on the magnetic field.

MAXIMUM ABSOLUTE STIFFNESS REQUIREMENT

For the maximal value of the stiffness, the derivative of the force is taken with respect to the $y-$coordinate, resulting in

$$\frac{dF}{dy} = C\frac{dB}{dy}. \tag{6.4}$$

As the current density and the mover magnet dimensions are constant, only the derivative of the magnetic field needs to be taken. For a single gravity compensator the maximum value of the stiffness is $\frac{1000\ [N/m]}{3} = 333\ \left[\frac{N}{m}\right]$. Substituting this in equation 6.4, results into

$$\frac{dB_x}{dy}_{max} = \frac{1}{C}\frac{dF}{dy}_{max} = \frac{1}{0.81\left[\frac{N}{mT}\right]} \cdot 333\left[\frac{N}{m}\right] = 410\left[\frac{mT}{m}\right] = 0.41\left[\frac{mT}{mm}\right]. \tag{6.5}$$

MAXIMUM CHANGE OF STIFFNESS REQUIREMENT

For the maximum change of the stiffness the same approach is used, however, now using for the value of the maximum allowable derivative $\frac{200\left[\frac{N}{m}\right]}{3} = 66\ \left[\frac{N}{m}\right]$.

$$\frac{dB_x}{dy}_{max} = \frac{1}{C}\frac{dF}{dy}_{max} = \frac{1}{0.81\left[\frac{N}{mT}\right]} \cdot 66\left[\frac{N}{m}\right] = 82\left[\frac{mT}{m}\right] = 0.08\left[\frac{mT}{mm}\right]. \tag{6.6}$$

Important to note is that these requirements for the maximum derivatives of the magnetic field represent linear changes in the magnetic field over the full length of the mover magnet. In other words, the magnetic field has to have a derivative of 0.41 $\left[\frac{mT}{mm}\right]$ over the entire length of the mover magnet to result into a stiffness of 333 $\left[\frac{N}{m}\right]$. This is graphically represented in figure 6.8. To estimate the effect of derivatives sustained over shorter lengths, a correction factor should be used to accommodate for the length over which the derivative is present.

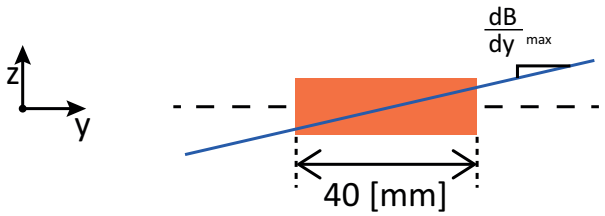

Figure 6.8: Maximum derivative of the magnetic field in the case of a constant derivative over the full length of the mover magnet.

FORCE ERROR REQUIREMENT

The fore error requirement for a single gravity compensator equals $F_{e,max} = \frac{1\,[N]]}{3} = 0.33\,[N]$. Similarly to the requirements of the stiffness and the change of the stiffness, equation 6.2 can be used to translate the force error requirement into a requirement for the magnetic field.

$$B_{x,max} = \frac{F_{e,max}}{C} = \frac{0.33\,[N]}{0.81\,[\frac{N}{mT}]} = 0.40\,[mT]\,. \tag{6.7}$$

Note, that this also only holds for an average value of the magnetic field over the entire length of the mover magnet.

6.4.3. PERFORMANCE ESTIMATION FROM LONG-STROKE MEASUREMENTS

Firstly the stiffnesses are computed from the measurement data with the highest derivative. These are located in the measurement data of the right top measurement. From the data the derivative is estimated, which can be seen in figure 6.9.

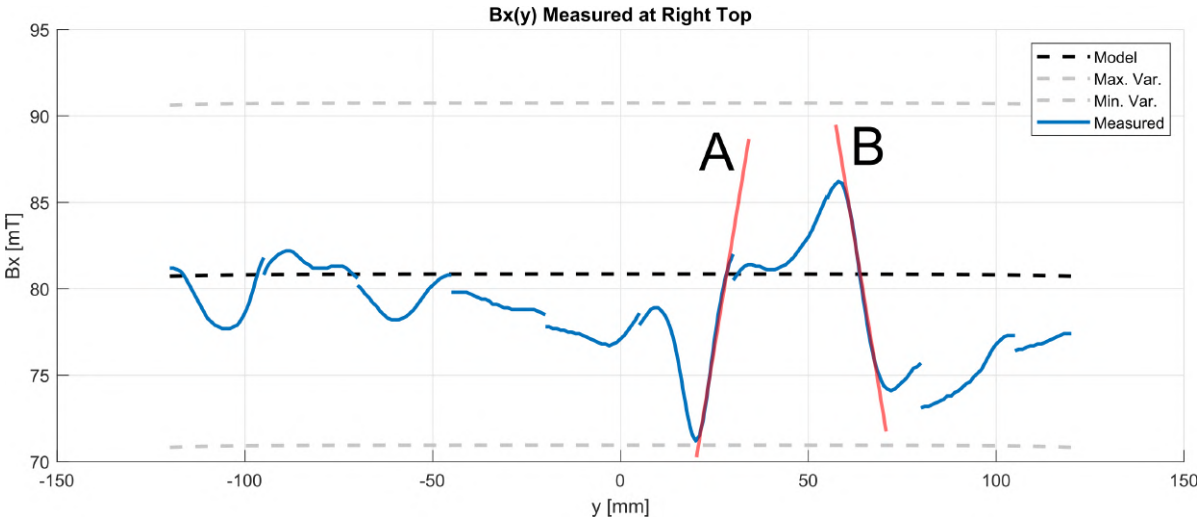

Figure 6.9: Estimation of the stiffness from the highest derivatives found in the long-stroke measurements.

From the derivatives, the effective stiffness is calculated. Note that these high derivatives are not sustained over the entire length of the mover magnet. This is compensated for with a linear approximation (see table

Table 6.2: Estimated stiffnesses from highest derivatives

	Maximal Positive Derivative (A)	**Maximal Negative Derivative (B)**
Derivative	$1.25\ [mT/mm]$	$-0.92\ [mT/mm]$
Sustained over	$8\ [mm]$	$13\ [mm]$
Effective derivative	$1.25 \cdot \frac{8}{40} = 0.25\,[mT/mm]$	$-0.92 \cdot \frac{13}{40} = -0.30\,[mT/mm]$
Resulting stiffness (1 g.c.)	$\frac{0.25}{0.41} \cdot 333 \approx 200\ [N/m]$	$\frac{-0.30}{0.41} \cdot 333 \approx -240\ [N/m]$
Resulting stiffness (3 g.c.)	$3 \cdot 200 \approx 600\ [N/m]$	$3 \cdot -240 \approx -720\ [N/m]$

The same is done for two regions where the derivatives are sustained over approximately the entire mover magnets length. The stiffnesses are determined in the same manner.

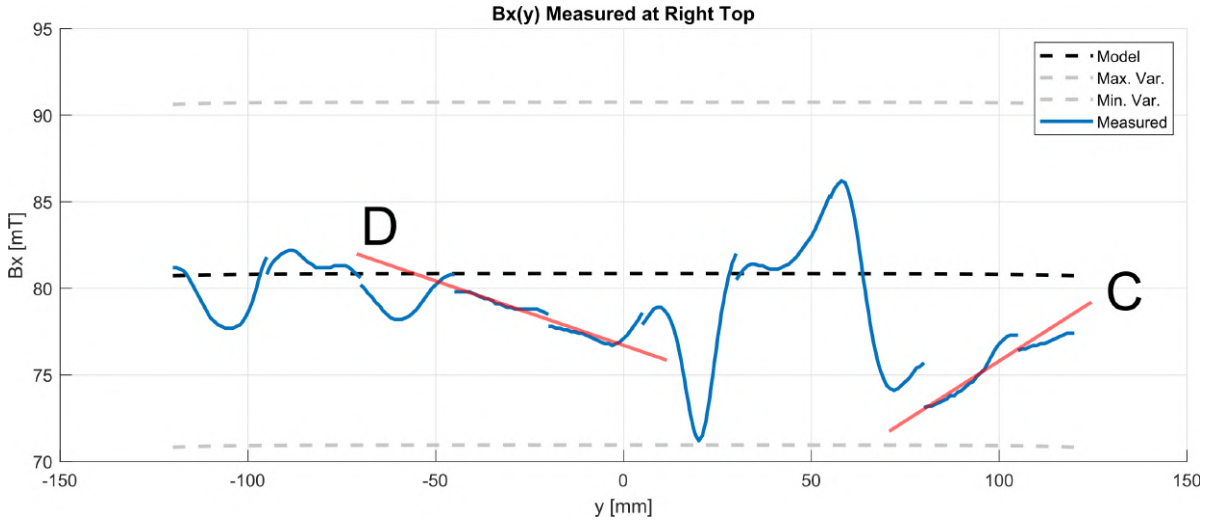

Figure 6.10: Estimation of the stiffness from regions with a constant derivative of the magnetic field with a length of approximately the mover magnet length.

Table 6.3: Estimated stiffnesses from longer sustained derivatives

	Positive Derivative (C)	**Negative Derivative (D)**
Derivative	$0.11\ [mT/mm]$	$-0.07\ [mT/mm]$
Sustained over	$38\ [mm]$	$42\ [mm]$
Effective derivative	$0.11 \cdot \frac{38}{40} = 0.11\ [mT/mm]$	$-0.07 \cdot \frac{42}{40} = -0.08\ [mT/mm]$
Resulting stiffness (1 g.c.)	$\frac{0.11}{0.41} \cdot 333 \approx 84\ [N/m]$	$\frac{-0.08}{0.41} \cdot 333 \approx -63\ [N/m]$
Resulting stiffness (3 g.c.)	$3 \cdot 84 \approx 252\ [N/m]$	$3 \cdot -63 \approx -189\ [N/m]$

For the force error the measurements taken in the top left corner are used. Two regions have been identified where the average magnetic field has been calculated. These regions have been indicated in figure 6.11, and the resulting force and force error are calculated. For the results see table 6.4.

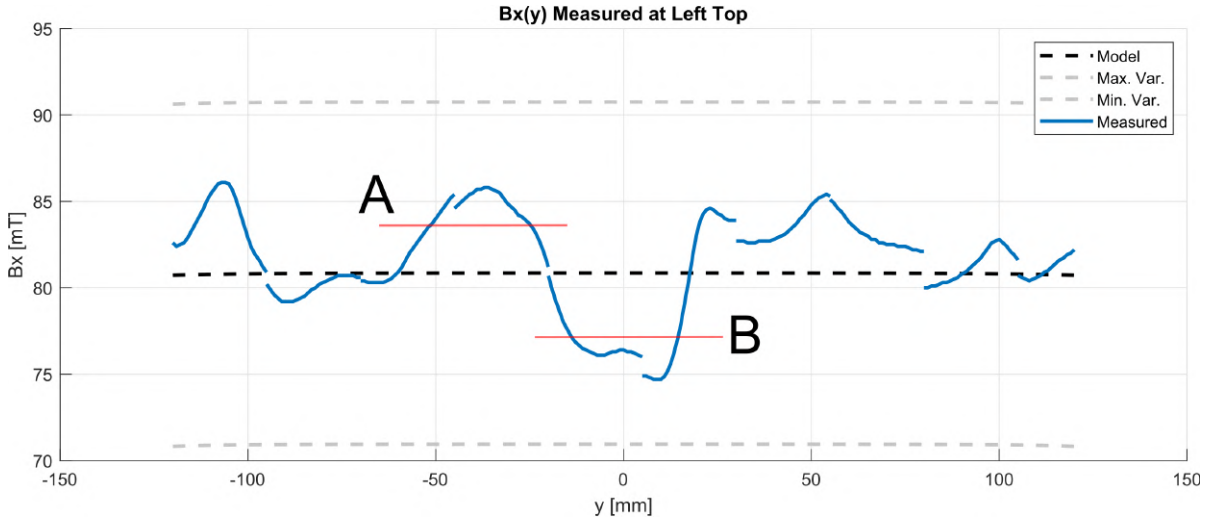

Figure 6.11: Estimation of the force error from the long-stroke measurements.

Table 6.4: Estimated force error from measurements

	Above Nominal (A)	**Below Nominal (B)**
Average field	84.1 $[mT]$	76.6 $[mT]$
Sustained over	39 $[mm]$	38 $[mm]$
Effective field strength	$84.1 \cdot \frac{39}{40} = 82.0\,[mT]$	$76.6 \cdot \frac{38}{40} = 72.8\,[mT]$
Resulting force	$82.0\ [mT] \cdot 0.81\,[N/mT] \approx 66.4\ [N]$	$72.8\,[mT] \cdot 0.81\,[N/mT] \approx 59.0\ [N]$
Resulting force error (1 g.c.)	$66.4\,[N] - 65.4\,[N] \approx 1.0\,[N]$	$65.4\,[N] - 59.0\,[N] \approx 6.4\,[N]$
Resulting force error (3 g.c.)	$3 \cdot 1.0 \approx 3\ [N]$	$3 \cdot 6.4 \approx 19.2\ [N]$

6.5. MEASUREMENT OF FIELD WEAKENING AT END OF LONG-STROKE

In section 4.7 the required length margin in the long-stroke direction was determined. One additional measurement was performed to validate this result. This is done by measurement of the magnetic field at the end of the long-stroke, where the field is expected to weaken. Just like in the previous measurement, the $x-$, and $z-$coordinates at which the measurements are taken, correspond to the corners of the mover magnet when it is in its nominal position. This is schematically depicted in figure 6.12.

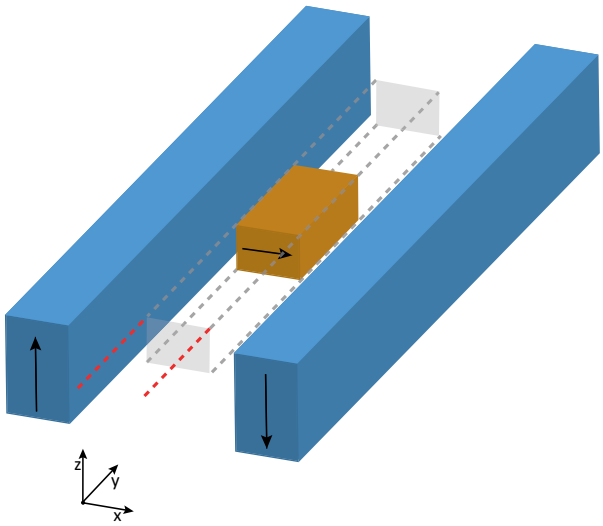

Figure 6.12: Measurement lines over the top corners of the mover magnet (indicated in red) were used for the end-of-stroke field weakening measurement.

In a similar fashion to the way that the performance was estimated from the long-stroke measurements, an estimation can be made of the stiffness in this region. This can subsequently be compared to the results found in section 4.7. The results of the measurements are shown in figure 6.13

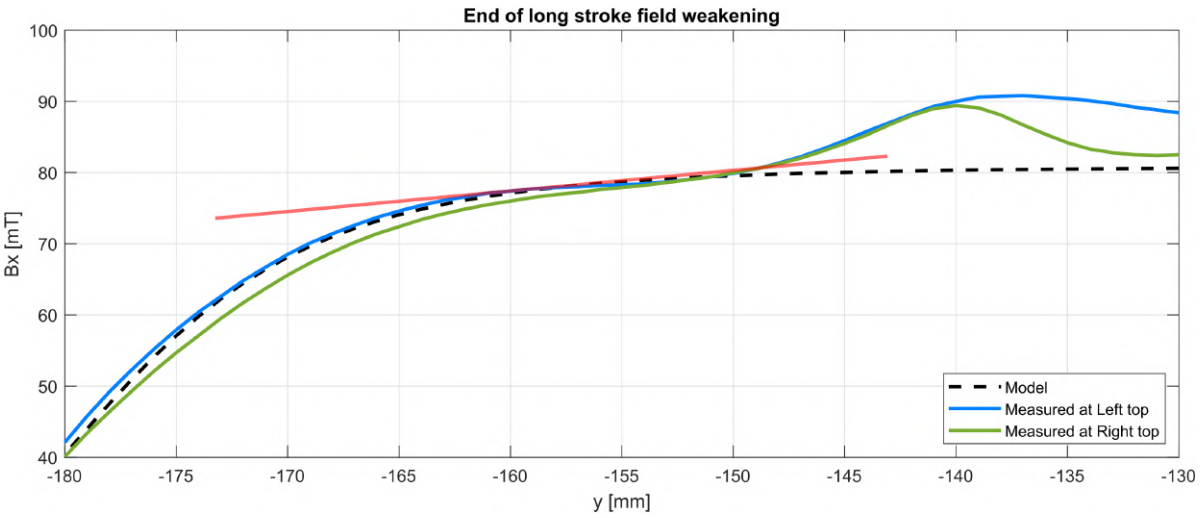

Figure 6.13: Magnetic field measured at the end of the long-stroke.

The derivative of the measured data is taken, after which it compared to the stiffness requirement. The coordinate is determined for which the derivative is larger than $\frac{dB_x}{dy}_{max} = 0.41\ \left[\frac{mT}{mm}\right]$, which was found to equal $y = -160\ [mm]$, which results in a margin of $160\ [mm] - 120\ [mm] = 40\ [mm]$. This leads to the conclusion that to ensure that the stiffness remains below the required 1000 $\left[\frac{N}{m}\right]$, a stator length margin of 40 $[mm]$ in the long-stroke direction is required. This is in good accordance with the found 48 $[mm]$ in section 4.7. The difference between the two is the result of the fact that in section 4.7 a different criterion was used to determine the required length margin. There a maximum change of 4 $\left[\frac{N}{m}\right]$ in the stiffness due to the edge effects at the end of the long-stroke was used. This translates to a derivative of

$$\frac{dB_x}{dy}_{max} = \frac{1}{C}\frac{dF}{dy}_{max} = \frac{1}{0.81\left[\frac{N}{mT}\right]} \cdot 4\left[\frac{N}{m}\right] = 4.9\left[\frac{mT}{m}\right] = 0.0049\left[\frac{mT}{mm}\right]. \tag{6.8}$$

A derivative this low could not be obtained in this setup, as can also be concluded from the measurements and results presented in the previous section.

6.6. CONCLUSIONS FROM MEASUREMENTS

In this section the conclusions from the performed measurements are presented. They are linked to the goals described at the beginning of this chapter.

1. **Validate the magnetic design and long-stroke concept**: In measurement number two, the linearity of the model was measured, leading to the conclusion that the stator indeed processes a linear growing field. This is an important result as it is the fundamental working principle of the gravity compensator. Secondly, in a fine measurement over a magnet transition, no fluctuations in the magnetic field were observed that could harm the performance of the gravity compensator. From this data, the practical aspects of the long-stroke gravity compensator have been validated.

2. **Validate the model**: The reproducibility was measured at $\pm 0.53\ [mT]$, contributing to the total uncertainty level of 9.9 $[mT]$. From the measurements in the long-stroke direction, it is concluded that all measurement data remains within the 3σ uncertainty interval, thereby validating the model.

3. **Estimate the achieved performance**: Finally, the performance of the gravity compensator was estimated using linear approximations where the force and stiffness requirements are translated to requirements of the B_x field. This resulted into estimations of the maximal stiffness of $\approx 240\ [N/m]$, a maximal peak to peak change of the stiffness $\approx 440\ [N/m]$, and a force error of $\approx 6.4\ [N]$. As these estimations are resulting from only a single gravity compensator, and three will be needed for the eventual implementation, the eventual performance parameters are: maximal stiffness of $\approx 720\ [N/m]$, a peak to peak change in the stiffness of $\approx 1320\ [N/m]$, and a force error of $\approx 19.2\ [N]$. From these results it is concluded that the requirements cannot be met using standard stock magnets.

7

ACHIEVABLE PERFORMANCE AND RECOMMENDED IMPLEMENTATION

7.1. GOAL

The performance estimation presented in subsection 6.4.3 based on the measurement data showed that the performance requirements cannot be met using standard stock magnets. In this chapter, it is investigated how a long stroke magnetic gravity compensator can be successfully implemented in a nanometer precision positioning machine. This is done by examining the effect of the magnetic tolerances on the achievable performance.

In section 4.4 a similar investigation was performed, however, this was limited to a 2D study. In this chapter a more elaborate 3D method will be employed, where the final foal is to determine the needed magnetization tolerances to meet the design specifications as stated in table 1.1.

7.2. MONTE CARLO SIMULATION

The approach used to achieve this is to perform a Monte Carlo Simulation. This is a method where the effect of randomly distributed design parameters is statistically investigated. In this study, this boils down to generating magnetic tolerances for a long stroke magnetic gravity compensation system and calculating the resulting performance parameters. This process is repeated for a specified number of iterations where for each iteration the achieved performance is saved. When all iterations are completed, the resulted performance can be examined statistically examined.

The 3D surface charge model is used to calculate the interaction forces on a three-dimensional grid over the full mover strokes (see table 1.1). The investigated performance parameters are the maximum force error, the peak to peak stiffness change, and the maximum force error. The included tolerance values are the variations in the magnetization strength and the magnetization angle and they are assumed to be normally distributed. The results of these simulations are presented in the following subsections.

7.2.1. STANDARD STOCK MAGNETS

Firstly a Monte Carlo simulation is performed using the specifications of magnets from the experimental setup. This serves as a verification of the performance estimated from the measurements from the magnetic field. The 3σ values specified for the normal distribution of the magnetization strength and the mangetization angle are 2.8 % and 2.7 $[deg]$ respectively. These are directly obtained from the measurement data presented in section 5.4 (table 5.6). The dimensions of the magnets used equal those used in the experimental setup (see table 5.4)

Figure 7.1 show the distribution of the generated magnetic tolerances of the simulation. The resulting mean maximal stiffness is 756 $[N/m]$, the mean peak to peak change of the stiffness is 1105 $[N/m]$, and the mean force error is 15 $[N]$. These are all in good accordance with the estimations obtained from the measurement data. It can be concluded that the stiffness requirements are met in approximately 80 % of the cases, however, the

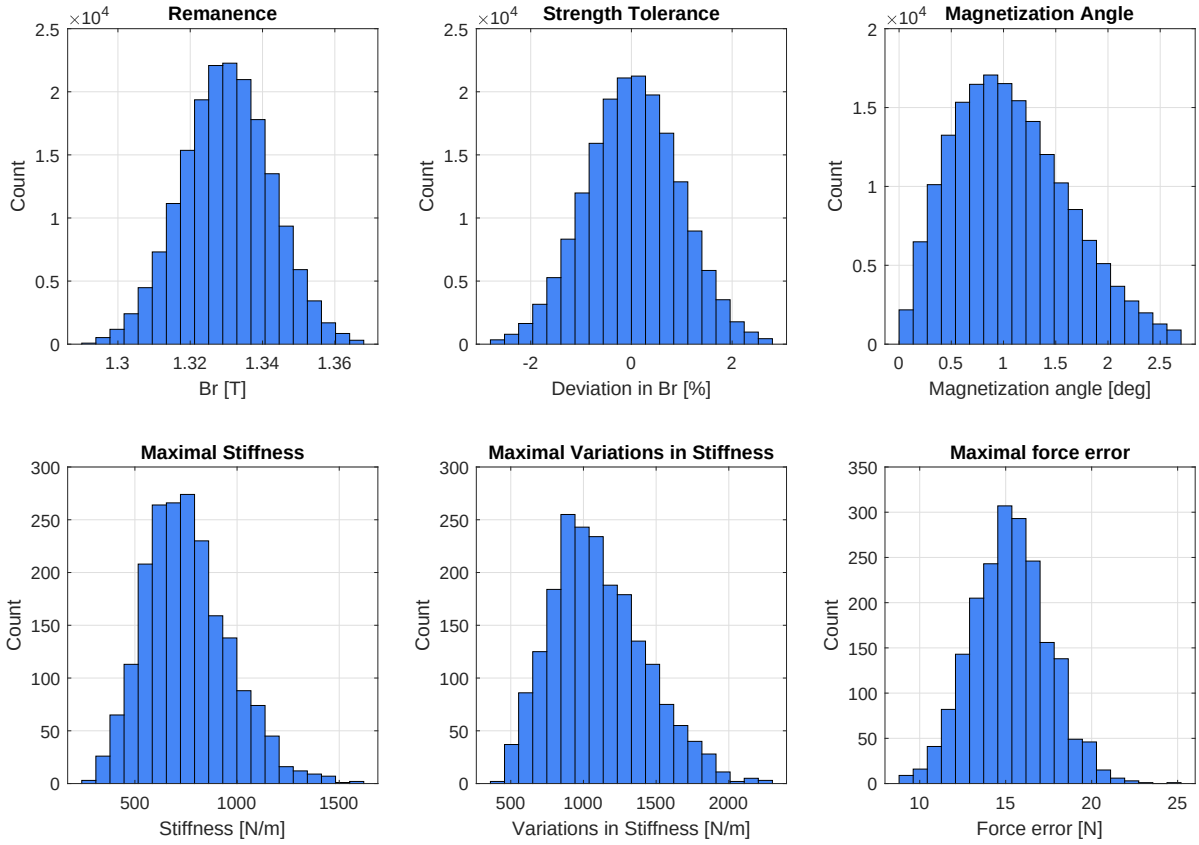

Figure 7.1: Generated magnetic tolerances with standard stock magnets and the resulting performance.

maximum stiffness of the gravity compensation system can still be as high as 1600 $[N/m]$. Therefore, it cannot be guaranteed that the stiffness requirement will be met. Moreover, the peak to peak change of the stiffness requirements is met in 0 % of the cases, as is the force error requirement. This confirms the conclusions drawn on the basis of the measurement data: standard stock magnets are not suitable for a long stroke gravity compensator application.

7.2.2. HIGH GRADE CUSTOM MAGNETS

To estimate the performance using high-grade custom magnets, a specialized supplier has been contacted to obtain values for the magnetic tolerances. These are listed in table 7.1. For the simulation, the specified tolerances of magnet grade A are used, and the dimensions of the magnets are chosen as those of the original design (see table 4.4)

Table 7.1: Commonly used tolerances for magnet grades

	Grade A	**Grade B**	**Grade C**
Max. deviation of magnetic dipole moment	1 %	3 %	5 %
Max. deviation of magnetization angle	1 $[deg]$	3 $[deg]$	5 $[deg]$

With these original magnet dimensions and tighter magnet tolerances, the performance has improved significantly. The obtained mean stiffness, mean peak to peak change of the stiffness, and mean force error have reduced to 150 $[N/m]$, 250 $[N/m]$, and 1 $[N]$ respectively. Also the worst case stiffness possible has reduced to 300 $[N/m]$, meaning that this requirement is satisfied in 100 % of the cases.

Unfortunately, this is not the case for the peak to peak change of the stiffness and the force error. The average peak to peak change of the stiffness obtained is 250 $[N/m]$, meaning that it is expected that only in approximately 30 % of the cases this requirement will be met. In the worst case, the peak to peak change in stiffness can even reach 550 $[N/m]$, which is close to 3 times the desired value.

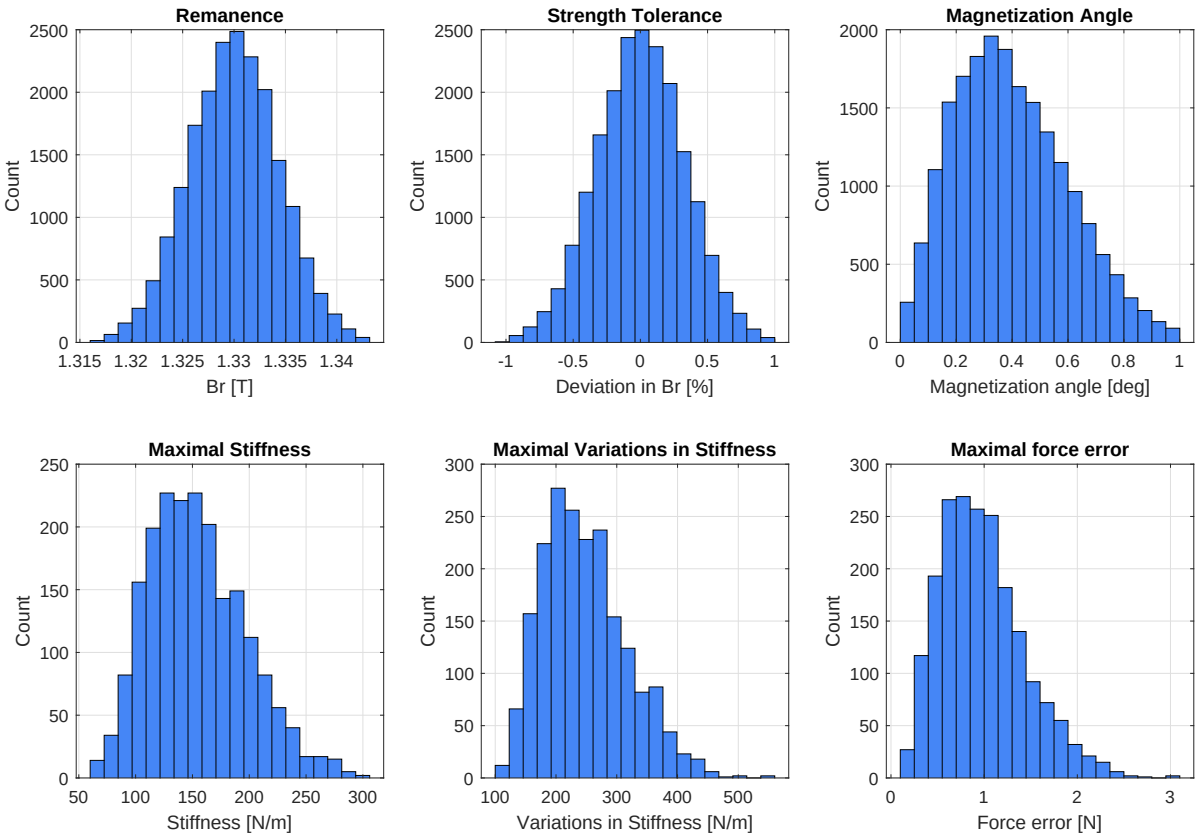

Figure 7.2: Generated magnetic tolerances with Grade A magnets and the resulting performance.

The mean force error obtained is 1 $[N]$, and only in 60% of the cases the required performance will be achieved. The maximum worst-case force error that can be expected is 3 $[N]$, which is 3 times higher than the design specification.

7.3. IDENTIFICATION OF WORST CASE SCENARIOS

From the previous section it is concluded that even with the magnetic tolerances set to maximally 1 % deviation in the dipole moment, and 1 $[deg]$ deviation of the magnetization angle, the required performance will generally not be met. In this section, the worst-case scenarios are investigated to gain an understanding of what magnet tolerances give rise to the worst-case performance situations. This information can subsequently be used, to come up with a strategy for the implementation of a long stroke magnetic gravity compensator in which at least some design requirements will be met. To achieve this, the magnetic tolerances resulting in the worst performance are saved from the Monte Carlo simulations and compared to the results already obtained in section 4.4.

7.3.1. WORST CASE FOR THE PEAK TO PEAK CHANGE OF THE STIFFNESS

From the results of the Monte Carlo simulations, it is concluded that the stiffness requirement is always met. However, the peak to peak change of the stiffness can still reach values up to 550 $[N/m]$, thereby not fulfilling the design specification. In section 4.4 it was concluded that high stiffness are the result of asymmetries in the stator magnets. This is confirmed in the study using the Monte Carlo approach.

For the magnetization strength this situation is created when a magnet on the left side is for example 1% stronger, while the opposing magnet on the right side is 1% weaker. This is visualized in figure 7.3a. The resulting stiffness in this case is 180 $[N/m]$, which on itself is not a problem. However, when the opposite situation also occurs (like in 7.3a), than the local stiffness there will be -180 $[N/m]$, resulting in a peak to peak change of the stiffness of 360 $[N/m]$.

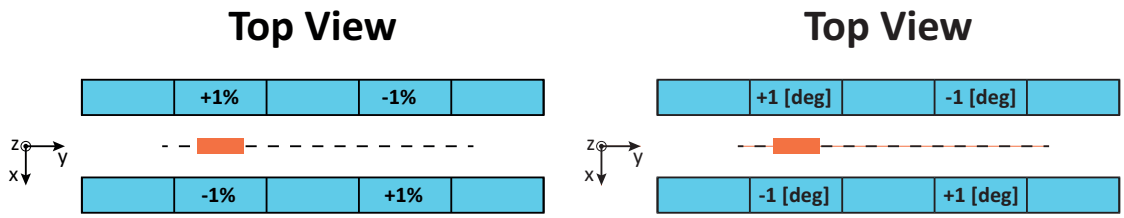

(a) Worst case stiffness due to magnetization strength.

(b) Worst case stiffness due to magnetization angle.

Figure 7.3: Asymmetrical tolerances causing the worst case stiffness and peak-to-peak change of the stiffness (stator indicated in blue, mover indicated in orange).

For the magnetization angle, the same is true, that a positive magnetization angle on the left, combined with a negative magnetization angle on the right results in a high stiffness, which was also observed from the 2D simulations presented in 4.4. In the case of 1 $[deg]$ deviations of the magnetization angle this would result in a stiffness of 240 $[N/m]$. Similarly to the case for the magnetization strength, a high peak to peak change is created when this situation also occurs in the opposite way, as shown in figure 7.3b. The resulting stiffness change in that case is 480 $[N/m]$.

An important additional result is that in both the case of the magnetization strength and the magnetization angle, the resulting force errors remain negligibly low (force error $\lessapprox$ 0.1 $[N]$). This result was also obtained from the 2D investigation from chapter 4.

7.3.2. WORST CASE FOR FORCE ERROR

As seen from the investigation of the effect of magnetization tolerances presented in section 4.4, and from the results from the previous section, it is concluded that the magnetization angle of the stator magnets does not have a large effect on the force error. This is not the case, however, for the magnetization strength. A high force error occurs when two opposing magnets on the left and right side are either both 1% stronger, or are 1% weaker. This situation can be seen in 7.4

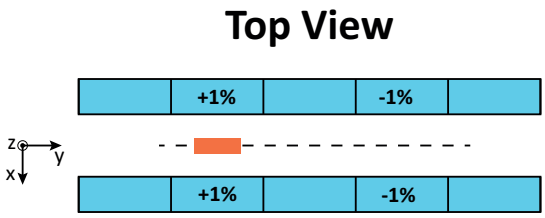

Figure 7.4: Symmetrical tolerances of the magnetization strength causing the worst case force error.

The resulting force error is 3 $[N]$ (or -3 $[N]$). As in this case symmetry is maintained between both stator sides, the resulting stiffness (and thus also its peak to peak change) are very low (change of the stiffness $\lessapprox$ 20 $[N/m]$).

7.3.3. CONCLUSIONS

From this investigation, it can be concluded that high stiffnesses and therefore also high peak to peak change of the stiffness, occur in situations where asymmetry is created between the left and right stator. On the contrary, when the magnetization strength deviations are of the same sign on both sides, high force errors are the result. In other words, the performance in terms of stiffness can only be increased at the expense of the force error, and vice versa.

7.4. RECOMMENDED IMPLEMENTATION

Using the results from the investigation presented in the previous section, various implementation options are proposed. Firstly the possibilities are discussed when grade A magnets are used. Secondly, it is investigated what magnet tolerances are needed to meet all the specified design requirements.

7.4.1. IMPLEMENTATION USING GRADE A MAGNETS

In section 7.3 situations with the worst-case performance are identified. The results showed a contradiction between the worst case for the stiffness and the force error. Therefore, a design compromise is inevitable when using magnets with tolerances specifications of a maximum 1 % deviation of the dipole moment, and a maximum magnetization angle of 1 $[deg]$. Either the peak to peak change of the stiffness, or the force error is prioritized. This can be achieved by smart magnet placement using the measurement data provided by the supplier when ordering this kind of magnets. Note, however, that improving one aspect of the performance, will always be at the cost of another other.

PRIORITIZE FORCE ERROR REQUIREMENT

If the force error is most important, it is recommended to assemble the gravity compensator such that magnets with equal deviations in the magnetization strength on either side, is avoided. This means the force errors are kept to a minimum. However, this will result in a higher change of the stiffness. To solve this issue, it is recommended to implement higher-order fitting methods or a lookup table of the stiffness. In this way, the higher changes in the stiffness can be compensated for.

PRIORITIZE THE PEAK TO PEAK STIFFNESS REQUIREMENT

In the other case, where the stiffness requirements of higher importance. The situations as depicted in figures 7.3a and 7.3b should be avoided. This will result in low stiffnesses (hence also in low peak to peak change of the stiffness), at the expense of the force error. To compensate for this, either the cooling performance of the machine could be improved. Or the possibilities of manual magnetic tuning, using ferromagnetic shims, could be investigated to reduce the force error.

7.4.2. IMPLEMENTATION OF MAGNETS WITH TIGHTER TOLERANCES

The approaches described in the previous section have some serious disadvantages. The most obvious one being, that a trade-off is required between two important design requirements. Also, they involve a labor intensive assembly process, where a puzzle needs to be solved to determine the position of each individual magnet received from the supplier. This can be a cumbersome process, where, especially in the case of prioritizing the stiffness requirements, additional magnets need to be ordered to find a configuration that meets the requirements.

A better alternative could be to order magnets with a higher tolerance specification in consultation with the supplier. Using the Monte Carlo approach it is investigated what the required magnet tolerances are to meet the original performance specifications. The results of this investigation are that the maximal deviation of the magnetization strength and the magnetization angle required to achieve this are 0.5 %, and 0.5 $[deg]$

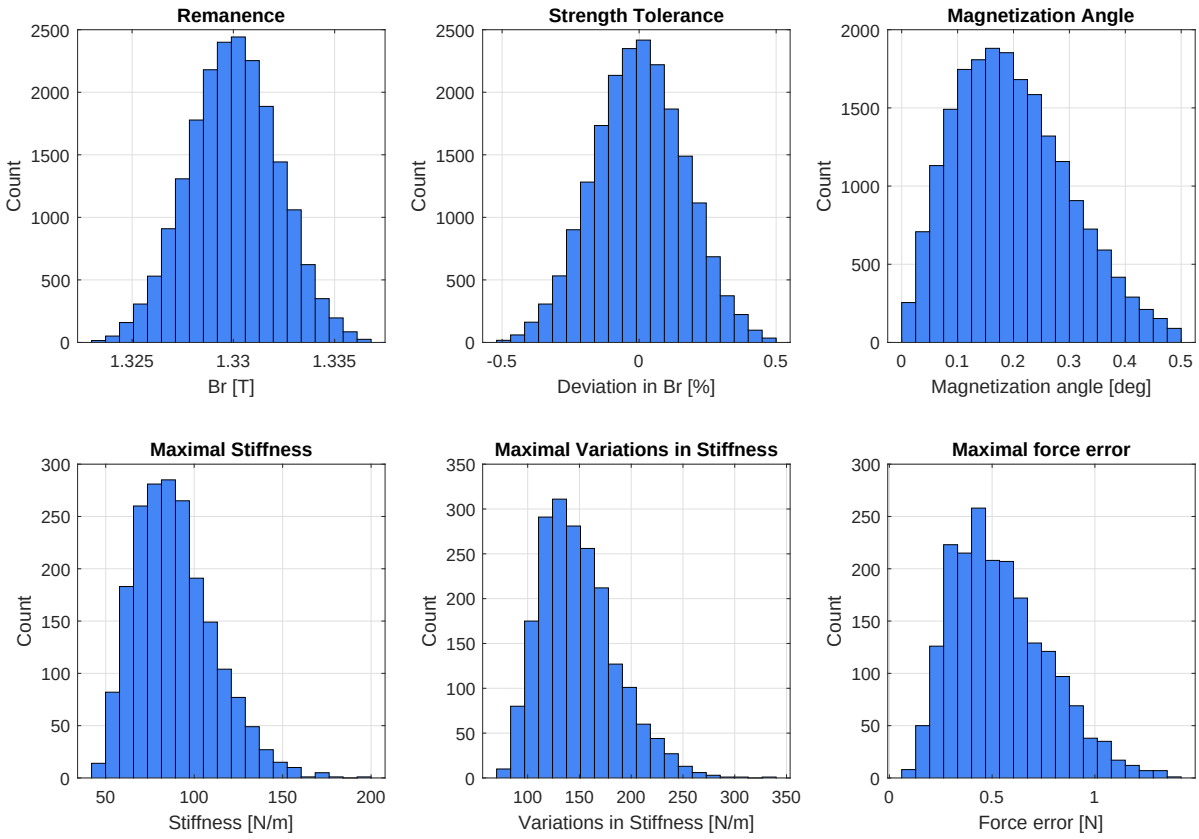

Figure 7.5: Generated magnetic tolerances with highly specified magnets and the resulting performance.

The obtained performance can be seen in figure 7.5. The mean maximum stiffness, maximum peak to peak change of the stiffness, and the force error are 90 $[N/m]$, 150 $[N/m]$, 0.5 respectively. The stiffness requirement is met in 100 % of the cases and the peak to peak change and force error requirement in 90 % and 95 % respectively.

7.5. CONCLUSIONS

The goal of this investigation was to determine the possibilities of implementing a long stroke magnetic gravity compensator system. For this, the effects of the magnetic tolerance specifications on the performance of the gravity compensator needed to be investigated in 3D, using a Monte Carlo simulation. From this investigation the following conclusions were drawn:

1. **Demonstrator performance**: The performance estimated from the measurement data matches the performance estimated using the 3D surface charge model, thereby validating the conclusion that standard stock magnets are not suitable for the intended application.

2. **Required magnetic tolerances to meet original design requirements**: If the original design requirements are to be met, the maximally allowed deviation of the magnetization strength is 0.5 %, and the maximally allowed magnetization angle is 0.5 $[deg]$. The cost of the magnets of the complete long-stroke gravity compensation system will result in approximately € 1000

3. **Performance achievable with grade A magnets:** If grade A magnets are used, it is advised to sacrifice the performance in terms of parasitic stiffness requirements for force error. The increased stiffness level can then be compensated for using simple fitting algorithms. Alternatively, force error requirements can be sacrificed for stiffness, and better cooling of the machine or magnetic tuning options could be considered. In this case, the price of the magnets would amount to approximately € 700.

8

CONCLUSIONS AND RECOMMENDATIONS

The goal of this study was "***To design and experimentally validate a permanent magnet based long-stroke gravity compensator for a nanometer precision positioning machine***". This involved four specific research goals. First of all, a suitable modeling technique was required for calculating the interaction forces between permanent magnets. From these interaction forces, the performance parameters could be obtained thereby making the model a crucial tool for the assessment of the feasibility of the long-stroke magnetic gravity compensator. Secondly, a state of the art study was conducted where four fundamentally different magnetic configurations were found that are suitable for the application in a magnetic gravity compensator. The third objective was to combine the model and the results from the state of the art study to come up with a magnetic design and validate both the design and the model using an experimental setup. Finally, the achievable performance of a long-stroke magnetic gravity compensator was to be determined, in order to study the feasibility of its application in high precision positioning machines. In this chapter, the conclusions regarding all these research objectives are discussed, followed by recommendations for further research.

8.1. CONCLUSIONS

8.1.1. MODELING

Four different modeling techniques were found (section 2.2) for the calculation of interaction forces between permanent magnets. By comparison, it was shown that the dipole model is not a suitable design tool as its application is very limited (section 2.3.1). However, the concept of representing a permanent magnet as a perfect dipole is crucial in the process of designing and manufacturing a magnetic gravity compensator. This is due to the fact that it is used in the measurement of physical magnets, where it serves as the bridge between a physical magnet, and the needed parameters for its modeling. Also, it can be concluded that a 2D modeling technique which is a hybrid between FEM and the coil model is a very strong and capable design tool. This method provides a lot of valuable understanding into the working principles of the design which allows for a quick design process. This can be achieved by analyzing the magnetic field created by the stator magnets, and using it to hone the dimensions and gap sizes until the desired requirements are met. However, from the comparison presented in section 2.3.2 it must be concluded that 2D modeling also has its limitations, as the inherent three-dimensional effects are neglected. Therefore, it is advised to always check the results obtained from a 2D analysis with a 3D modeling technique.

8.1.2. LITERATURE STUDY INTO THE STATE OF THE ART

From the example of two repelling magnets, it can be concluded that two equally sized repelling magnets are not suitable for a gravity compensation application. This is due to the exponential force increase with the inverse of the center-to-center distance between them. This leads to the conclusion that more sophisticated magnetic designs are needed to meet the design requirements. From the literature study, four fundamental configurations were found (see figure 3.1) that provide the unique combination of a high load capacity with a low local stiffness. This property is illustrated in figure 3.2 where the force-displacement curves for all configurations show a region where the stiffness is zero. By refining the magnet dimensions and the gap sizes, the obtained stiffness can be tuned, however, due to time limitations in this study, it has been decided

to choose the two most suitable configurations for further investigation. The trade-off was done mainly using the available information from literature (see section 3.2). Configuration 1 was found to be unsuitable due to the occurring demagnetization which is a consequence of the small airgap required to achieve a stiffness below 1000 $[N/m]$. Configuration 3 and 4 were selected as the most suitable for the application into a long-stroke gravity compensator mainly due to their higher force density.

8.1.3. MAGNETIC DESIGN AND EXPERIMENTAL VALIDATION

Using a 2D modeling approach the two most potent configurations were dimensioned using ideal magnets, resulting in 3 different design variations. Also, it has led to the conclusion that three separate gravity compensators are necessary to meet the specified requirements for the load capacity while not exceeding the maximum cross-sectional dimensions. Under this simplification of ideal magnets the obtainable stiffnesses proved to be very low with values observed as low as 24 $\left[\frac{N}{m}\right]$.

Multiple magnets are needed in the long stroke direction due to the manufacturing limitation regarding the maximum dimensions of permanent magnets. Therefore, a comparison was made between the three designs with the purpose to determine the sensitivity of the stiffness to the present manufacturing tolerances of permanent magnets. The included tolerances are variations in magnet dimensions, magnetization strength, and magnetization angle. In all designs, the stiffness showed a strong sensitivity to these variations, as a maximum stiffness of 1677 $\left[\frac{N}{m}\right]$ was observed (an increase with a factor 20 w.r.t. the ideal case), leading to the conclusion that manufacturing tolerances of permanent magnets cannot be neglected in the design of long-stroke magnetic gravity compensators. The design using magnetic configuration 4 (see figure 3.1d) proved to be the least sensitive to these tolerances and was therefore chosen for the application in the long-stroke gravity compensator.

For the practical validation of the long-stroke concept, an experimental setup was designed and built. The chosen approach for this validation was by measurement of the magnetic field produced by the stator of the gravity compensator. With this experimental setup firstly the working principle of the magnetic design was validated. This was done by measuring the linearity of the magnetic field (section 6.2) thereby confirming the magnetic design. Secondly, it was observed from the measurement data that no performance-limiting spikes or discontinuities are measured in the magnetic field at a transition between two magnets in the long-stroke direction. This leads to the conclusion that no practical issues are foreseen that could potentially limit the performance of a long-stroke magnetic gravity compensator. Thirdly, measurements over the entire long-stroke direction were used for the validation of the model. A maximum deviation of approximately 9.8 $[mT]$ was measured, which is within the expected 3σ uncertainty margin, therefore validating the model. Finally, from the measurement data, it was concluded that it is not possible to meet the design specifications with standard stock magnets. Even though an estimated maximum stiffness of only 720 $\left[\frac{N}{m}\right]$ was obtained, the estimations for the peak to peak change of the stiffness and maximum force error are 1320 $\left[\frac{N}{m}\right]$, and 19 $[N]$ respectively, therefore not meeting the required design specifications of 200 $\left[\frac{N}{m}\right]$, and 1 $[N]$.

8.1.4. ACHIEVABLE PERFORMANCE

The achievable performance of a long-stroke magnetic gravity compensator made of custom magnets was investigated using a Monte Carlo simulation. In this approach, the validated model was used to 2000 gravity compensator systems were simulated with randomly generated magnetic tolerance values. For each case, the performance parameters were saved and analyzed.

When grade A magnets are used (maximum strength deviation of 1 % and magnetization angle of 1 $[deg]$) the performance increases significantly. The mean maximum stiffness of approximately 150 $\left[\frac{N}{m}\right]$, with a worst case stiffness of approximately only 300 $\left[\frac{N}{m}\right]$. Therefore showing that the stiffness requirement will always be met. The mean peak to peak change of the stiffness obtained in the simulation is $\approx$ 250 $\left[\frac{N}{m}\right]$, but in the worst case scenario this could increase to approximately 550 $\left[\frac{N}{m}\right]$. Finally a mean force error and the worst case force error resulting from the simulation are 1 $[N]$ and 3 $[N]$ respectively.

Even though the changes of the stiffness exceeds the design specification of 200 $[N/m]$, the design can still successfully be implemented. From section 7.3 it was concluded that the cases in which the maximum change of the stiffness and the maximum force error are obtained, are conflicting. Therefore, a design choice has to be made when using Grade A magnets. In the case that the force error is prioritized, higher-order fitting methods or a lookup table in the control algorithms can be applied in the eventual machine. In this way, the changes

in the stiffness can be compensated for, which allows subsequently for the placement of the magnets such that the force error requirements are met. Alternatively, if the maximum peak-to-peak change of the stiffness is prioritized, asymmetries in the stator magnets should be avoided leading to low stiffnesses. This goes at the expense of the force error which can be solved by improving the cooling of the machine, or if desired, manual magnetic tuning of the gravity compensator can be investigated by using ferromagnetic shims.

Finally, if neither of these design compromises is desired, the tolerances on the magnets can be increased to a maximum deviation of the strength of 0.5 % and a maximum deviation of the magnetization angle of 0.5 $[deg]$ leading to the performance values seen in table 8.1. In this case, all performance values will be met, at the expense of the system costs.

Table 8.1: Overview of obtained performance with different magnet classes.

Design Requirements	**Values**	**Experimental setup**	**Grade A magnets**	**Highly specified magnets**
Strokes: x, y, z	$1,200,1\,[mm]$	$1,200,1\,[mm]$	$1,200,1\,[mm]$	$1,200,1\,[mm]$
Nominal load Capacity:	$196.2\,[N]$	$197.9\,[N]$	$196.0\,[kg]$	$196.0\,[kg]$
Parasitic Stiffness:	$\leq 1000\,[\frac{N}{m}]$	$720\,[\frac{N}{m}]$	$150\,[\frac{N}{m}]$	$90\,[\frac{N}{m}]$
Change of Stiffness:	$\leq 200\,[\frac{N}{m}]$	$1320\,[\frac{N}{m}]$	$250\,[\frac{N}{m}]$	$150\,[\frac{N}{m}]$
Force Error:	$\leq 1\,[N]$	$12\,[N]$	$1\ [N]$	$0.5\ [N]$
Magnet costs:		$\approx$ € 500	$\approx$ € 800	$\approx$ € 1000

8.1.5. MAIN CONCLUSIONS

Looking back at the research goals of this study the following conclusions can be made: Firstly a suitable design method has been found making use of a combination of finite element method and a coil model for determining the load capacity and stiffness of magnetic designs. Secondly, the proposed design and the model have both been validated using an experimental setup. Finally, it was shown that it is possible to manufacture a long-stroke gravity compensator that can be implemented such that the design requirements can be met. Therefore, it can be concluded from this study that a long stroke magnetic gravity compensator is a suitable concept to be applied in nanometer positioning machines thereby allowing for the innovation towards more cost-effective high precision positioning equipment.

8.2. RECOMMENDATIONS

Before the long-stroke magnetic gravity compensator is applied to the design of an actual high precision positioning setup, it is recommended to investigate the damping in more detail, as in this study only a crude approximation was obtained. It is advised to do this by means of a more detailed modeling approach, and experimental validation through an actively controlled experimental setup. Not only would this provide the experimental validation for the estimations of the damping, but it would also provide a possibility to experiment with different fitting algorithms or strategies to compensate for the changes in the stiffness.

Alternatively, if better performance is required, for example, a reduction in the changes of the stiffness without increasing the costs of the gravity compensation system, this could be achieved by improving the proposed magnet configuration. A suitable approach would be to use computer-aided optimization of the magnet dimensions and gap sizes. Furthermore, the effect of more exotic magnet shapes could be investigated. As this was the first study into this subject, it was chosen to only investigate cuboidal magnets, to limit the design space. However, in practice, the magnets are not restricted to a rectangular shape, and using different shapes could yield better performance.

A

Datasheet of Hirst GM07

GM07 & GM08 Gaussmeter

- Menu driven
- Graphical LCD display
- DC, AC, PEAK, MAX, HOLD and STORE functions
- Operating function and units displayed
- USB & RS232 (GM08)
- Battery operated
- External power supply connection (GM08 only)
- Multi lingual
- Thin semi-flexible probe
- Visible measurement point
- Probe polarity indicator

Hirst Magnetic Instruments' GM07 and GM08 microprocessor controlled gaussmeters complement the range of Hirsts compact desktop instruments. Designed for factory floor, on site and laboratory use the instrument offers a simple menu driven front end.

Hirst Magnetic Instruments' GM07 and GM08 microprocessor controlled Gaussmeters offer sophisticated measuring functions in a simple to use, menu driven, hand-held package.

Designed for factory floor, on site and laboratory measurement of magnetic flux Density and Magnetic Field Strength in SI or CGS, these instruments give excellent value for money

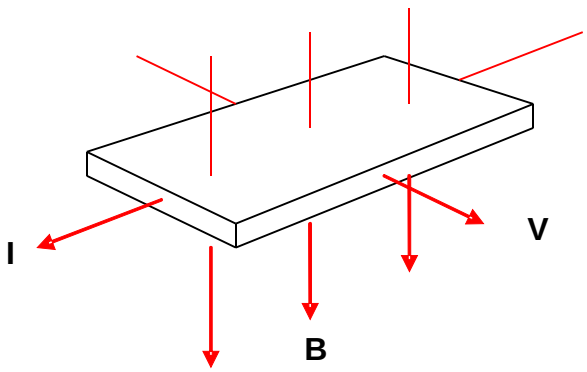

Hirst Magnetic Instruments Ltd
Tesla House, Tregoniggie, Falmouth,
Cornwall, TR11 4SN, United Kingdom

Tel: +44 (0) 1326 372734
Fax: +44 (0) 1326 378069
E: enquiries@hirst-magnetics.com

Website www.hirst-magnetics.com
VAT Reg. No. GB730 0277 74
Registered in England No 1564814

Introduction

The GM07 and GM08 Gaussmeters have been designed and manufactured by Hirst Magnetic Instruments Ltd, a company with more than 40 years experience in Magnetic Measurement. This experience and our extensive knowledge of the magnetics market has enabled us to design an instrument incorporating all of the measurement functions a user is likely to need. The GM07/08 is controlled via a simple menu and is supplied with a thin semi-flexible Transverse Hall Probe suitable for all but the very smallest of applications.

The GM07/08 incorporates an analogue peak detector for the DC and AC peak functions. This, coupled with the microprocessor operation means fast response is possible with digital stability (fast pulses / no droop in readings).

Measurement functions

The GM07/08 can measure :-

DC DC magnetic field measurement.

DC PEAK Maximum positive peak reading of the DC field.

AC RMS True RMS (Root mean Square) of input signal.

AC RMS MAX Maximum true RMS.

AC PEAK Maximum positive peak value.

Utilities

The GM07/08 has a number of UTILITIES options allowing the operator to disable or select various times for the automatic POWER DOWN. Also nulling routines can be selected.

The GM07/08 also has the facility to operate its menu structure in English, French German, Italian, Spanish and Portuguese.

Calibration

The GM07/08 is calibrated to standards traceable to the National Physical Laboratories.

During manufacture, the accuracy of nuclear magnetic resonance (NMR) is used to determine the irregularities and none- conformities of the GM07/08 and its Hall Probe. This is stored and used mathematically to automatically correct readings taken by the GM07/08.

Measurement units

The GM07/08 can measure magnetic flux density or magnetic field strength. The menu system enables the operator to easily choose between Tesla, Amps/m (SI Units), Gauss or Oersted (cgs units).

Data capture

The GM07/08 can HOLD measured values by pressing the Hall Probe button. Pressing the button again releases HOLD (when enabled).

The GM07/08 can also STORE measured values. These values can later be RECALLED, either on the meter or via RS232/USB with the GM08.

Applications

The GM07 is ideal for inspection and measurement of magnetic flux density of magnets and magnetic assemblies in both goods inward and Quality Assurance environments.

Where individual measurements need to be recorded the GM08 will store and upload not only the measured values, polarity, measurement units and measurement function, but also the time at which the measurement was taken.

Applications include: Computer Disk Drive Actuators, Loudspeaker Air Gaps, Electric Motor air gaps(including pancake and Permanent Magnets), Transformer Stray Field measurements, Magnetiser and Demagnetiser Field measurements, Bending Magnets, Non-Destructive Testing (Magnetic), Goods inward and Quality Assurance Inspection, automated magnet calibration, etc.

GM08 Communications

The GM08 features all of the functions of the GM07 plus:

An interface to provide RS232 and USB communication for uploading measurement data to a host computer. The GM08 can also be remotely controllable via this link.

A full driver suit is available as an optional extra. This includes sample programs with full source code (Microsoft Visual C++ .NET) for the 2000 operating system, XP and later. A Labview [1] VI is included. Linux is also supported.

The GM08 also incorporates a non volatile memory to enable the retention of stored values even when switched off.

The GM08 also includes a time keeping device to record the time data is stored and an external DC power supply socket for bench top applications.

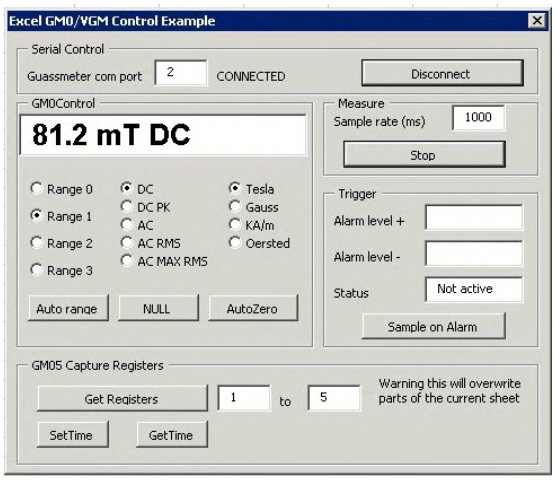

Screen shot from within Microsoft Excel

GM07 & GM08 Hall probes

Both the GM07 and the Gm08 are supplied with a transverse Hall probe as standard (Tp002).

The design of the Hall probe is critical to the satisfactory operation of any gaussmeter. For the GM06 and GM07 we have used our experience to produce a transverse Hall probe which is semi-flexible and only 1 mm thick by 4 mm wide. This enables operators to take measurements in tight spaces and narrow air gaps. In addition the sensitive Hall element is clearly visible so the user knows exactly where the measurement is being made..

The probe is fitted with a push button enabling the operator to HOLD and STORE measurments and orientate the probe for polarity readings.

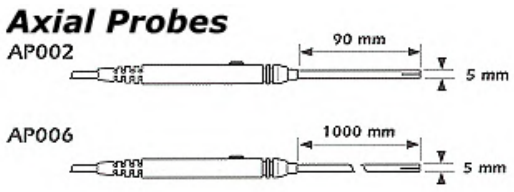

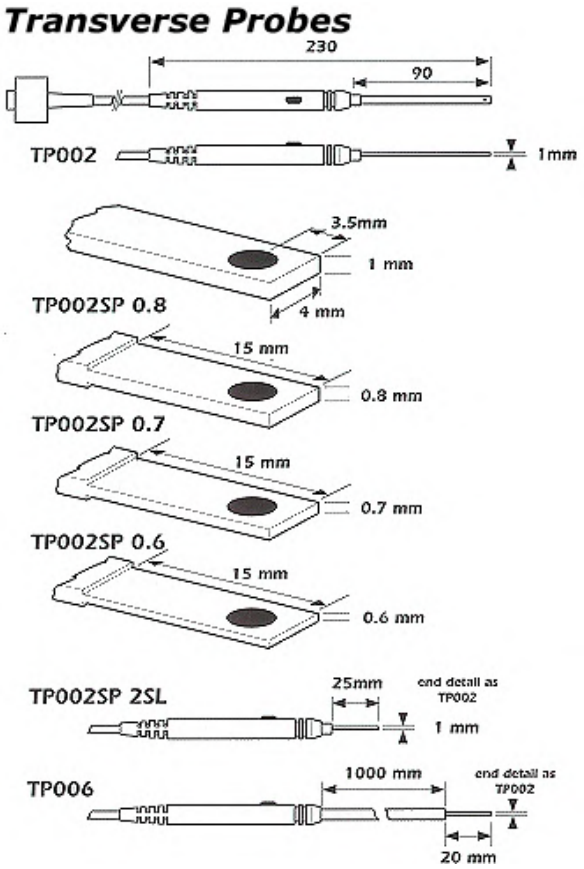

All transverse and axial probes are fully interchangeable with Hirst Magnetic Instruments Ltd's GM04, Gm05, VGM01, BGM01, GM07 and GM08 gaussmeters

Axial and transverse probes are also available with longer cable lengths. If you require a long cable or a custom probe please contact the sales office for more information

Hall Effect Theory

In an ideal world, a Hall Element consists of a small slab of semi-conductor material. Current passes from one end of the slab to the other and the voltage on each edge of the slab is the same when no magnetic field is present. If a magnetic field is now applied through the top to bottom surfaces of the slab, a voltage appears across the sides of the slab which is directly proportional to the Magnetic Flux Density or Magnetic Field Strength. In reality, all practical Hall Probe elements are only linear within certain limits, normally 1%-2%. The more accurate and thinner the probes, the greater the expense. Most Gaussmeter manufacturers approach this problem by selecting current and Hall Probe load resistance to minimise these non-linearity errors.

The Hall Probes are connected to Gaussmeters, the Gaussmeters are designed to be linear to make the best use of the non-linear Hall Probes.

The philosophy behind the design of the GM04 is that both the Probe and the Gaussmeter will contain non-linearities and errors. The difference between a theoretical, perfect Hall Probe and that of an individual Hall Probe is measured and the difference recorded in an E2prom located in the Hall probe socket (this memory device also contains other information such as serial number and calibration date).

The perfect Hall Probe is in fact a calibration process using a technique known as Nuclear Magnetic Resonance (NMR) which gives very high accuracy.

The errors between the GM07/08 and an ideal electronic circuit are measured and recorded in it's internal E2prom.

When a measurement is taken the voltage generated by the Hall Probe element is amplified by the GM07/08 electronic circuit and digitised in an Analogue to Digital converter.

The software of the GM07/08 then automatically corrects this data mathematically, firstly with the Hall Probe calibration information and then with the GM07/08 calibration information.

This technique gives superb results and enables calibration of the Gaussmeter to be carried out in software rather than "select on test" resistor values. The GM07/08 includes other innovative techniques which further improve and give additional long term stability.

The GM07/08 also includes a linear analogue circuit for peak detection. This dedicated circuit enables the accurate capture of transient events without the inherent delays of Analogue to Digital Converter sampling times.

Although this captured voltage level will decay, In the analogue circuit, it is converted and displayed from a digital storage giving zero droop digital storage.

GM07/08 SPECIFICATION

AUTO RANGING AND MANUAL RANGING

Range 1
0 to more than 3 Tesla
resolution 1 milliTesla

Range 2
0 - 299.9 milliTesla
resolution 100 microTelsa

Range 3
0 - 29.99 milliTelsa
resolution of 10 microTesla

Range 4
0 - 2.999 milliTesla
resolution of 2 microTesla

Measurements can be made in Tesla, Gauss, Amps/m or Oersted.

(1 mT = 10 Gauss = 0.796 kA/m)

Accuracy (at 20 degC +/- 1%

(DC) Traceable NPL

Reproducibility +/- 0.5%

Temperature Coefficient
Better than +/- 0.1 % of reading / degC including probe.

Frequency Range
DC and 15Hz to 10kHz

Averaging Time Constant
100 milliseconds

Functions
DC, DC Peak, AC RMS, AC RMS MAX, AC PEAK

Display
LCD graphics display monochrome.

Display Sampling rate
3 / second (approx)

Facilities
Store and Recall on 0 99 samples. Hold facility. Analogue peak with digital storage. Auto and manual ranges. Automatic reading conversion between different units. Operating setup at time of power down is stored and recalled automatically at power-on. Functions are selected with an easy to use menu.

Operating Temperature Range
0 degC to +50 degC

Storage Temperature Range
-20 degC to +70 degC

Battery Type
4 of Longlife1.5V Alkaline AA cells.

Battery Life
Battery Life of 15 hours continuous operation. Auto power down after 1, 4 or 10 minutes or can be disabled, all under menu control.

Dimensions

Length	175mm
Width	89mm
Height	40mm

Weight
430 g (not including probe)

Standard Accessories
Transverse Hall Probe, Zero Flux Chamber and Carry Case.

Optional Accessories
Axial Probe Ref AP002.
Replacement Transverse Probe Ref TP002.
Reference Magnets Axial and Transverse contact factory for details.

GM08 ADDITIONAL FEATURES

RS232 and USB
Used for data transfer and remote control. Software handshaking. USB 1.1 Compliant.

Analogue Output
+/- 3 Volts full scale.

Non volatile memory
The GM07 and GM08 will retain stored measurements when the instrument is switched off.

Time Keeping
The GM08 has a time keeping device so that the time that measurements were taken can also be recorded.

External PSU Socket
An external PSU (not supplied) may be used to power the GM08 when used in bench top applications.

ADDITIONAL STANDARD ACCESSORIES

Software
Windows communication software is supplied with the GM08. This allows the user to download readings, stored data and control the instrument remotely.

The Hall Probe
Both the GM07 and GM08 are supplied with a transverse Hall probe as standard.

The design of the hall probe is critical to the satisfactory operation of any gaussmeter. For the GM07 and GM08 we have used our extensive industrial experience to produce a transverse Hall probe which is semi-flexible and only 1mm thick by 4mm wide. This enables operators to take measurements in tight spaces and narrow air gaps. In addition the sensitive Hall element is clearly visible so that the user knows exactly where the measurement is being made.

The probe is fitted with a push button enabling the operator to HOLD and STORE measurements and orientate the probe for polarity readings.

An axial probe is also available as an optional extra. This is only 5mm in diameter and also incorporates a push button for HOLD and STORE functions.

All transverse and axial probes are fully interchangeable on both the GM07 and GM08 without the need for re-calibration.

Compatibility
The probes of GM04 and GM05 meters are directly compatible with the GM07 and GM08 and fully interchangeable.

The software interface (RS232) is also compatible. A GM08 can directly replace a GM05 in service.

RoHS Compliance
Both the GM07 ,GM08 meters, probes and accessories are RoHS compliant.

Hirst Magnetic Instruments Ltd. also manufactures wide ranges of magnetic instruments, magnetisers, demagnetisers, precision demagnetisers and special magnetic systems.

Due to a process of continual improvement, Hirst Magnetic Instruments Ltd. reserve the right to change any specifications without notice.

Document:

Hirst Magnetic Instruments Ltd
Tesla House, Tregoniggie, Falmouth,
Cornwall, TR11 4SN, United Kingdom

Tel: +44 (0) 1326 372734
Fax: +44 (0) 1326 378069
E: enquiries@hirst-magnetics.com

Website www.hirst-magnetics.com
VAT Reg. No. GB730 0277 74
Registered in England No 1564814

B

Data-sheet Magnets Used in Experimental Setup

magnet-shop.net
Vertrauen Sie unserer Kraft!

Quadermagnet 40,0 x 10,0 x 5,0 mm N42 Nickel - hält 8 kg

Artikel-Nummer: QM-40x10x05-N

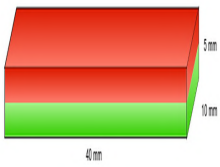

Produkteigenschaften und technische Daten

Haftkraft	8,00 kg / 78.44 N
Volumen	2000,00 m³
Gesamtbreite	10,00 mm
Gesamthöhe	5,00 mm
Gesamtlänge	40,00 mm
Magnetisierungsrichtung	axial
Beschichtung	Nickel (Ni-Cu-Ni)
Maximaltemperatur	80 ° C
Magnetisierungsgüte	N42
Toleranz	± 0,10 mm
Magnet-Material	Neodym
Remanenz Br	12,9 - 13,2 kG
	1,29 - 1,32 T
Koerzitivfeldstärke bHc	10,8 - 12,0 kOe
	860 - 955 kA/m
Koerzitivfeldstärke iHc	min. 12 kOe
	min. 955 kA/m
Energieprodukt (BxH) max	40 - 42 MGOe
	318 - 334 kJ/m³

Produktbeschreibung

ROHS-Richtlinie

Dieser Artikel entspricht der europäischen RoHS-Richtlinie (2002/95/EG - RoHS - Restriction of Hazardous Substances) zur Beschränkung der Verwendung bestimmter gefährlicher Stoffe in Elektround Elektronikgeräten. Nicht registrierungspflichtig gemäß REACH.

Warnung

NdFeB-Magnete sind kein Kinderspielzeug - besonders bei dünneren Abmessungen können diese leicht zerbrechen oder splittern! Ein unkontrollierter Aufprall von zwei Magneten sowie eine äußere, mechanische Schlag- oder Druckbelastung sollte deswegen vermieden werden!

Hinweis zur Bestimmung der Haftkraft

Die von uns ermittelten Haftkräfte sind bei Raumtemperatur an einer polierten Platte aus Stahl S235JR (ST37) mit einer Stärke von 10 mm bei senkrechtem Abzug des Magneten bestimmt worden (1kg~10N). Eine Abweichung von bis zu -10% gegenüber dem angegebenen Wert ist in Ausnahmefällen möglich. Im Allgemeinen wird der Wert überschritten. Beachten Sie bitte, dass bei dünneren, lackierten und nicht absolut planen Untergründen die Haftkraft nur einen Bruchteil der in der Prüfung bestimmten Werte beträgt!

Produktbilder

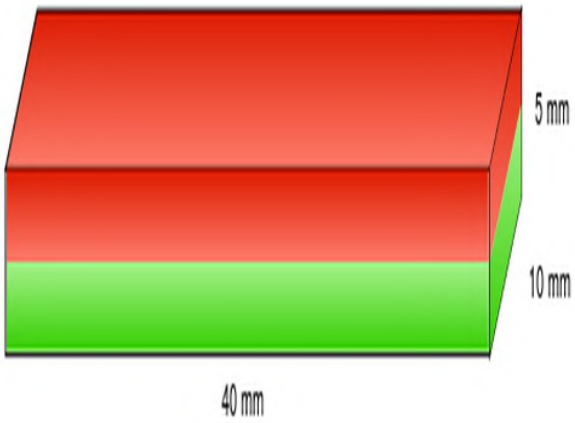
5 mm
10 mm
40 mm

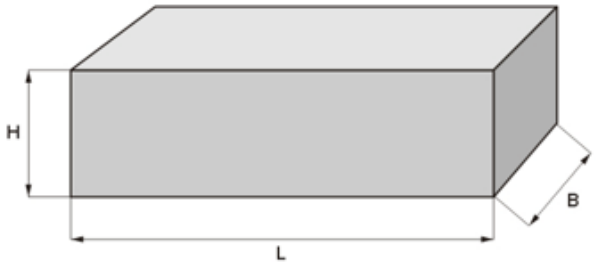
H
B
L

BIBLIOGRAPHY

[1] E. P. Furlani, *Permanent Magnet and Electromechanical Devices* (2001) p. 537.

[2] N. Ida, *Engineering Electromagnetics* (2015).

[3] D. J. Griffiths, *Introduction to Electrodynamics* (2013) p. 623.

[4] K. W. Yung, P. B. Landecker, and D. D. Villani, *An Analytic Solution for the Force Between Two Magnetic Dipoles,* Magnetic and Electrical Separation **9**, 39 (1998).

[5] J. L. Janssen, *Extended Analytical Charge Modeling for Permanent-Magnet Based Devices Practical Application to the Interactions in a Vibration Isolation System*, december (2011) p. 268.

[6] R. Deng, J. W. Spronck, A. Tejada, and R. H. Munnig Schmidt, *2-DoF magnetic actuator for a 6-DoF stage with long-stroke gravity compensation,* in *Proceedings of the 13th euspen International Conference*, May (2013) pp. 6–9.

[7] J. L. Janssen, J. J. Paulides, and E. A. Lomonova, *Study of magnetic gravity compensator topologies using an abstraction in the analytical interaction equations,* Progress in Electromagnetics Research **128**, 75 (2012).

[8] J. L. Janssen, J. J. Paulides, E. A. Lomonova, and B. Delinchant, *Design study on magnetic springs with low resonance frequency,* in *8th International Conference on Linear Drives for Industry Applications* (2011).

[9] J. L. Janssen, J. J. Paulides, E. A. Lomonova, B. Delinchant, and J. P. Yonnet, *Design study on a magnetic gravity compensator with unequal magnet arrays,* Mechatronics **23**, 197 (2013).

[10] J. L. Janssen, J. J. Paulides, and E. A. Lomonova, *Passive Limitations for a Magnetic Gravity Compensator,* Journal of System Design and Dynamics **3**, 671 (2009).

[11] W. S. Robertson, M. R. Kidner, B. S. Cazzolato, and A. C. Zander, *Theoretical design parameters for a quasi-zero stiffness magnetic spring for vibration isolation,* Journal of Sound and Vibration **326**, 88 (2009).

[12] J. W. Spronck, P. Examiner, R. O. Ramirez, F. Application, and P. Data, *(12) United States Patent,* **1** (2002).

[13] Y. Zhou, B. Kou, P. Liu, H. Zhang, F. Xing, X. Yang, Y. Zhou, B. Kou, P. Liu, H. Zhang, and F. Xing, *Force characteristic analysis of a magnetic gravity compensator with annular magnet array for magnetic levitation positioning system,* AP Advances **8** (2018), 10.1063/1.5005964.

[14] C. Ding, J. L. Janssen, A. A. Damen, P. P. Van Den Bosch, J. J. Paulides, and E. A. Lomonova, *Modeling and realization of a 6-DoF contactless electromagnetic anti-vibration system and verification of its static behavior,* IEEE/ASME International Conference on Advanced Intelligent Mechatronics, AIM , 149 (2012).

[15] Y. Zhou, B. Kou, L. Wang, and F. Xing, *Modeling and Analysis of a Maglev Vibration Isolation Unit Using Rectangle Halbach Permanent Magnet Array,* in *17th International Conference on Electrical Machines and Systems (ICEMS)* (2014) pp. 22–25.

[16] J. Li, S. Wang, and L. Wang, *Low stiffness magnetic vibration isolator based on Halbach permanent magnet array,* in *2019 22nd International Conference on Electrical Machines and Systems (ICEMS)* (IEEE, 2019).

[17] Y. Zheng, Q. Li, B. Yan, Y. Luo, and X. Zhang, *A Stewart isolator with high-static-low-dynamic stiffness struts based on negative stiffness magnetic springs,* Journal of Sound and Vibration **422**, 390 (2018).

[18] W. S. Robertson, B. S. Cazzolato, and A. Zander, *A Multipole Array Magnetic Spring,* IEEE transactions on magnetics **41**, 3826 (2005).

[19] Y. Zhu, Q. Li, D. Xu, and M. Zhang, *Modeling of Axial Magnetic Force and Stiffness of Ring-Shaped Permanent-Magnet Passive Vibration Isolator and Its Vibration Isolating Experiment,* IEEE TRANSACTIONS ON MAGNETICS **48**, 2228 (2012).

[20] S. A. Hol, J. C. Compter, A. J. Vandenput, and R. H. Munnig Schmidt, *Design of a Magnetic Bearing,* in *Proceedings 3rd International Conference of the European Society for Precision Engineering and Nanotechnology (Euspen)* (2002) pp. 151–154.

[21] S. A. Hol, E. A. Lomonova, and A. J. Vandenput, *Design of a magnetic gravity compensation system,* Precision Engineering **30**, 265 (2006).

[22] S. A. Hol, *Design and optimization of a magnetic gravity compensator*, 2004 (2004) p. 199.

[23] Y.-m. Choi, M. G. Lee, D.-g. Gweon, J. Jeong, Y.-m. Choi, G. Lee, and D.-g. Gweon, *A new magnetic bearing using Halbach magnet arrays for a magnetic levitation stage,* Review of Scientific Instruments (2012), 10.1063/1.3116482.

[24] R. Deng, *Integrated 6-DoF Lorentz Actuator with Gravity Compensation for Vibration Isolation in In- Line Surface Metrology* (2017) p. 142.

[25] M. Thier, R. Saathof, A. Sinn, R. Hainisch, and G. Schitter, *Six Degree of Freedom Vibration Isolation Platform for In-Line Nano-Metrology,* IFAC-PapersOnLine **49**, 149 (2016).

[26] Bakker Magnetics, *Neodymium Sintered Standard Grades,* (2015).

[27] R. Berkhof, *Vertical vibration isolation using permanent magnets*, master thesis, Delft University of Technology (2015).

[28] Vacuumschmelze, *Rare Earth Permanent Magnets: VACOdym and VACOmax,* (2015).

[29] Goudsmit Magnetic Supplies B.V., *Permanent Magnets Brochure,* (1959).

[30] D. T. van Casteren, K. J. Pluk, J. J. Paulides, and E. A. Lomonova, *Modeling the effects of magnetization variations on a permanent magnet based levitation or vibration isolation system,* Applied Mechanics and Materials **416-417**, 366 (2013).

[31] J. C. Compter, *The Design and Application of Industrial Linear Motors* (2011) pp. 1–155.

[32] N. Derby and S. Olbert, *Cylindrical Magnets and Ideal Solenoids,* American Journal of Physics **78** (2009), 10.1119/1.3256157, arXiv:arXiv:0909.3880v1 .

[33] M. Hall, J. Bartholomew, and L. Henderson, *Measurement of the magnetic dipole moment of ferromagnetic material specimens,* (2001).

[34] S. Möwius, N. Kropff, and M. Velicescu, *Measurement technologies for permanent magnets,* **7**, 15 (2018).

[35] J. C. Compter and J. L. van der Veen, *Magnet analysis with a Helmholz coil set,* IEE Proceedings - Science Measurement and Technology **150**, 177 (2003).

[36] D.-x. Chen, E. Pardo, and A. Sanchez, *Demagnetizing Factors of Rectangular Prisms and Ellipsoids,* **38**, 1742 (2002).

[37] D. Chen, E. Pardo, and A. Sanchez, *Fluxmetric and magnetometric demagnetizing factors for cylinders,* **306**, 135 (2006).